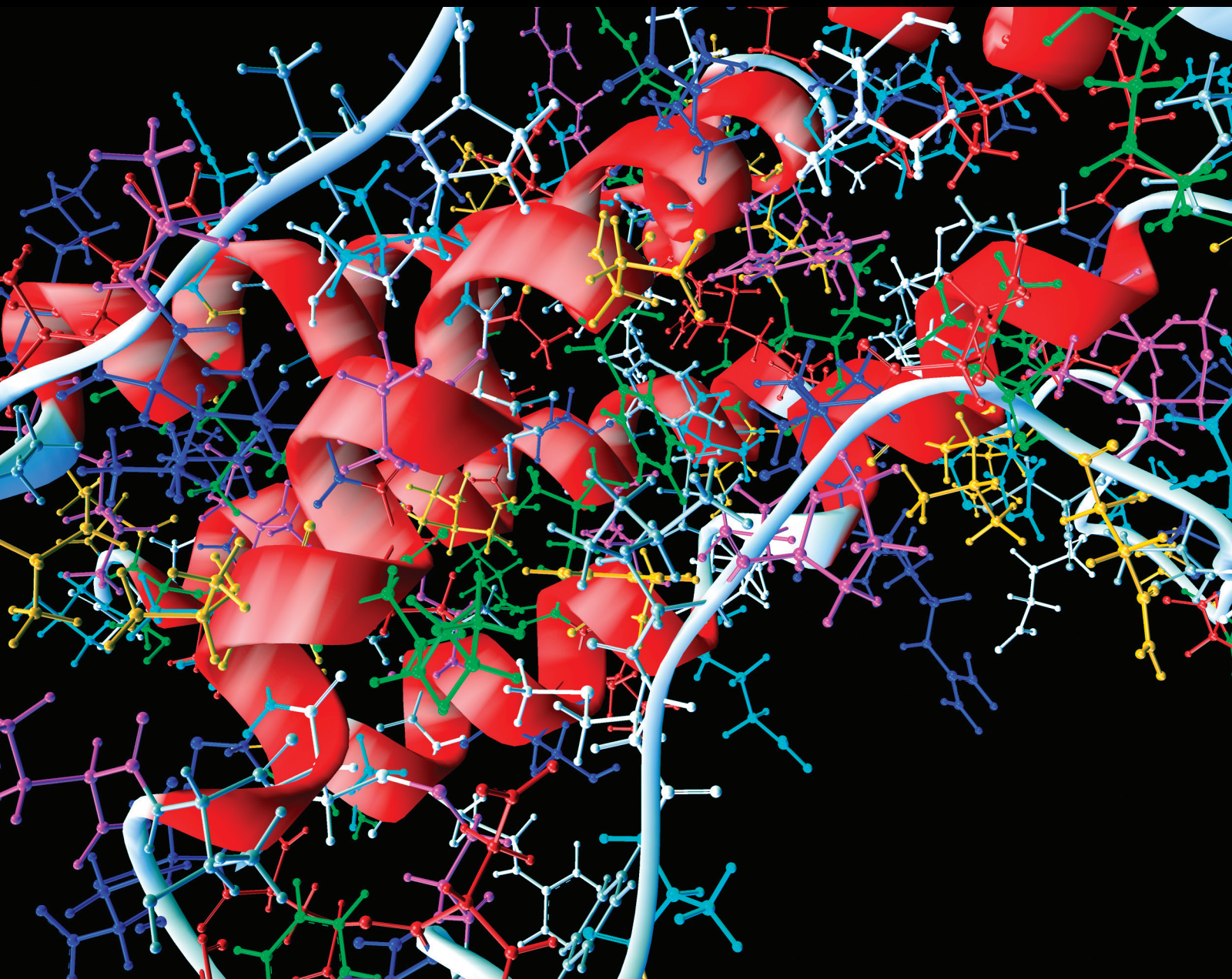


Predictive Models of Tumour Response to Treatment Using Functional Imaging Techniques

Guest Editors: Loredana G. Marcu, Eva Bezak, Iuliana Toma-Dasu,
and Alexandru Dasu





Predictive Models of Tumour Response to Treatment Using Functional Imaging Techniques

Computational and Mathematical Methods in Medicine

Predictive Models of Tumour Response to Treatment Using Functional Imaging Techniques

Guest Editors: Loredana G. Marcu, Eva Bezak,
Iuliana Toma-Dasu, and Alexandru Dasu



Copyright © 2015 Hindawi Publishing Corporation. All rights reserved.

This is a special issue published in “Computational and Mathematical Methods in Medicine.” All articles are open access articles distributed under the Creative Commons Attribution License, which permits unrestricted use, distribution, and reproduction in any medium, provided the original work is properly cited.

Editorial Board

Emil Alexov, USA
Elena Amato, Italy
Konstantin G. Arbeev, USA
Georgios Archontis, Cyprus
Chris Bauch, Canada
Lynne Bilston, Australia
Konstantin B. Blyuss, UK
Thierry Busso, France
Xueyuan Cao, USA
Carlos Castillo-Chavez, USA
Carlo Cattani, Italy
Shengyong Chen, China
Phoebe Chen, Australia
Hsiu-Hsi Chen, Taiwan
Wai-Ki Ching, Hong Kong
Nadia A. Chuzhanova, UK
Maria N. D. S. Cordeiro, Portugal
Irena Cosic, Australia
Fabien Crauste, France
William Crum, UK
Getachew Dagne, USA
Qi Dai, China
Justin Dauwels, Singapore
Didier Delignières, France
Thomas Desaive, Belgium
Georges El Fakhri, USA
Issam El Naqa, USA
Ricardo Femat, Mexico
Marc T. Figge, Germany
Alfonso T. García-Sosa, Estonia
Amit Gefen, Israel
Humberto G.-Díaz, Spain
Igor I. Goryanin, Japan
Marko Gosak, Slovenia

Dinesh Gupta, India
Damien Hall, Australia
Volkhard Helms, Germany
Akimasa Hirata, Japan
Roberto Hornero, Spain
Tingjun Hou, China
Seiya Imoto, Japan
Sebastien Incerti, France
Abdul Salam Jarrah, USA
Hsueh-Fen Juan, Taiwan
R. Karaman, Palestinian Authority
Lev Klebanov, Czech Republic
Andrzej Kloczkowski, USA
Xiang-Yin Kong, China
Xiangrong Kong, USA
Zuofeng Li, USA
Qizhai Li, China
Chung-Min Liao, Taiwan
Quan Long, UK
Reinoud Maex, France
Valeri Makarov, Spain
Kostas Marias, Greece
Richard J. Maude, Thailand
Panagiotis Mavroidis, USA
Georgia Melagraki, Greece
Michele Migliore, Italy
John Mitchell, UK
Arnold B. Mitnitski, Canada
Michele Nichelatti, Italy
Ernst Niebur, USA
Kazuhisa Nishizawa, Japan
Hugo Palmans, UK
Francesco Pappalardo, Italy
Matjaz Perc, Slovenia

Jesús Picó, Spain
Giuseppe Pontrelli, Italy
Mohamad A. Pourhoseingholi, Iran
Christopher Pretty, New Zealand
Ravi Radhakrishnan, USA
John J. Rice, USA
Xu Shen, China
Simon A. Sherman, USA
E. Albert Siegbahn, Sweden
Sivabal Sivaloganathan, Canada
Dong Song, USA
Emiliano Spezi, UK
Tianhai Tian, Australia
Tianhai Tian, Australia
Jerzy Tiuryn, Poland
Nestor V. Torres, Spain
Nelson J. Trujillo-Barreto, Cuba
Po-Hsiang Tsui, Taiwan
Gabriel Turinici, France
Kutlu O. Ulgen, Turkey
Edelmira Valero, Spain
Liangjiang Wang, USA
Ruisheng Wang, USA
David A. Winkler, Australia
Guang Wu, China
Chen Yanover, Israel
Xiaojun Yao, China
Kaan Yetilmesoy, Turkey
Henggui Zhang, UK
Huaguang Zhang, China
Xiaoqi Zheng, China
Yunping Zhu, China

Contents

Predictive Models of Tumour Response to Treatment Using Functional Imaging Techniques,

Loredana G. Marcu, Eva Bezak, Iuliana Toma-Dasu, and Alexandru Dasu

Volume 2015, Article ID 571351, 2 pages

Towards Multidimensional Radiotherapy: Key Challenges for Treatment Individualisation,

Iuliana Toma-Dasu and Alexandru Dasu

Volume 2015, Article ID 934380, 8 pages

PET-Specific Parameters and Radiotracers in Theoretical Tumour Modelling, Matthew Jennings,

Loredana G. Marcu, and Eva Bezak

Volume 2015, Article ID 415923, 11 pages

Multimodality Functional Imaging in Radiation Therapy Planning: Relationships between Dynamic Contrast-Enhanced MRI, Diffusion-Weighted MRI, and 18F-FDG PET, Moisés Mera Iglesias,

David Aramburu Núñez, José Luis del Olmo Claudio, Antonio López Medina, Iago Landesa-Vázquez,

Francisco Salvador Gómez, Brandon Driscoll, Catherine Coolens, José L. Alba Castro, and Victor Muñoz

Volume 2015, Article ID 103843, 10 pages

Modeling the Relationship between Fluorodeoxyglucose Uptake and Tumor Radioresistance as a Function of the Tumor Microenvironment, Jeho Jeong and Joseph O. Deasy

Volume 2014, Article ID 847162, 7 pages

Hypoxia in Head and Neck Cancer in Theory and Practice: A PET-Based Imaging Approach,

Loredana G. Marcu, Wendy M. Harriss-Phillips, and Sanda M. Filip

Volume 2014, Article ID 624642, 13 pages

Delay Differential Model for Tumour-Immune Response with Chemoimmunotherapy and Optimal Control, F. A. Rihan, D. H. Abdelrahman, F. Al-Maskari, F. Ibrahim, and M. A. Abdeen

Volume 2014, Article ID 982978, 15 pages

Editorial

Predictive Models of Tumour Response to Treatment Using Functional Imaging Techniques

Loredana G. Marcu,^{1,2} Eva Bezak,^{2,3} Iuliana Toma-Dasu,⁴ and Alexandru Dasu⁵

¹Faculty of Science, University of Oradea, 410087 Oradea, Romania

²School of Chemistry & Physics, University of Adelaide, Adelaide, SA 5000, Australia

³Department of Physics, Royal Adelaide Hospital, Adelaide, SA 5000, Australia

⁴Medical Radiation Physics Division, Stockholm University and Karolinska Institutet, 171 76 Stockholm, Sweden

⁵Department of Medical and Health Sciences, Radiation Physics, Linköping University, 581 85 Linköping, Sweden

Correspondence should be addressed to Loredana G. Marcu; loredana@marcunet.com

Received 14 December 2014; Accepted 14 December 2014

Copyright © 2015 Loredana G. Marcu et al. This is an open access article distributed under the Creative Commons Attribution License, which permits unrestricted use, distribution, and reproduction in any medium, provided the original work is properly cited.

The aim of the current special issue was to bring together articles on various aspects of tumour modelling focusing on treatment response and prediction of clinical outcome based on functional imaging techniques.

Together with technological and radiobiological advances, tumour modelling is an emerging area of oncology, which plays a key role in predicting treatment outcome in cancer patients. Despite the complexity of tumour biology and its microenvironment, computational and mathematical models of virtual cancer behaviour and response to treatment are successfully developed and employed for clinical research. A mathematical (delay differential) model with optimal control for tumour-immune response with chemoimmunotherapy is presented by F. A. Rihan et al. in their research paper that describes the interaction of tumour cells and immune response cells with external therapy. In their model, the authors propose a numerical technique to solve the optimal control problem and identify the best strategy to combine chemotherapy and immunotherapy in order to minimise tumour load while maximising the strength of the immune system.

Current diagnostic and imaging methods provide in-depth metabolic information that can be employed for tumour modelling. Latest technical and molecular advances in the field of nuclear medicine offer new possibilities in functional imaging, overcoming some of the confines

imposed by previous diagnostic techniques. Positron emission tomography (PET) is the most advanced technology designed to provide metabolic information of disease, treatment monitoring, and also evaluation of treatment outcome. Together with other quantitative imaging techniques, such as dynamic contrast-enhanced MRI, PET is a promising diagnostic tool assisting in patient stratification for specific therapies, evaluation of drug efficacy, assessment of chemo- and radiotherapy outcome, and prediction of survival.

This research idea is underlined in the paper by M. Jennings et al., which focuses on PET-specific parameters and radiotracers in theoretical tumour modelling. The work reviews the use of PET/CT information applied to *in silico* models of tumour growth, development, and behaviour during treatment. Tumour-related parameters such as cell proliferation, hypoxia, angiogenesis, and pH as well as PET/CT-specific biophysical parameters by means of SUV (standardized uptake value) and Hounsfield units are revisited in the context of computational modelling of complex processes involving tumour kinetics and treatment outcome.

While several PET radiotracers have been developed for clinical use to target specific tumour properties, FDG (fluorodeoxyglucose) continues to be the most commonly used radionuclide in functional imaging as it offers unique information for tumour detection, staging, target definition, and response monitoring during radio- and chemotherapy.

In this special issue, J. Jeong and J. O. Deasy have modelled the relationship between FDG uptake and tumour radioresistance as a function of the tumour microenvironment. The mechanistic model has considered cellular status to be dictated by glucose and oxygen content, showing that cells in the intermediate stress state (that receive glucose but not oxygen) present an increased avidity of FDG when compared to well-oxygenated cells. The role of hypoxia and the current status of hypoxia imaging including PET-specific markers are discussed by L. G. Marcu et al. in their review paper written in the context of head and neck cancer. Hypoxia-specific PET markers have been implemented in several clinical trials to quantify hypoxic tumour subvolumes for dose painting and personalised treatment planning. Tracer pharmacokinetics and PET-derived functional parameters serve as important input data for *in silico* models that aim to simulate or interpret the acquired image. The paper discusses two main streams of PET tracer modelling: (1) models of specific tracer/oxygen dynamics with the aim of simulating PET images leading to results that are in close agreement with real PET images and (2) utilisation of PET data within a separate tumour model with the aim of creating a more specific model that is predictive of response to treatment. The authors have collated analytical compartment models of tracer pharmacokinetics, stochastic models of treatment response using probability distribution functions, and reports on model predictions within clinical radiotherapy planning systems of dose distribution. A pertinent conclusion of the review is that the role of computer models based on functional imaging techniques in understanding patient-specific tumour behaviour is effusively justified.

The challenge of hypoxia in cancer management is further analysed by M. M. Iglesias et al. in a research article looking at the multimodality functional imaging in radiotherapy planning and the relationship between dynamic contrast-enhanced (DCE) MRI, diffusion-weighted MRI, and FDG-PET in order to develop predictive individualised models of tumour response to radiotherapy in head and neck cancer patients. For an optimal biologically guided radiotherapy, to obtain relevant datasets on tumour hypoxia and cellular density, there is a need to understand the correlations and interactions between various functional imaging modalities. Parameters such as SUV (PET), Hounsfield units, dose, ADC (apparent diffusion coefficient) maps (MRI), and contrast exchange coefficients (DCE-MRI) have been recorded for each patient from the study and the relationship between parameters analysed. The authors concluded that the above functional parameters based on different image datasets are valuable in describing in a complex manner tumour oxygenation and vascularisation, cell density, and tumour malignancy offering, therefore, treatment personalisation and optimisation.

A central motif of today's cancer management is personalised treatment planning and delivery. While this trend is featured in all papers of the current special issue, a more focused view upon treatment individualisation via multidimensional radiotherapy is presented in the work of I. Toma-Dasu and A. Dasu. According to the authors, the key approach to maximise the individualisation of treatment is by

combining multiparameter information from imaging with predictive information from biopsies and molecular analyses and also by monitoring tumour response to treatment. The emphasis of the paper is on biologically adapted radiation therapy (BIOART), which is based on both pretreatment conditions and intrinsic responsiveness assessed using functional imaging techniques. The authors suggest that the BIOART concept should replace the simple dose painting approach for a more optimal management of radioresistant subvolumes within the BTV (biological target volume). Functional imaging is shown to have the potential to provide a paradigm shift in treatment planning and optimisation that extends beyond target definition.

In silico modelling in cancer research was and continues to be a very important tool of treatment simulation and optimisation, contributing to a more personalised medicine for an improved patient outcome. The use of computational models for treatment assessment and outcome prediction is fast growing and the power of *in silico* models as preclinical tools becomes acknowledged. Therefore, multidisciplinary research leading to predictive models of tumour response to treatment using functional imaging techniques needs to be encouraged to enable further developments in the diagnostic and treatment of cancer.

Loredana G. Marcu
Eva Bezak
Iuliana Toma-Dasu
Alexandru Dasu

Review Article

Towards Multidimensional Radiotherapy: Key Challenges for Treatment Individualisation

Iuliana Toma-Dasu¹ and Alexandru Dasu²

¹Medical Radiation Physics, Stockholm University and Karolinska Institutet, P.O. Box 260, 171 76 Stockholm, Sweden

²Department of Radiation Physics and Department of Medical and Health Sciences, Linköping University, 581 83 Linköping, Sweden

Correspondence should be addressed to Iuliana Toma-Dasu; iuliana.livia.dasu@ki.se

Received 4 July 2014; Accepted 3 September 2014

Academic Editor: Eva Bezak

Copyright © 2015 I. Toma-Dasu and A. Dasu. This is an open access article distributed under the Creative Commons Attribution License, which permits unrestricted use, distribution, and reproduction in any medium, provided the original work is properly cited.

Functional and molecular imaging of tumours have offered the possibility of redefining the target in cancer therapy and individualising the treatment with a multidimensional approach that aims to target the adverse processes known to impact negatively upon treatment result. Following the first theoretical attempts to include imaging information into treatment planning, it became clear that the biological features of interest for targeting exhibit considerable heterogeneity with respect to magnitude, spatial, and temporal distribution, both within one patient and between patients, which require more advanced solutions for the way the treatment is planned and adapted. Combining multiparameter information from imaging with predictive information from biopsies and molecular analyses as well as in treatment monitoring of tumour responsiveness appears to be the key approach to maximise the individualisation of treatment. This review paper aims to discuss some of the key challenges for incorporating into treatment planning and optimisation the radiobiological features of the tumour derived from pretreatment PET imaging of tumour metabolism, proliferation, and hypoxia and combining them with intratreatment monitoring of responsiveness and other predictive factors with the ultimate aim of individualising the treatment towards the maximisation of response.

1. Introduction

The progress and technological development of functional and molecular techniques for imaging tumours have offered the possibility of redefining the target in radiation therapy and devising the treatment in an innovative manner. Fourteen years have passed since Ling et al. [1] introduced the concept of biological target volume (BTV) encompassing the multidimensional physiological and functional information provided by the new imaging techniques. At the end of their seminal paper on multidimensional radiotherapy, the authors challenged the research and clinical communities to define a biological target volume and apply it by the year 2010 moving towards evidence-based multidimensional radiation therapy by conforming the physical dose distribution to the radiobiological features of the target that may be derived from molecular and functional imaging. Research has been conducted towards this aim, but the current practice in radiation therapy is still, at its best, based on the physical optimisation of the dose distribution according to the

anatomical information regarding the localisation and the extent of the tumour and the normal tissue. The routine planning in clinical radiation treatment does not generally take into account the particular radiation sensitivity of the tumour of an individual patient or the spatial and temporal heterogeneity of tumour resistance. However, it is well known that these aspects may be the causes for treatment failure for a considerable fraction of the nonresponding patients, as the standard dose prescription does not ensure sufficiently curative doses to counteract the radiation resistance of the tumour. Among these adverse factors one has to count the variations in cellular density from tumour to tumour, the proliferation characteristics of the tumour cells, and the distinct microenvironmental characteristics of the tumours.

A broad array of techniques could now be used to determine the morphologic, functional, and molecular features of tumours and normal tissues. Among these, positron emission tomography (PET) has the advantage of being almost noninvasive as it uses tracers that are usually metabolic substitutes

and is quite sensitive since quite low concentrations of tracers are required for imaging. Furthermore, several tracers are already available for investigating various processes [2]. The most quoted tumour phenotypes that could be integrated with the CT-defined gross tumour volume (GTV) to obtain the BTV are the tumour metabolism, proliferation, hypoxia, and angiogenesis. Consequently, several methods have been proposed for providing the relevant biological information on metabolic, biochemical, and physiological factors resulting in a new approach for the way the treatment is planned [3, 4]. However, it became clear that tumours do not contain one biological target volume to which a homogeneous dose could be prescribed, but instead the biological features of interest for targeting exhibit considerable heterogeneity with respect to magnitude, spatial, and temporal distribution, both within one patient and between patients.

This review paper aims to add to these conceptual solutions by discussing some of the key challenges for incorporating the radiobiological features of the tumour into the models for predicting the treatment outcome or for counteracting the adverse tumour control factors based on PET imaging of tumour metabolism, proliferation, and hypoxia.

2. PET Imaging of Key Tumour Phenotypes and Corresponding Models for Dose Painting

Several modelling studies have presented various approaches with different degrees of complexity to include the imaging information into treatment planning. Although in some cases more than one type of PET image was available, to the best of our knowledge the models currently proposed in the literature did not focus on more than one of the adverse tumour control factors at a time for determining the BTV and its subregions and for addressing the radiation resistance associated with them. With very large extent, the majority of the models focused on tumour hypoxia since it is one of the most important factors that determine the response of the tumour to radiation therapy [5–8]. A common approach is to delineate a hypoxic subtarget in the tumour based on PET tracers specifically designed for imaging the tumour oxygenation such as [^{18}F]Fluoromisonidazole ([^{18}F]FMISO), [^{18}F]Fluoroetamidazole ([^{18}F]FETA), [^{18}F]Fluoroazomycin-arabinofuranoside ([^{18}F]FAZA), or the nonimidazoles compound Cu(II)-diacetyl-bis-N-(4)-methylthiosemicarbazone (Cu-ATSM) and prescribe an escalation of the dose according to available radiation therapy techniques and considering the tolerance of the normal tissues around the tumour [9–11]. However the risk of using such an empirical approach is that the prescribed dose might not be large enough to counteract the hypoxic radiation resistance and therefore the method might fail to bring the expected results in clinical settings. Other approaches recommended highly heterogeneous dose distributions based on a linear increase of the prescribed dose according to the signal intensity in the PET image [12, 13] or, as a result of redistributing the dose to the target, by increasing the dose to the hypoxic voxels while decreasing the prescribed dose to the remaining

voxels in the tumour [14, 15]. More complex approaches for heterogeneous dose prescription make use of dynamic PET information [16]. However, heterogeneous dose distributions are at risk of failing to provide the expected results for cases of dynamic hypoxia as have indeed been seen in clinical patients [17] since changes in the spatial distribution of hypoxia could easily lead to mismatches between the hypoxic subregions and the planned hotspots in the dose distribution. Alternative approaches in which the impact of local changes in the oxygenation of the tumour were also theoretically explored and subsequently tested for feasibility [18, 19].

Another factor that reduces treatment effectiveness among the physiological factors that influence the response to treatment is tumour cell proliferation. Cell proliferation and especially accelerated repopulation that is seen in rapidly growing tumours like head-and-neck carcinomas are regarded as adverse factors for the success of radiotherapy because they increase the population of cells that could regrow the tumour and therefore need to be sterilised with radiation [20]. This warrants the noninvasive investigation of tumour proliferation as a potential target to increase local control. Proliferation and/or metabolic PET tracers may be used to image and quantify the tumour regions with increased proliferation. They can also be used to predict and evaluate the response to treatment and if necessary to adapt or improve the therapy.

Many tumours also have an increased glycolytic metabolism compared to normal tissues [21]. This means that a radioactive analogue of glucose will be easily taken up in tumours and the tumour burden could be detected through the difference in activity concentration. This is the case of [^{18}F]Fluorodeoxyglucose ([^{18}F]FDG) that led to PET being largely used for improving the detection and staging of cancers as well as for target delineation and the evaluation of treatment [22–24]. Other tracers, like ^{11}C -acetate, would have to be considered for non-FDG-avid tumours, offering yet another facet of tumour metabolism [25–28].

Furthermore, some studies showed that the uptake of FDG in slowly proliferating tumours is generally lower than in rapidly growing, poorly differentiated tumours [2], suggesting an indirect correlation with the proliferating potential of the tumours. However, FDG is not a dedicated tracer for tumour proliferation and therefore some regions with increased glycolytic metabolism such as inflammations will also show a high FDG uptake and will be imaged, decreasing the quality of the information provided by FDG-PET. Due to these limitations other biomarkers have been proposed for specifically characterising tumour proliferation [2], such as [^{18}F]3'-deoxy-3'-fluorotymidine ([^{18}F]FLT). In comparison to hypoxia, little attention has been paid to developing models for the inclusion of proliferation information into treatment planning. To the best of our knowledge, there is only one study in which the possibility of including quantitative imaging of tumour proliferation and cell density into the radiobiological evaluation and optimisation of treatment planning was theoretically explored [29].

3. Multitracer Spatial and Temporal Distributions and TCP Models

The most common hypotheses on which a dose painting approach is generally based are the following: local recurrence is related to resistant foci not eradicated by the currently prescribed and delivered uniform doses, noninvasive functional and molecular imaging allows mapping the target in terms of radiation resistance and progress in treatment planning and radiation delivery allows nonhomogeneous target irradiation while the irradiation of the normal tissue and organs-at-risk (OARs) is kept below the tolerance levels. The subsequent steps that are taken when proposing a strategy for dose painting are to determine what functional noninvasive methods can be used for imaging specific tumour phenotypes related to local control or risk of relapse after (chemo)radiotherapy, to determine the response function(s) that would allow the quantitative interpretation of the image or images translated into a painting strategy, and finally to determine how to prescribe and deliver the dose, as dose boosting or as in the manner generally known as dose painting by numbers.

The larger variability in the known approaches for performing treatment planning based on functional imaging is related to the interpretation of the images and their translation into dose prescription. Furthermore, for the case of combined information regarding the key factors that should be accounted for when attempting dose painting based on functional PET imaging, tumour metabolism, proliferation, and hypoxia, the complexity of the problem has prevented up to the present date the proposal of quantitative radiobiological models to simultaneously account for them.

The most general approach for modelling the tumour response if information about the key features regarding tumour resistance to radiation is available as derived from functional imaging is to calculate the tumour control probability (TCP) at voxel level and then to integrate the response over the whole target structure. Thus, assuming an initial distribution of cell density $n_0(\mathbf{r})$ and a distribution of cell survival following the treatment $SF(\mathbf{r})$, the probability of controlling the tumour is given by the following expression [18]:

$$\text{TCP} = \exp \left[- \int_{\mathbf{r}} n_0(\mathbf{r}) \cdot SF(\mathbf{r}) d\mathbf{r} \right]. \quad (1)$$

If the linear quadratic (LQ) model [30–32] adapted for proliferation [33] is used for describing the cellular survival, the fraction of cells surviving in a voxel \mathbf{r} in the tumour is given by

$$SF(\mathbf{r}) = \prod_{i=1}^n \exp \left[-\alpha(\mathbf{r}) \cdot d_i(\mathbf{r}) - \beta(\mathbf{r}) \cdot d_i^2(\mathbf{r}) \right] \cdot \exp \left[\frac{T \ln(2)}{\text{TD}(\mathbf{r})} \right], \quad (2)$$

where n is the number of fractions, $d_i(\mathbf{r})$ is the dose in fraction i in voxel \mathbf{r} , $\alpha(\mathbf{r})$ and $\beta(\mathbf{r})$ are the LQ parameters describing the radiosensitivity in voxel \mathbf{r} , T is the treatment duration, and

$\text{TD}(\mathbf{r})$ is the cell doubling time in the voxel \mathbf{r} . If the variation in radiation sensitivity is related to the oxygenation of the cells, $\alpha(\mathbf{r})$ and $\beta(\mathbf{r})$ could be expressed as functions of the α and β parameters relevant for well oxygenated cells and the oxygen tension-dependent modification factors, OMF, and thus (2) becomes

$$SF(\mathbf{r}) = \prod_{i=1}^n \exp \left[-\frac{\alpha}{\text{OMF}(pO_2(\mathbf{r}))} \cdot d_i(\mathbf{r}) - \frac{\beta}{\text{OMF}^2(pO_2(\mathbf{r}))} \cdot d_i^2(\mathbf{r}) \right] \cdot \exp \left[\frac{T \ln(2)}{\text{TD}(\mathbf{r})} \right]. \quad (3)$$

OMF($pO_2(\mathbf{r})$) is given by the following expression:

$$\text{OMF}(pO_2(\mathbf{r})) = \text{OMF}_{\max} \frac{k + pO_2(\mathbf{r})}{k + \text{OMF}_{\max} pO_2(\mathbf{r})}, \quad (4)$$

where OMF_{\max} is the maximum protection achieved in the absence of oxygen and k is a reaction constant as described by Alper and Howard-Flanders [34].

In these conditions, the probability for controlling the tumour could be written as

$$\begin{aligned} \text{TCP} &= \exp \left\{ - \int_{\mathbf{r}} n_0(\mathbf{r}) \cdot \prod_{i=1}^n \exp \left[-\frac{\alpha}{\text{OMF}(pO_2(\mathbf{r}))} \cdot d_i(\mathbf{r}) - \frac{\beta}{\text{OMF}^2(pO_2(\mathbf{r}))} \cdot d_i^2(\mathbf{r}) \right] \cdot \exp \left[\frac{T \ln(2)}{\text{TD}(\mathbf{r})} \right] d\mathbf{r} \right\}. \end{aligned} \quad (5)$$

Several proposals exist in the literature regarding the way the parameters $n_0(\mathbf{r})$, $\text{TD}(\mathbf{r})$, and $\text{OMF}(pO_2(\mathbf{r}))$ could be derived from PET images. Thus, the density of the clonogenic cells in the beginning of the treatment could be derived from a FDG PET image based on the assumption that the enhanced FDG uptake should correspond to areas of higher density of glucose-avid clonogens [35]. As FLT is a marker taken up by the cells and phosphorylated by thymidine kinase 1 (TK1) which is an enzyme closely tied to cellular proliferation, it has been postulated that the retention of FLT within the cells provides a measure of cellular proliferation [36, 37]. The parameters used for describing the relationship between radiation sensitivity and tumour oxygenation could be derived based on the relative uptake of hypoxia-specific PET markers for various oxygen tensions, as proposed by Toma-Dasu et al. [38, 39], and subsequently tested with respect to its feasibility based on FMISO PET [19]. Thus, if FDG, FLT, and FMISO images of the tumour would be available before the start of the treatment and the relationships between the tracers uptake and $n_0(\mathbf{r})$, $\text{TD}(\mathbf{r})$, and $\text{OMF}(pO_2(\mathbf{r}))$ would also be

known, (5) could be used to determine the heterogeneous dose distribution that should be delivered for achieving a defined level of TCP.

Nevertheless, the practical implementation of this approach towards the complex BTV concept proposed by Ling et al. [1] is faced with several potential problems that may not be easily solved. Thus, one key problem is the fact that the required information about the biological parameters of interest would in fact be derived from PET images taken at different time points extending over several days to allow for the clearance of the different tracers. Therefore, assuming for example that the FDG PET image is taken at the time point t_1 before the start of the treatment while FMISO and FLT images are taken at t_2 and t_3 , respectively, (5) should be rewritten as

$$\begin{aligned} \text{TCP} &= \exp \left\{ - \int_{\mathbf{r}} n_0(\mathbf{r}, t_1) \right. \\ &\quad \cdot \prod_{i=1}^n \exp \left[- \frac{\alpha}{\text{OMF}(pO_2(\mathbf{r}, t_2))} \cdot d_i(\mathbf{r}) \right. \\ &\quad \quad \left. \left. - \frac{\beta}{\text{OMF}^2(pO_2(\mathbf{r}, t_2))} \cdot d_i^2(\mathbf{r}) \right] \right. \\ &\quad \left. \cdot \exp \left[\frac{T \ln(2)}{\text{TD}(\mathbf{r}, t_3)} \right] d\mathbf{r} \right\}. \end{aligned} \quad (6)$$

The expression in (6) shows that in reality it is quite difficult to speak about a time-independent BTV, given the spatial and temporal heterogeneity of the parameters determining the tumour control probability. Furthermore, the different biological processes that have to be incorporated are seldom coinciding in space [40, 41] meaning that several boost volumes would have to be defined, possibly with different boost levels.

The temporal stability and the reproducibility of the signal in the images before the start of the treatment given by the technical limitations of the imaging method, but, moreover, by the dynamics of the biological system that is imaged, may add yet another layer of complication to the already challenging task of multiparameter mapping of the target with respect to the radiobiological tumour features related to adverse response to (chemo)radiotherapy.

Last, but not least, the intrinsic radiosensitivity of the patients would have to be accounted for. Radiosensitivity parameters could be derived from clinical dose-response curves, but these are considered relevant for populations of patients which often exhibit considerable interpatient heterogeneity [42]. Instead one could use for example patient-specific parameters derived *in vitro* from biopsy materials as these were shown to better describe the response to treatment than generic or average parameters [43]. In the future such information may also be combined with predictive molecular assays providing quantitative information on the responsiveness of individuals to various forms of

treatment. Therefore, the true individualisation of treatment would have to determine the right prescription levels not only for the BTV or its equivalents, but also for the CTV and the GTV.

4. Integrated Biological Dose Prescription and Treatment Adaptation Based on Functional Imaging: Is It Time for a New Paradigm Shift?

Given the inherent limitations in defining the BTV and determining the dose prescription that should overcome the radioresistant foci within the BTV, the implementation of simple dose painting approaches might lead to disappointing results in clinical settings. Therefore, the present paper proposes a paradigm shift from focusing on the radiobiological dose prescription towards biologically adapted radiation therapy, BIOART, based on tumour responsiveness assessed with functional imaging. The BIOART concept, in a much wider acceptance, was introduced by Brahme in 2003 as Biologically Optimized *in vivo* Predictive Assay-Based Adaptive Radiation Therapy [3]. The original paper proposed that combining accurate knowledge about the delivered dose acquired with a PET camera based on the nuclear reactions induced in the patient by ions or high energy photons, together with information regarding the density of tumour clonogens at some early point during the treatment derived from two successive PET images, one taken before the start of the treatment and one after about one week, could be used to assess the responsiveness of the tumour to the treatment and consequently to adapt the treatment. Although very appealing, the monitoring of the dose delivery or rather of the production of positron emitting isotopes inside the patient following nuclear reactions, in case of ion therapy, or photonuclear reactions in case of photon irradiation with high energy photons, is not yet possible as a routine clinical procedure [44, 45], the accurate dose determination being achieved at its best through deformable dose registration based on repeated CBCT images during the course of the treatment. The effectiveness of this approach has however been debated on the grounds of the associated uncertainties [46].

The second component of the generic BIOART approach, monitoring of the tumour response by repeated PET images early during the treatment, is actually currently feasible. Indeed, several studies have explored qualitatively the correlations between variations in PET tracer uptake and treatment outcome [47–53]. Nevertheless, a very recent study on NSCLC imaged with FDG-PET before the start of (chemo)radiotherapy and during the second week of radiation therapy showed that it is feasible to determine a threshold value for the effective radiosensitivity of the patients that could be used quantitatively to divide the patients into good and poor responders to treatment as assessed by overall survival at 2 years after treatment [54]. These results therefore support the high potential of early assessment of treatment responsiveness and subsequent treatment individualisation by identifying the likely candidates for more aggressive

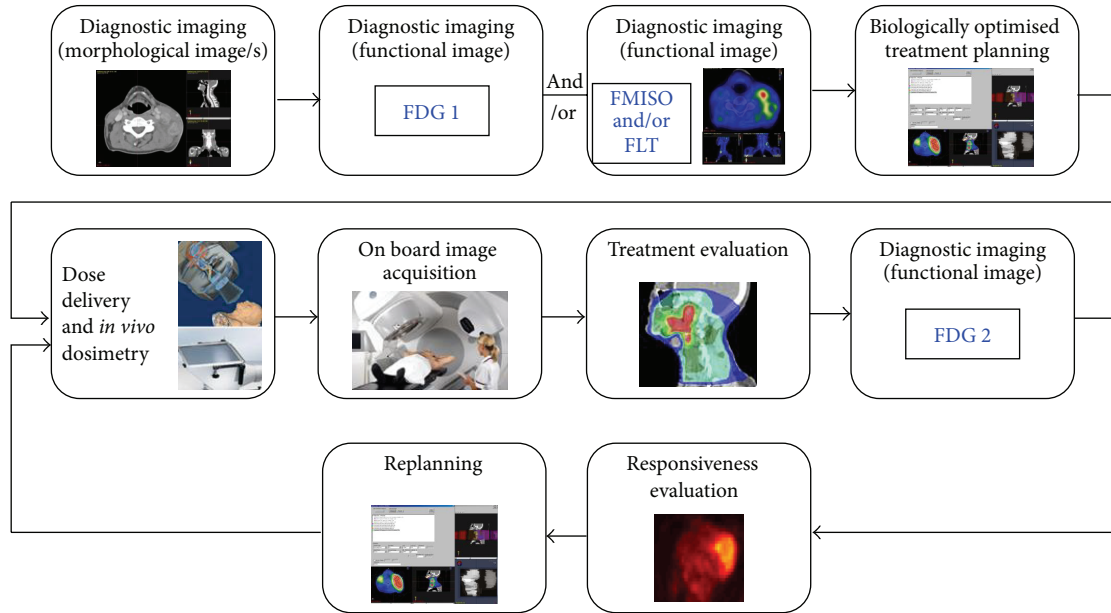


FIGURE 1: Schematic illustration of customised adaptive radiation therapy accounting for tumour hypoxia and/or proliferation.

strategies like dose escalation or combined therapies needed to increase the rate of local control.

This approach also provides another advantage, as repeated examinations in the same patient ensure that each patient is its own reference and does not require specific assumptions regarding the radiosensitivity. In fact, the approach opens the possibility of deriving effective radioreistance parameters that could eventually be used for treatment adaptation. Thus, assuming that the FDG images give a measure of the tumour burden, variations in signal intensities in individual voxels in the same patient would reflect changes in the density of functional clonogenic cells due to cell kill or proliferation. These and the dose distributions could then be used together with (2) or a simplified version of it to determine effective parameters for radiosensitivity [3, 54]. Other investigations of biologically adverse processes like hypoxia and proliferation could offer additional information that could be used for fine-tuning the parameters or included in the treatment optimisation process, provided that their intrinsic heterogeneity and dynamics are accounted for. A schematic illustration of the currently proposed approach for individualising the treatment and adapting it based on functional PET imaging is shown in Figure 1.

Several papers have shown that pretreatment FDG, FMISO, and FLT PET imaging might have not only prognostic values for indicating the likely course of the disease in the untreated individual, but also, more importantly in this setting, predictive values that might allow the selection of patients that would benefit from the chosen treatment [55–59]. However, proper patient selection and subsequent dose painting approaches for prescribing and delivering the dose do not guarantee the success of the treatment due to the large interpatient variability in response [56] and therefore they should be integrated in complex strategies for

the management of the tumour which include early monitoring of the response and treatment adaptation.

Central to responsiveness evaluation and treatment adaptation is the registration of images containing anatomic, functional, and dosimetric information. This is the result of a mathematical optimisation process using algorithms aimed at aligning the images through rigid or deformable transformations [60]. Several sources of uncertainties exist in this process, some intrinsic to the algorithms used and other originating in uncertainties or noise in the analysed images. As there is the risk that these uncertainties might interfere with the analysis of the information in the images, it is important to include them in a sensitivity analysis aimed at testing the robustness of the results or predictions, as done, for example, by Tilly et al. [61]. It has to be highlighted that best results are probably obtained when the assessment of the response has to take place not later than two weeks from the start of the treatment. This not only prevents the inflammatory response from dominating the information that could be retrieved from repeated FDG images, but also minimises the morphological changes that may be caused, for example, by tumour shrinkage or progression and which might require deformable registration algorithms that are more error prone and therefore more of a source of uncertainties.

The proposal above has mainly been concerned with using functional information from PET images for treatment monitoring and adaptation. Nevertheless, similar consideration might also apply for functional magnetic resonance imaging (MRI) that allows both qualitative and quantitative characterisation of clinical tumours and the subsequent mapping of the tumour response. Thus, parameters derived from diffusion-weighted MRI (DW-MRI) could offer information on tissue cellularity and may therefore be used for treatment response monitoring [62]. Other methods like dynamic

contrast-enhanced (DCE) imaging may be useful to obtain information on tissue vasculature [63], although it has been argued that tumour oxygenation might have a more complex dependence [64]. Proposals also exist for imaging lactate or choline levels in tumours as surrogates for hypoxia and proliferation [2].

5. Conclusions

There is no doubt that functional and molecular imaging have the potential to provide a paradigm shift in treatment planning and optimisation in cancer therapy that extends well beyond target definition. While multiparameter examinations will nevertheless provide valuable prognostic information for each patient, it is in unleashing the predictive power of the tracers that the true value of PET lies in modern radiotherapy. Thus, pretreatment investigations, possibly combined with predictive molecular information on the intrinsic features of each patient, will provide initial information on the dose levels needed to be included in the individual treatment plan and the likely therapeutic approaches. Subsequent examinations early during the treatment would then provide information on tumour responsiveness that may subsequently be used to determine the need for treatment adaptation taking into account the delivered dose distributions as well as adjuvant therapies, the effectiveness of which could also be assessed with this proposed approach. This may therefore be a simple and quite straightforward way to individualise treatment, considering not only the pretreatment condition of the patient, but also its intrinsic responsiveness and individual dose distributions that determine the need for later treatment adaptation. This is in fact the ultimate aim towards true individualisation of modern cancer treatment.

Conflict of Interests

The authors report no conflict of interests concerning the materials or methods used in this study or the findings in this paper.

Acknowledgments

Financial support from the Cancer Research Funds of Radiumhemmet, EU FP7 ARTFORCE, Linköping University, and the County Council of Östergötland is gratefully acknowledged.

References

- [1] C. C. Ling, J. Humm, S. Larson et al., "Towards multidimensional radiotherapy (MD-CRT): biological imaging and biological conformality," *International Journal of Radiation Oncology Biology Physics*, vol. 47, no. 3, pp. 551–560, 2000.
- [2] S. Apisarnthanarax and K. S. C. Chao, "Current imaging paradigms in radiation oncology," *Radiation Research*, vol. 163, no. 1, pp. 1–25, 2005.
- [3] A. Brahme, "Biologically optimized 3-dimensional in vivo predictive assay-based radiation therapy using positron emission tomography-computerized tomography imaging," *Acta Oncologica*, vol. 42, no. 2, pp. 123–136, 2003.
- [4] S. M. Bentzen, "Theragnostic imaging for radiation oncology: dose-painting by numbers," *The Lancet Oncology*, vol. 6, no. 2, pp. 112–117, 2005.
- [5] M. Nordmark, M. Overgaard, and J. Overgaard, "Pretreatment oxygenation predicts radiation response in advanced squamous cell carcinoma of the head and neck," *Radiotherapy and Oncology*, vol. 41, no. 1, pp. 31–39, 1996.
- [6] D. M. Brizel, G. S. Sibley, L. R. Prosnitz, R. L. Scher, and M. W. Dewhurst, "Tumor hypoxia adversely affects the prognosis of carcinoma of the head and neck," *International Journal of Radiation Oncology Biology Physics*, vol. 38, no. 2, pp. 285–289, 1997.
- [7] J. Overgaard, "Clinical evaluation of nitroimidazoles as modifiers of hypoxia in solid tumors," *Oncology Research*, vol. 6, no. 10–11, pp. 509–518, 1994.
- [8] P. Vaupel and A. Mayer, "Hypoxia in cancer: significance and impact on clinical outcome," *Cancer and Metastasis Reviews*, vol. 26, no. 2, pp. 225–239, 2007.
- [9] K. S. C. Chao, W. R. Bosch, S. Mutic et al., "A novel approach to overcome hypoxic tumor resistance: Cu-ATSM-guided intensity-modulated radiation therapy," *International Journal of Radiation Oncology Biology Physics*, vol. 49, no. 4, pp. 1171–1182, 2001.
- [10] A.-L. Grosu, M. Souvatzoglou, B. Röper et al., "Hypoxia imaging with FAZA-PET and theoretical considerations with regard to dose painting for individualization of radiotherapy in patients with head and neck cancer," *International Journal of Radiation Oncology Biology Physics*, vol. 69, no. 2, pp. 541–551, 2007.
- [11] S. T. Lee and A. M. Scott, "Hypoxia positron emission tomography imaging with ¹⁸F-fluoromisonidazole," *Seminars in Nuclear Medicine*, vol. 37, no. 6, pp. 451–461, 2007.
- [12] M. Alber, F. Paulsen, S. M. Eschmann, and H. J. Machulla, "On biologically conformal boost dose optimization," *Physics in Medicine and Biology*, vol. 48, no. 2, pp. N31–N35, 2003.
- [13] S. K. Das, M. M. Miften, S. Zhou et al., "Feasibility of optimizing the dose distribution in lung tumors using fluorine-18-fluorodeoxyglucose positron emission tomography and single photon emission computed tomography guided dose prescriptions," *Medical Physics*, vol. 31, no. 6, pp. 1452–1461, 2004.
- [14] E. Malinen, A. Søvik, D. Hristov, O. S. Bruland, and D. R. Olsen, "Adapting radiotherapy to hypoxic tumours," *Physics in Medicine and Biology*, vol. 51, no. 19, pp. 4903–4921, 2006.
- [15] R. T. Flynn, S. R. Bowen, S. M. Bentzen, T. R. Mackie, and R. Jeraj, "Intensity-modulated X-ray (IMXT) versus proton (IMPT) therapy for theragnostic hypoxia-based dose painting," *Physics in Medicine and Biology*, vol. 53, no. 15, pp. 4153–4167, 2008.
- [16] D. Thorwarth, S.-M. Eschmann, F. Paulsen, and M. Alber, "Hypoxia dose painting by numbers: a planning study," *International Journal of Radiation Oncology Biology Physics*, vol. 68, no. 1, pp. 291–300, 2007.
- [17] S. Roels, P. Slagmolen, J. Nuyts et al., "Biological image-guided radiotherapy in rectal cancer: is there a role for FMISO or FLT, next to FDG?" *Acta Oncologica*, vol. 47, no. 7, pp. 1237–1248, 2008.
- [18] I. Toma-Đađu, A. Đađu, and A. Brahme, "Dose prescription and optimisation based on tumour hypoxia," *Acta Oncologica*, vol. 48, no. 8, pp. 1181–1192, 2009.

- [19] I. Toma-Dasu, J. Uhrdin, L. Antonovic et al., “Dose prescription and treatment planning based on FMISO-PET hypoxia,” *Acta Oncologica*, vol. 51, no. 2, pp. 222–230, 2012.
- [20] H. R. Whithers, J. M. G. Taylor, and B. Maciejewski, “The hazard of accelerated tumor clonogen repopulation during radiotherapy,” *Acta Oncologica*, vol. 27, no. 2, pp. 131–146, 1988.
- [21] P. Vaupel, F. Kallinowski, and P. Okunieff, “Blood flow, oxygen and nutrient supply, and metabolic microenvironment of human tumors: a review,” *Cancer Research*, vol. 49, no. 23, pp. 6449–6465, 1989.
- [22] V. Gregoire, “Is there any future in radiotherapy planning without the use of PET: unraveling the myth,” *Radiotherapy and Oncology*, vol. 73, no. 3, pp. 261–263, 2004.
- [23] D. L. Schwartz, E. C. Ford, J. Rajendran et al., “FDG-PET/CT-guided intensity modulated head and neck radiotherapy: a pilot investigation,” *Head and Neck*, vol. 27, no. 6, pp. 478–487, 2005.
- [24] V. Grégoire and A. Chiti, “Molecular imaging in radiotherapy planning for head and neck tumors,” *Journal of Nuclear Medicine*, vol. 52, no. 3, pp. 331–334, 2011.
- [25] C. L. Ho, S. C. H. Yu, and D. W. Yeung, “¹¹C-acetate PET imaging in hepatocellular carcinoma and other liver masses,” *Journal of Nuclear Medicine*, vol. 44, no. 2, pp. 213–221, 2003.
- [26] G. Sandblom, J. Sörensen, N. Lundin, M. Häggman, and P.-U. Malmström, “Positron emission tomography with C11-acetate for tumor detection and localization in patients with prostate-specific antigen relapse after radical prostatectomy,” *Urology*, vol. 67, no. 5, pp. 996–1000, 2006.
- [27] A. Sun, J. Sörensen, M. Karlsson et al., “¹¹C-acetate PET imaging in head and neck cancer—a comparison with ¹⁸F-FDG-PET: implications for staging and radiotherapy planning,” *European Journal of Nuclear Medicine and Molecular Imaging*, vol. 34, no. 5, pp. 651–657, 2007.
- [28] A. Sun, S. Johansson, I. Turesson, A. Dau, and J. Sörensen, “Imaging tumor perfusion and oxidative metabolism in patients with head-and-neck cancer using ¹¹C-acetate PET during radiotherapy: preliminary results,” *International Journal of Radiation Oncology Biology Physics*, vol. 82, no. 2, pp. 554–560, 2012.
- [29] A. Dasu, “Treatment planning optimisation based on imaging tumour proliferation and cell density,” *Acta Oncologica*, vol. 47, no. 7, pp. 1221–1228, 2008.
- [30] K. H. Chadwick and H. P. Leenhouts, “A molecular theory of cell survival,” *Physics in Medicine and Biology*, vol. 18, no. 1, pp. 78–87, 1973.
- [31] B. G. Douglas and J. F. Fowler, “Fractionation schedules and a quadratic dose effect relationship,” *British Journal of Radiology*, vol. 48, no. 570, pp. 502–504, 1975.
- [32] G. W. Barendsen, “Dose fraction, dose rate and iso-effect relationships for normal tissue responses,” *International Journal of Radiation Oncology Biology Physics*, vol. 8, no. 11, pp. 1981–1997, 1982.
- [33] J. F. Fowler, “The linear-quadratic formula and progress in fractionated radiotherapy,” *British Journal of Radiology*, vol. 62, no. 740, pp. 679–694, 1989.
- [34] T. Alper and P. Howard-Flanders, “Role of oxygen in modifying the radiosensitivity of *E. coli* B,” *Nature*, vol. 178, no. 4540, pp. 978–979, 1956.
- [35] G. Meijer, J. Steenhuijsen, M. Bal, K. De Jaeger, D. Schuring, and J. Theuws, “Dose painting by contours versus dose painting by numbers for stage II/III lung cancer: practical implications of using a broad or sharp brush,” *Radiotherapy and Oncology*, vol. 100, no. 3, pp. 396–401, 2011.
- [36] A. K. Buck, G. Halter, H. Schirrmeister et al., “Imaging proliferation in lung tumors with PET: ¹⁸F-FLT versus ¹⁸F-FDG,” *Journal of Nuclear Medicine*, vol. 44, no. 9, pp. 1426–1431, 2003.
- [37] D. L. Francis, A. Freeman, D. Visvikis et al., “In vivo imaging of cellular proliferation in colorectal cancer using positron emission tomography,” *Gut*, vol. 52, no. 11, pp. 1602–1606, 2003.
- [38] I. Toma-Dasu, J. Uhrdin, A. Dasu, and A. Brahme, “Therapy optimization based on non-linear uptake of PET tracers versus ‘linear dose painting,’” *IFMBE Proceedings I*, vol. 25, pp. 221–224, 2009.
- [39] I. Toma-Dasu and A. Dasu, “Biologically-optimised IMRT based on molecular imaging of tumour hypoxia—the impact of the tracer used,” *IFMBE Proceedings*, vol. 39, pp. 1742–1745, 2013.
- [40] P. Vera, P. Bohn, A. Edet-Sanson et al., “Simultaneous positron emission tomography (PET) assessment of metabolism with ¹⁸F-fluoro-2-deoxy-d-glucose (FDG), proliferation with ¹⁸F-fluoro-thymidine (FLT), and hypoxia with ¹⁸F-fluoro-misonidazole (F-miso) before and during radiotherapy in patients with non-small-cell lung cancer (NSCLC): a pilot study,” *Radiotherapy and Oncology*, vol. 98, no. 1, pp. 109–116, 2011.
- [41] T. J. Bradshaw, S. Yip, N. Jallow, L. J. Forrest, and R. Jeraj, “Spatiotemporal stability of Cu-ATSM and FLT positron emission tomography distributions during radiation therapy,” *International Journal of Radiation Oncology Biology Physics*, vol. 89, no. 2, pp. 399–405, 2014.
- [42] A. Daşu, I. Toma-Dasu, and J. F. Fowler, “Should single or distributed parameters be used to explain the steepness of tumour control probability curves?” *Physics in Medicine and Biology*, vol. 48, no. 3, pp. 387–397, 2003.
- [43] M. Hedman, T. Bjork-Eriksson, O. Brodin, and I. Toma-Dasu, “Predictive value of modelled tumour control probability based on individual measurements of in vitro radiosensitivity and potential doubling time,” *British Journal of Radiology*, vol. 86, no. 1025, Article ID 20130015, 2013.
- [44] J. Bauer, D. Unholtz, F. Sommerer et al., “Implementation and initial clinical experience of offline PET/CT-based verification of scanned carbon ion treatment,” *Radiotherapy and Oncology*, vol. 107, no. 2, pp. 218–226, 2013.
- [45] K. Frey, J. Bauer, D. Unholtz et al., “TPS(PET): a TPS-based approach for in vivo dose verification with PET in proton therapy,” *Physics in Medicine and Biology*, vol. 59, no. 1, pp. 1–21, 2014.
- [46] T. E. Schultheiss, W. A. Tome, and C. G. Orton, “Point/counterpoint: it is not appropriate to ‘deform’ dose along with deformable image registration in adaptive radiotherapy,” *Medical Physics*, vol. 39, no. 11, pp. 6531–6533, 2012.
- [47] E. Brun, E. Kjellen, J. Tennvall et al., “FDG pet studies during treatment: prediction of therapy outcome in head and neck squamous cell carcinoma,” *Head and Neck*, vol. 24, no. 2, pp. 127–135, 2002.
- [48] A. van Baardwijk, G. Bosmans, A. Dekker et al., “Time trends in the maximal uptake of FDG on PET scan during thoracic radiotherapy. A prospective study in locally advanced non-small cell lung cancer (NSCLC) patients,” *Radiotherapy and Oncology*, vol. 82, no. 2, pp. 145–152, 2007.
- [49] M. Hentschel, S. Appold, A. Schreiber et al., “Early FDG PET at 10 or 20 Gy under chemoradiotherapy is prognostic for locoregional control and overall survival in patients with head and neck cancer,” *European Journal of Nuclear Medicine and Molecular Imaging*, vol. 38, no. 7, pp. 1203–1211, 2011.
- [50] M. Massacesi, M. L. Calcagni, M. G. Spitilli et al., “¹⁸F-FDG PET-CT during chemo-radiotherapy in patients with non-small

cell lung cancer: the early metabolic response correlates with the delivered radiation dose,” *Radiation Oncology*, vol. 7, article 106, 2012.

- [51] W. van Elmpt, M. Öllers, A.-M. C. Dingemans, P. Lambin, and D. de Ruysscher, “Response assessment using ^{18}F -FDG PET early in the course of radiotherapy correlates with survival in advanced-stage non-small cell lung cancer,” *Journal of Nuclear Medicine*, vol. 53, no. 10, pp. 1514–1520, 2012.
- [52] J. K. Hoang, S. K. Das, K. R. Choudhury, D. S. Yoo, and D. M. Brizel, “Using FDG-PET to measure early treatment response in head and neck squamous cell carcinoma: quantifying intrinsic variability in order to understand treatment-induced change,” *The American Journal of Neuroradiology*, vol. 34, no. 7, pp. 1428–1433, 2013.
- [53] E. A. Usmanij, L. F. de Geus-Oei, E. G. C. Troost et al., “ ^{18}F -FDG PET early response evaluation of locally advanced non-small cell lung cancer treated with concomitant chemoradiotherapy,” *Journal of Nuclear Medicine*, vol. 54, no. 9, pp. 1528–1534, 2013.
- [54] I. Toma-Dasu, J. Uhrdin, A. Dasu, S. Carvalho, W. van Elmpt, and P. Lambin, “Evaluating tumour response of NSCLC patients with FDG-PET: potential for treatment individualisation,” *Radiotherapy and Oncology*, vol. 111, supplement 1, p. 364, 2014.
- [55] J. G. Rajendran, D. L. Schwartz, J. O’Sullivan et al., “Tumor hypoxia imaging with [F-18] fluoromisonidazole positron emission tomography in head and neck cancer,” *Clinical Cancer Research*, vol. 12, no. 18, pp. 5435–5441, 2006.
- [56] J. van Loon, A. van Baardwijk, L. Boersma, M. Öllers, P. Lambin, and D. de Ruysscher, “Therapeutic implications of molecular imaging with PET in the combined modality treatment of lung cancer,” *Cancer Treatment Reviews*, vol. 37, no. 5, pp. 331–343, 2011.
- [57] H. Quon and D. M. Brizel, “Predictive and prognostic role of functional imaging of head and neck squamous cell carcinomas,” *Seminars in Radiation Oncology*, vol. 22, no. 3, pp. 220–232, 2012.
- [58] H. J. W. L. Aerts, J. Bussink, W. J. G. Oyen et al., “Identification of residual metabolic-active areas within NSCLC tumours using a pre-radiotherapy FDG-PET-CT scan: a prospective validation,” *Lung Cancer*, vol. 75, no. 1, pp. 73–76, 2012.
- [59] M. Inubushi, T. Saga, M. Koizumi et al., “Predictive value of 3’-deoxy-3’-[^{18}F]fluorothymidine positron emission tomography/computed tomography for outcome of carbon ion radiotherapy in patients with head and neck mucosal malignant melanoma,” *Annals of Nuclear Medicine*, vol. 27, no. 1, pp. 1–10, 2013.
- [60] D. L. Hill, P. G. Batchelor, M. Holden, and D. J. Hawkes, “Medical image registration,” *Physics in Medicine and Biology*, vol. 46, no. 3, pp. R1–45, 2001.
- [61] D. Tilly, N. Tilly, and A. Ahnesjö, “Dose mapping sensitivity to deformable registration uncertainties in fractionated radiotherapy: applied to prostate proton treatments,” *BMC Medical Physics*, vol. 13, article 2, no. 1, 2013.
- [62] H. C. Thoeny and B. D. Ross, “Predicting and monitoring cancer treatment response with diffusion-weighted MRI,” *Journal of Magnetic Resonance Imaging*, vol. 32, no. 1, pp. 2–16, 2010.
- [63] T. Nielsen, T. Wittenborn, and M. R. Horsman, “Dynamic contrast-enhanced magnetic resonance imaging (DCE-MRI) in preclinical studies of antivasular treatments,” *Pharmaceutics*, vol. 4, no. 4, pp. 563–589, 2012.
- [64] A. Dasu and I. Toma-Dasu, “Vascular oxygen content and the tissue oxygenation: a theoretical analysis,” *Medical Physics*, vol. 35, no. 2, pp. 539–545, 2008.

Review Article

PET-Specific Parameters and Radiotracers in Theoretical Tumour Modelling

Matthew Jennings,^{1,2} Loredana G. Marcu,^{1,3} and Eva Bezak^{1,2}

¹School of Chemistry & Physics, University of Adelaide, Adelaide, SA 5000, Australia

²Department of Medical Physics, Royal Adelaide Hospital, Adelaide, SA 5000, Australia

³Faculty of Science, University of Oradea, 410087 Oradea, Romania

Correspondence should be addressed to Matthew Jennings; matthew.jennings@health.sa.gov.au

Received 17 July 2014; Accepted 15 September 2014

Academic Editor: Iuliana Toma-Dasu

Copyright © 2015 Matthew Jennings et al. This is an open access article distributed under the Creative Commons Attribution License, which permits unrestricted use, distribution, and reproduction in any medium, provided the original work is properly cited.

The innovation of computational techniques serves as an important step toward optimized, patient-specific management of cancer. In particular, *in silico* simulation of tumour growth and treatment response may eventually yield accurate information on disease progression, enhance the quality of cancer treatment, and explain why certain therapies are effective where others are not. *In silico* modelling is demonstrated to considerably benefit from information obtainable with PET and PET/CT. In particular, models have successfully integrated tumour glucose metabolism, cell proliferation, and cell oxygenation from multiple tracers in order to simulate tumour behaviour. With the development of novel radiotracers to image additional tumour phenomena, such as pH and gene expression, the value of PET and PET/CT data for use in tumour models will continue to grow. In this work, the use of PET and PET/CT information in *in silico* tumour models is reviewed. The various parameters that can be obtained using PET and PET/CT are detailed, as well as the radiotracers that may be used for this purpose, their utility, and limitations. The biophysical measures used to quantify PET and PET/CT data are also described. Finally, a list of *in silico* models that incorporate PET and/or PET/CT data is provided and reviewed.

1. Introduction

Anatomic imaging modalities, particularly X-ray computed tomography (CT) and magnetic resonance imaging (MRI), have long been the standard tools for the accurate localization of organs and lesions in radiation oncology. Today, they play a routine role in three-dimensional treatment planning. However, the effectiveness of structural imaging techniques in determining metabolic or functional tissue information is limited. Functional imaging has been demonstrated to be invaluable for the initial diagnosis and staging of cancer as well as the monitoring of therapy and the detection of cancer recurrence [1]. Metabolic changes in tissue commonly precede the structural changes that are detected via CT and MRI. Thus, imaging of metabolic changes may enable the detection of malignant disease at earlier stages of development [2]. In addition, the availability of functional information is advantageous for cases in which there is poor

contrast between normal and malignant tissue when using structural imaging. For example, for the initial staging of lymphomas, the metabolic information provided by positron emission tomography (PET) enables more accurate delineation of the extent of nodal disease as compared with CT and bone scans. Similarly and perhaps most notably, PET demonstrates superior local staging capabilities for head and neck cancers over both CT and MRI. FDG-PET alone has a plethora of indications for a wide variety of malignancies [3]. Consequently, functional imaging modalities such as PET are playing an increasingly important role in the management of malignant disease.

PET scanning has progressed into widespread clinical practice since its first commercialization in the late 1970s. For oncological PET studies, the most utilized and extensively researched radiotracer is ¹⁸F-fluorodeoxyglucose (FDG). FDG-PET has demonstrated superior accuracy over conventional imaging modalities in multiple scenarios across

both the diagnosis and the staging of cancer [3, 4]. In a variety of clinical settings, FDG-PET exhibits improved values of sensitivity, specificity, or both. Examples of clinical scenarios in which FDG-PET has demonstrated efficacy include the evaluation of mass lesions, the staging and restaging of cancer, the planning of radiotherapy treatments, the monitoring of therapy, and the detection of cancer recurrence [3]. However, the primary drawback of functional imaging is the lack of anatomic information that it provides. This necessitates its accompaniment with structural imaging for application in clinical oncology [1].

In order to take advantage of their inherent benefits, the combined use of both anatomic and physiologic imaging modalities is optimal. The accurate structure localization capabilities of CT complement the mapping of normal and abnormal tissue function performed by PET. Because of this, PET images are routinely read alongside CT images in order to both distinguish and localize metabolic irregularities. In the first instance, this has been achieved via the coregistration of separately acquired PET and CT images using fusion software, a technique which has especially proved to be effective for brain imaging. However, coregistration of images of other anatomical regions poses significant challenges [5]. Difficulties in the registration process primarily arise from varying patient positioning between the two image sets. Whilst such difficulties are minimal for brain scans, they may be significant in other anatomical regions wherein there may be substantial organ movement or deformation. In light of this, the development and subsequent commercialization of the PET/CT scanner in 2001 has generally addressed the issues affecting the coregistration of separately acquired PET and CT images [6].

The use of integrated PET/CT in oncologic imaging has since become a widespread field of research, particularly with the utilization of ^{18}F -FDG. This combined modality overcomes some of the drawbacks that are characteristic of standalone PET scanning, namely, the significant presence of noise in attenuation correction factors, the lengthy duration of scans, and the absence of anatomic markers [7]. While the vast majority of published research concerns standalone PET, PET/CT has begun to show great promise across a multitude of clinical settings [3]. Studies have shown significantly improved accuracy in the staging of nonsmall cell lung cancer with PET/CT over the separate performance of PET and CT [8–10]. Some centres perform a series of PET/CT scans on nonoperative head and neck cancer patients following either radiation therapy or chemotherapy due to its indispensable combined anatomical and functional information [3, 7, 11]. For patients with recurrent or metastasized thyroid cancer, the localization capabilities of ^{18}F -FDG-PET/CT can lead to improved diagnostic accuracy [12]. Finally, the incorporation of FDG-PET/CT data into the radiation treatment planning process has repeatedly shown to improve target delineation and enhance the therapeutic ratio via its increased cancer staging accuracy [13]. The ongoing clinical evaluation and further innovation of PET/CT, namely, via technological improvements and the establishment of new tracers, will continue to propel this technology into widespread use in oncology [3].

The significant interpatient variability in both tumour behaviour and normal tissue response to cancer therapy has prompted increasing demand for individualized treatment planning. Simulations of radiobiological processes in malignancies provide scope for the further optimization of individual treatment plans and to ultimately improve patient outcomes. The development of computer or *in silico* models of these radiobiological processes is particularly beneficial [14]. It is here in which PET and PET/CT, as noninvasive functional imaging modalities, can play a crucial role [15–17]. The aim of this work is to review the application and effectiveness of PET and PET/CT for the *in silico* modelling of tumours. In particular, it examines the various parameters that can be determined via PET and PET/CT imaging along with the assortment of radiotracers available for these purposes. The biophysical quantities used to quantify PET and PET/CT data, including SUV and compartmental models, are assessed. Finally, an overview of the existing *in silico* models that utilize PET or PET/CT data is provided.

2. Tumour Model Parameters Obtainable from PET Imaging

With the objective of optimal, individualized treatment planning, many biological characteristics of a given tumour can be considered for computer simulation. In the case of radiation therapy, the proliferative potential of a tumour and its radiosensitivity are of particular interest. Parameters which describe tumour cell proliferation and repopulation characteristics are useful for *in silico* modelling of tumour growth and treatment response. Similarly, since it is well established that tumour's oxygenation level contributes significantly to its radioresistance, modelling parameters that characterize tumour hypoxia and angiogenesis are also common. Increasingly, *in silico* models have expanded to incorporate additional contributing factors to tumour radiosensitivity, including intracellular tumour pH, gene expression, and cell-cycle simulation. The complexity of any given model dictates the number of characteristics simulated, as well as the accuracy with which each tumour characteristic is simulated. Simpler models may use averaged, macroscopic measures of a given tumour characteristic, while more complex models may simulate a tumour and its behaviour at the microscopic, molecular, and even atomic levels. Indeed, some of the most accurate, contemporary models are “multiscale”; they simulate tumour behaviour across multiple biological scales, reconciling the macroscopic and microscopic levels [18]. Details of the various parameters utilized for tumour modelling obtainable from PET and PET/CT data are provided below.

2.1. Cell Proliferation. There are many approaches to modelling cell proliferation but it is useful to separately consider modelling at the macroscopic and microscopic scales. At the macroscopic scale, tumours are commonly simulated using continuum models. Using this approach, gross tumour morphology and behaviour are modelled under various environmental conditions and typically governed

by a set of differential equations whose initial conditions serve as input parameters [18]. Input parameters include such quantities as cell density (both viable and necrotic), cell volume fractions, and gross tumour proliferation and metabolic rates [19]. Such parameters may be gathered from PET/CT data, where a corresponding radiotracer can be utilized [20]. Details of various radiotracers and the functional information they provide are given in Section 3.

In contrast to continuum tumour models, discrete tumour models developed at the microscopic scale simulate individual cell behaviour. Their input parameters correspondingly describe a set of biophysical rules applied to the modelled cells and the diversity of these rules varies across different models. Each cell is assigned an initial state and its status is subsequently tracked throughout the simulation. Consequently, discrete models directly simulate cell proliferation; a process which is mediated by input parameters such as proliferative potential, cell-cycle positions, and durations for different cell types, probability of cell division, cell loss rates, and maximum tumour radius or cell number [19]. Patient-specific parameters such as tumour radius and proliferating cells per voxel are directly obtainable from functional imaging data [15].

2.2. Hypoxia. The adverse effects of tumour hypoxia on patient outcomes following radiotherapy have been well established. Indeed, hypoxia is often attributed to poor tumour control probabilities in locally advanced head and neck cancers, for which low oxygenation levels are common [21]. Accordingly the simulation of oxygenation in tumours has been a prolific area of research in the tumour modelling community for more than 60 years [22]. The simulation of tumour hypoxia varies greatly across different models; the most complex models concurrently simulate oxygen diffusion, oxygen consumption by tissue, and the interdependence of oxygen with tumour proliferation and vasculature [23].

Oxygen information is generally modelled using an analytic approach. That is, sets of differential equations are used to describe oxygen diffusion and/or consumption rates both during tumour growth and in response to treatment. Even stochastic (discrete) tumour cell proliferation models that incorporate oxygen information typically employ a composite approach; oxygen and other substrate concentrations are generally governed by continuous fields. Since the oxygen distribution within a tumour is directly related to the extent and nature of its vasculature, many tumour hypoxia models incorporate blood vessel information into their simulations. The most sophisticated models simulate angiogenesis (see Section 2.3) and its effect on tumour hypoxia [16, 23, 24].

Simulated oxygen distributions are typically quantified using partial oxygen tension or pO_2 values. Thus, for the successful simulation of tumour hypoxia, realistic initial pO_2 conditions must be set. In order to categorize the oxygen status of tissue, binary approaches to oxygen modelling establish a defined threshold pO_2 value below which the region is considered to be hypoxic. More robust models establish a more detailed relationship between tumour growth

or treatment response and oxygen information and may incorporate both oxygen diffusion and oxygen consumption by tissue [23, 25]. Additional parameters of interest may be included for oxygen effects, such as reoxygenation probability distributions and hypoxic thresholds for which cell quiescence is initiated. Multiple studies have demonstrated the utility of PET for obtaining pO_2 distributions for use in patient-specific tumour models [16, 23, 26].

2.3. Angiogenesis. The extent and nature of tumour vasculature significantly influence tumour growth and oxygen status. Consequently, the simulation of angiogenesis serves as a useful complement to models of tumour cell proliferation and hypoxia. Likecell proliferation, models of tumour-induced angiogenesis may be either continuous or discrete in nature. More advanced models utilize both approaches for simulating the various mechanisms involved in angiogenesis, such as capillary sprout formation, endothelial cell migration, blood flow, and vessel adaptation [19].

Input parameters related to vessel branching generally include probabilities of random endothelial cell migration, chemotaxis with tumour angiogenesis factor concentration (especially vascular endothelial growth factor or VEGF), and haptotaxis with fibronectin gradients [18]. The utility of PET for the imaging of specific angiogenic markers, such as $\alpha_v\beta_3$ integrins and tumour expression of VEGF, has been demonstrated by multiple groups [28, 29]. To date, tumour models of angiogenesis have traditionally not incorporated angiogenesis-specific PET data. However, since cellular oxygenation and tumour vasculature are intimately related phenomena, hypoxia-specific PET data has been utilised in models of tumour vasculature [16, 23]. Specifically, the value of PET information for the conversion of oxygen maps into capillary density maps has been demonstrated. The potential of angiogenesis-specific PET-based imaging for input in modelling the temporal development of vasculature or angiogenesis is well understood and will develop with ongoing studies [16].

2.4. pH. Though the intracellular pH of solid tumours is maintained in a range similar to that of normal cells, the extracellular pH of solid tumours is commonly acidic. The increased glucose metabolism of solid tumours, assisted by characteristically poor perfusion, is the most probable cause of their low extracellular pH. This is because glucose catabolism results in net acid production and insufficient vasculature cannot remove excess acid from the extracellular environment [30].

Perhaps the most compelling value of including pH in tumour growth models arises from the acid-mediated tumour invasion hypothesis. This suggests that tumour cells develop phenotypic adaptations to the harmful effects of acidosis during carcinogenesis, traits that are not present in normal cells. Consequently, tumour cells are rendered relatively impervious to the decreased pH in the tumour microenvironment resulting from increased anaerobic glycolysis, which is otherwise toxic to normal tissue. Effectively the tumour provides for itself a selective growth advantage and a useful mechanism for invasion [31]. Investigation of

TABLE 1: PET Radiotracers whose data has been/the potential to be incorporated into *in silico* models.

PET radiotracer	Functional characteristic	Corresponding tumour model parameters	Use in <i>in silico</i> models?
FDG	Glucose metabolism	(i) Intracellular Volume Fraction (ICVF) (ii) Acid production rates*	Yes
FLT	DNA replication	Tumour cell proliferative rates (vector- or voxel-based)	Yes
FMISO	Hypoxia	(i) Partial oxygen tension (pO ₂) (ii) Relative hypoxic fraction (RH)	Yes
Cu-ATSM	Hypoxia	Partial oxygen tension (pO ₂)	Yes
pHLIP	Acidosis	Extracellular pH (pH _e)	Potential
Galacto-RGD	Angiogenesis	(i) $\alpha_v\beta_3$ expression rate	Potential
FDOPA	Malignancy	(ii) L-DOPA activity	Potential
FES	Malignancy	(iii) Oestrogen overexpression	Potential

*The specificity of FDG to glucose metabolism provides an indirect measure of acid production rates in tumour cells, since anaerobic glycolysis is net acid producing.

this phenomenon is particularly suited for *in silico* tumour growth modelling and the role played by acid gradients in triggering tumour invasion has been evaluated this way [31]. Excess H⁺ ion concentration may be simulated in a continuum model utilizing reaction-diffusion partial differential equations, where input parameters such as acid production rate, reabsorption rate, and H⁺ ion diffusion coefficients may be obtained from measurement [32].

As with angiogenesis, *in silico* models incorporating tumour pH have not utilized noninvasive PET data for input. Though PET has been used for the measurement of pH since the 1970s and was the first noninvasive *in vivo* pH meter, it has historically been both an inaccurate and imprecise measurement tool [30]. However, the development of novel radiotracers that selectively target acidic tumours will enable the incorporation of pH related PET data into *in silico* models of tumour growth [33].

3. Radiotracers Used for Tumour Modelling

PET and PET/CT are able to image an increasing variety of physiological phenomena. This versatility arises from the ability to select a radiotracer that specifically targets a particular mechanism. Additionally, the diversity of PET tracers continues to expand with ongoing innovations in radiopharmaceutical production. Today, radiotracers exist for the imaging of metabolism, proliferation, perfusion, drug/receptor interactions, and gene expression. Despite this variety, the extent of PET data incorporated into *in silico* tumour models has so far been limited to radiotracers specific to glucose metabolism, cell proliferation, and hypoxia. There is significant potential for the use of alternative radiotracers to obtain additional functional information for *in silico* models using PET. A list of radiotracers whose information has been directly incorporated into *in silico* models as well as those that show significant promise for such applications is provided in Table 1.

3.1. *FDG*. ¹⁸F-2-Fluoro-2-deoxy-glucose or FDG is by far the most commonly used and extensively researched PET radiotracer. Today, FDG-PET plays an important role in

oncology. It has been recommended for use as an imaging tool additional to traditional radiological modalities in the appropriate clinical setting. In particular, it has demonstrated efficacy in the diagnosis, staging, unknown primary discovery, and the detection of cancer recurrence [1].

Increased glucose consumption is a typical characteristic of most cancers. In hypoxic regions, the Pasteur effect results in the upregulation of anaerobic glycolysis and the GLUT 1 glucose transporter in tumour cells. However, even if oxygen is plentiful, cancers undergo accelerated glycolysis. This observation, called the Warburg effect, is widely attributed to mutations in oncogenes and tumour suppressor genes [34]. Since FDG is a glucose analogue, it is a particularly suitable radiotracer to measure the increased glucose utilization typical of cancers. Along with increased glucose consumption, the upregulation of appropriate enzymatic activity further amplifies FDG uptake in tumour cells.

The primary drawback of FDG-PET for oncologic imaging is that FDG uptake is not specific to cancer. That is, FDG-PET exhibits a poor level of specificity for certain applications. FDG uptake may be intense in benign diseases as well as in areas of infectious disease and inflammatory tissue. That is, there are many potential causes of false-positive PET signals in oncologic imaging [1, 35, 36]. Conversely, some malignant diseases do not exhibit high glycolytic activity. Bronchioloalveolar carcinoma and carcinoid tumours are examples of cancers for which false-negative signals may occur for standalone FDG-PET imaging [35]. Combining FDG-PET with other imaging modalities has served to mediate this drawback somewhat; FDG-PET/CT has demonstrated superior performance than standalone FDG-PET in common cancers [37]. Additionally, the emergence of novel radiotracers that target biochemical processes that are more specific to cancer promises to overcome the relative nonspecificity of FDG-PET in oncologic imaging.

Commensurate with the predominance of FDG as the PET radiotracer of choice, metabolic information provided by FDG-PET is often utilized in *in silico* models of both tumour growth and treatment response [16, 20]. The specific information employed from FDG-PET varies across such models. Images may be used solely to identify existing

cancerous tissue, particularly in simulations for the prediction of tumour response to therapy [16]. Alternatively, glucose metabolism data from FDG-PET can be quantitatively used to simulate metabolic processes in predictive models of tumour growth [20].

3.2. FLT. PET radiotracers specific to cell proliferation are an effective alternative to those specific to glucose metabolism, such as FDG. Of these tracers, ^{18}F -3-fluoro-3-deoxy-thymidine (FLT) is perhaps the most researched and the most utilized. FLT-PET is typically a less sensitive imaging modality than FDG-PET: the difference in FLT uptake between normal and malignant tissues is usually less pronounced than that for FDG [38]. However, FLT uptake correlates very well with Ki-67, an index of cell proliferation. Consequently, FLT-PET is useful for aiding in the grading of tumours. The combined FLT-PET/CT modality has demonstrated efficacy for the early prediction of treatment response [39–41] as well as the assessment of cancer aggressiveness [42]. The uptake of FLT in infectious or inflammatory tissue is less than that of FDG and FLT has lower background activity in the brain and thorax [43, 44]. Consequently, the specificity of FLT-PET/CT exceeds that of FDG-PET/CT in certain imaging applications [44].

The magnitude of FLT that is trapped in a tumour cell is proportional to the amount of DNA/RNA synthesis undertaken by the cell. Since the growth of malignant tissue is intricately related to DNA replication, the degree of FLT uptake is strongly correlated with proliferation rate. Accordingly, FLT-PET data is particularly useful for patient-specific tumour modelling, where proliferative rates are often of paramount interest. A group led by Benjamin Titz at the University of Wisconsin has correspondingly acquired cell proliferation information from FLT-PET data for *in silico* models of tumour growth and treatment response [15, 16].

3.3. FMISO. In an effort to develop accurate, noninvasive measurement techniques of tumour hypoxia, a number of PET radiotracers have been produced which irreversibly bind to cells in poorly oxygenated conditions. Of these, ^{18}F -fluoromisonidazole (FMISO) is the most extensively studied and clinically validated. FMISO uptake is inversely proportional to O_2 level and perfusion does not restrict its delivery to malignant tissue. Several studies have demonstrated FMISO-PET to be a viable prognostic indicator of tumour response to treatment [45].

FMISO-PET has not been universally adopted into routine clinical application because of a number of limitations inherent in the radiotracer. Since it relies on passive transport mechanisms, its uptake is relatively slow in hypoxic tumours, usually requiring 2–4 hours to be selectively retained in the target following injection [46]. FMISO-PET imaging also exhibits relatively low tumour-to-background ratios, since its binding to malignant, hypoxic cells is highly nonspecific. Finally, considerable levels of unwanted, radioactive metabolite products result from the nonoxygen dependent metabolism of FMISO [45]. Improvements in the quantification of hypoxia by modelling FMISO-PET dynamics, as

opposed to using the standardized uptake value (SUV) in a binary manner, may aid in overcoming contrast limitations. Several studies have demonstrated reasonable success in the simulation of tracer transport and its application to tumour models (see Section 5) [25–27].

3.4. Cu-ATSM. Alternative hypoxia-specific PET radiotracers have been developed in order to overcome the various limitations of FMISO. Several other nitroimidazole compounds have been developed for this purpose [47]. In 1997, an alternative hypoxia PET tracer was proposed that does not suffer from the undesirable radioactive residues of nitroimidazoles. This tracer is Cu(II)-diacetyl-bis(N^4 -methylthiosemicarbazone) or Cu-ATSM [48]. Cu-ATSM has evolved to become one of the most promising PET agents for hypoxia imaging. It has demonstrably high hypoxic tissue selectivity [45]. It is able to rapidly identify hypoxic tissue with high tumour-to-background ratios, due to a combination of small molecular weight, high cell membrane permeability, rapid blood clearance, and prompt retention in hypoxic tissues [45].

The effectiveness of Cu-ATSM for providing clinically relevant tumour oxygenation information has been confirmed in multiple studies and its predictive value of tumour behaviour and treatment response has been demonstrated [49–51]. Perhaps unsurprisingly, it is a preferred radiotracer for the determination of oxygenation information using PET for incorporation into *in silico* tumour models [15, 16, 23]. For example, Titz and Jeraj chose a sigmoidal relationship between the SUV of Cu-ATSM and local tissue oxygenation [15], following the findings of Lewis et al. [52]. Using pretreatment Cu-ATSM-PET spatial maps of tumour oxygenation, it was demonstrated that lower oxygen levels resulted in reduced treatment efficacy. However, the group did note that further investigation into the quantitative relationship between partial oxygen tension and Cu-ATSM uptake is warranted.

3.5. Other Radiotracers. Although *in silico* models are yet to incorporate PET or PET/CT information beyond glucose metabolism, cell proliferation, and tumour oxygenation, there is scope for the use of tracers that image additional processes. Tumour acidosis arising from amplified glycolysis is a common feature of cancers and is a likely trigger of invasion into surrounding tissue [53]. Consequently, several mathematical models, inclusive of tumour acidity, have been developed to study the glycolytic phenotype and the tumour-host interface [31, 54]. There is suggestive potential of PET and particularly PET/CT for directly obtaining parameters of interest for such models, including glucose metabolic rate and acid production rates. One promising, novel PET tracer that specifically targets acidosis is pH low insertion peptide (pHLIP) [33]. pHLIP binds to acidic cell membranes and has demonstrated ability to target areas of hypoxia and carbonic anhydrase IX (CAIX) overexpression, an acid-extruding protein [55].

As discussed in Section 2, the simulation of angiogenesis is of significant interest for *in silico* tumour modelling.

Though parameters related to angiogenesis can be indirectly obtained using hypoxia-specific PET-imaging, alternative markers of angiogenesis can instead be targeted. For example, vascular integrins are targeted by PET radiotracers containing the tripeptide sequence arginine-glycine-aspartic acid (RGD) [28]. In particular, the $\alpha_v\beta_3$ integrin is a receptor related to cell adhesion and involved in tumour-induced angiogenesis that can be imaged using radiotracers such as ^{18}F -Galacto-RGD [29].

In models that simulate specific tumour types, PET information from alternative tracers might be useful. For example, neuroendocrine tumours are typically characterised by an increased L-DOPA decarboxylase activity [56]. The imaging of advanced neuroendocrine tumours has been validated with PET using ^{18}F -dihydroxyphenylalanine (FDOPA) [57] and may be of value in the modelling of these tumours. Similar arguments may be made for the simulation of breast cancers and the imaging of oestrogen receptor expression using ^{18}F labelled oestrogens such as ^{18}F -fluoroestradiol (FES) [58].

4. Biophysical Parameters Used in PET and PET/CT

The integration of reliable imaging-based information into *in silico* models of tumour growth and treatment response greatly relies on the accurate and precise quantification of imaging data. This is especially relevant for PET and PET/CT, for which radiotracer uptake is dependent on a host of factors. SUV is the most extensively used parameter clinically for the analysis of PET tracers, but its high degree of sensitivity to multiple variables can render the comparison of SUVs taken at different times or between different centres to be extremely difficult [59].

Details of the biophysical parameters used to quantify PET and PET/CT data are provided below. Their applications and limitations are discussed and compared, as well as the various methods that have been developed to overcome the potential pitfalls of a given measure. The present use of PET and PET/CT quantification measures in *in silico* models of tumour growth and treatment response is also discussed.

4.1. SUV. The standardized uptake value is the quintessential parameter employed to analyse and quantify PET radiotracer data. It is defined as follows:

$$\text{SUV} = \frac{\text{radiotracer concentration in ROI}}{\text{total injected activity}/N} \text{ g/mL}, \quad (1)$$

where the concentration is as measured with PET in kBq/mL, ROI is the region or volume elements of interest, and N is a factor normalizing for body weight, body surface area, or lean body mass. The overall denominator has units kBq/g. The radiotracer is commonly computed by scanning the patient for a 5–15-minute interval after a predetermined period (e.g., 1 hour) after radiotracer injection.

In general, SUV depends on the time between injection and scanning as well as multiple image acquisition settings

such as the reconstruction algorithm and scatter and attenuation corrections [59]. Its comparative value is hampered by methodology differences, such as choice of normalization factor and choice of *max*, *mean*, *peak*, or *total* SUV [60]. SUV may also be confounded by biological mechanisms, such as variations in plasma clearance before and after treatment and plasma glucose concentration (in the case of FDG) [59].

Despite its limitations, SUV poses advantages over alternative quantification techniques such as compartmental methods (see Section 4.2). It is the only method of PET quantitative analysis that can be realistically employed for routine clinical use, due to its sheer simplicity and the efficiency of the associated scan protocols. In addition, the effectiveness of SUV for the assessment of cancer therapy response by comparing values for scans taken before and after treatment has been extensively validated. This is particularly true for FDG-PET, whose efficacy has been confirmed for multiple cancer types [59]. Accordingly, in spite of its large variation in some situations, the use of SUV is common for the acquisition of metabolic information, proliferation rates, and pO_2 values for use in *in silico* tumour models [16, 20, 23].

4.2. Compartmental Models. Compartmental or kinetic modelling (CM) is the “gold standard” of quantification methods for PET data [59]. In CM, the exchange of the PET radiotracer between a number of physiological entities (called compartments) is simulated. These compartments are homogeneous in nature and the tracer transport and binding rates between them is modelled by a set of first-order differential equations [61]. The set of equations are solved numerically to obtain the rate constants, kinetic parameters analogous to those outlines in Section 2, such as glucose metabolic rates or blood flow [59].

Despite its accuracy and relative independence of confounding effects as compared to SUV, CM has the disadvantage of requiring a complex, time-intensive acquisition protocol. Techniques with which the requisite scan protocol complexity of CM can be overcome are an ongoing field of research [62, 63]. In the case of radiotracers such as FDG for which the use of SUV has been strongly validated (via comparison with CM, in some cases), the added benefit of employing CM techniques for PET analysis is likely to be insubstantial [59].

However, in the case of FMISO-PET imaging of hypoxia, the use of CM is warranted. Whilst FMISO can be used to identify and image tumour hypoxia, it typically exhibits poor tumour-to-background ratios using the standard SUV measure, generating highly variable results [25, 27]. Compartmental modelling of hypoxia imaging for dynamic FMISO-PET data has shown great success in ameliorating this problem, with particularly promising contributions from Thorwarth et al. [25] and Wang et al. [27].

4.3. Hounsfield Units. The process of positron emission tomography is based on the coincident detection of colinear, 511 keV photons originating from an annihilation event. This measurement may be affected by an interaction between one or both of the photons and the attenuator prior to reaching

the detectors. A colinear coincident event is consequently not detected and may instead register as scatter coincidence or no coincidence. To account for this signal loss, attenuation corrections are performed during PET image reconstruction in an effort to salvage the true radiotracer distribution. Until the development of PET/CT attenuation correction in PET was performed using a transmission scan taken immediately prior to the imaging scan, effectively doubling the total scan time. In modern PET/CT scanners, CT-based attenuation correction of PET images can be performed using the immediately available CT images. 511 keV linear attenuation values are obtained from the Hounsfield unit (HU) data provided by the CT using an appropriate transformation scheme [64], usually a bilinear relationship.

CT scanners convert attenuation coefficient distributions $\mu(x, y, z)$ into HU for display. Since attenuation is directly proportional to attenuator density, the HU of a particular voxel may be interpreted as the density of the object within that voxel relative to that of water. Typical scans consist of image noise within the range of 10–50 HU, corresponding to a relative error of 1–5% [65]. Consequently, CT is a powerful imager of tumour density. For oncologic scenarios in which lesions and background tissues are characterized by similar HU values, assessment with CT is facilitated by the use of positive and negative contrast agents. Contrast enhancement in PET/CT has been reported to improve lesion detection, characterization, and localization in some clinical settings [66–68].

Positive contrast agents within PET/CT may cause overestimation of PET attenuation with contrast-enhanced CT based attenuation corrections. This can lead to artifacts of apparently increased tracer uptake in regions of high contrast concentration within the PET image. However, such artifacts can often be attributed to an underlying vessel and hence do not cause problems with image interpretation [65]. Furthermore, several research studies have confirmed the clinical insignificance of this effect, since the typical SUV measure is negligibly affected by contrast [69, 70].

5. Review of Computational and Mathematical Models of Tumour Growth and Prediction to Treatment Response Based on PET Imaging Data

With the advances in technology, the current imaging modalities offer a great variety of biological, biophysical, and clinical parameters to be further studied and implemented into complex tumour models. Computational modelling is an ever-increasing area of research in tumour biology and therapy. Depending on their design (i.e., continuum or discrete) models offer various levels of understanding of biological, biochemical, and biophysical processes occurring in tumours before and during treatment. Models are versatile in terms of input parameters, equations used, phenomena simulated, and end points. While never perfectly illustrating the biological reality, models are valuable complements to kinetic analysis of tumour growth and development, treatment outcome

prediction, patient selection, and important decision-making towards personalized medicine.

There are a large number of computational and mathematical tumour models that incorporate functional imaging data in the scientific literature. This is particularly true for PET and PET/CT. A detailed list is provided in Table 2, which includes models of tumour growth, tumour characteristics, and response to treatment. The aims of the models, the corresponding imaging techniques used and physiological parameters imaged, and the relevant group's findings are given.

Tumour growth models are an important initial step when modelling treatment response. Using dual-phase CT and FDG-PET imaging modalities, Liu et al. have developed a tumour growth model for pancreatic cancers [20, 71]. They have introduced the intracellular volume fraction (ICVF) as biomarker for the estimation and evaluation of the model's parameters, based on longitudinal dual-phase CT images measured on pre- and postcontrast images. SUV was used as a semiquantitative measure of tumour metabolism (metabolic rate), which was further related to tumour proliferation rate. The model was validated by comparing the virtual tumour with a real pancreatic tumour, in terms of average ICVF difference of tumour surface, relative tumour volume difference, and average surface distance between the predicted tumour surface and the CT-segmented (reference) tumour surface [20].

Perhaps the vast majority of the models address the challenge of tumour hypoxia and neovascularization [15, 16, 23, 27]. The approach used in the models varies among research groups. Given that compartmental models are great tools in kinetic modelling of perfusion, diffusion, and pharmacokinetics of various tracers, they were chosen by some groups to quantitatively estimate the levels of hypoxia in head and neck tumours and also to assess the hypoxic distribution within the tumour [25, 27]. Considering the controversies around SUV and its correlation with the partial oxygen tension (pO_2), Thorwarth et al. came to a practical conclusion, whereby compartmental kinetic models are more reliable for hypoxia assessment than early static SUV measurements, due to the low uptake of FMISO by severely hypoxic cells.

Experimental probability density functions were employed by other groups to simulate the direction and spatial arrangement of microvascular tumour density, using patient-specific PET imaging information [23]. The discovered correlation between microvessel density and tumour oxygenation levels (i.e., pO_2) suggests that patient-based simulation can contribute towards individualized patient planning and treatment.

Hybrid models (or multiscale models) are often used for complex assessment of tumour growth and behaviour under therapy, due to their versatility and ability to integrate mathematical/computational modelling with experimental data on different physical scales. The hybrid model developed by Titz and Jeraj is an example of this [15]. Depending on the input parameters chosen in terms of relevance and reliability, such hybrid models can predict, with high accuracy, tumour response to various treatments. As illustrated in Section 3, functional imaging and particularly PET imaging

TABLE 2: Models of tumour growth and prediction to treatment response based on PET imaging data.

Aim of the model [references]	Imaging technique used	Model parameters	Results/observations
Models of tumour growth			
Spatial-temporal characterization of pancreatic tumour growth and progression [20]	Dual-phase CT and FDG-PET	Intracellular Volume Fraction (ICVF) which reflects tumour cell invasion and SUV used for determination of cell metabolic rate, growth rate, cell motion: diffusion and advection (for mass effect).	The model was successfully validated against a real tumour using average ICVF difference of tumour surface, relative tumour volume difference & average surface distance between predicted and segmented tumour surface.
Models of tumour characteristics			
Evaluation of tumour hypoxia in head and neck tumours [25]	Dynamic FMISO-PET	Tracer transport and diffusion model; voxel-based data analysis used to decompose time-activity curves into components for perfusion, diffusion and hypoxia-induced retention.	Quantification of hypoxia; hypoxic regions are spatially separated from blood vessels; tracer uptake occurs in viable hypoxic cells-only. The kinetic model is more accurate than static SUV values.
Simulation of tumour oxygenation [26]	Dynamic FMISO-PET	Model input parameters for steady-state O ₂ distribution: 2D vascular map, oxygen tension and rate of oxygen consumption. Binding rates of FMISO estimated and spatial-temporal O ₂ distribution found. Probability density function was used to model tumour vasculature to identify hypoxic sub-regions.	Hypoxic sub-region distribution and shape resulting from the simulation agree with real imaging data. It was shown that the extent of vasculature is of greater importance than the level of tissue oxygen supply. The model allows for quantitative analysis of tumour parameters when physiological changes occur in tumour microenvironment.
Estimation of tumour hypoxia in head and neck tumours [27]	Dynamic FMISO-PET	Region of interest and arterial blood are identified via PET. Values of kinetic parameters (for oxic, hypoxic and necrotic areas) are taken from PET-scanned patient data.	Voxel-based compartmental analysis is feasible to quantify tumour hypoxia and more reliable than static PET-SUV measurements.
Simulation of tumour vasculature [23]	Cu-ATSM PET and contrast CT	Capillaries were simulated using probability density functions (micro-vessel density) and patient imaging data. Capillary diameter was modelled in conjunction with voxel size; a relationship between vessel density and pO ₂ was employed.	Simulation of homogenous and heterogeneous oxygen and vascular distribution. The model was tested on mouse tumour: the simulated vasculature and the Cu-ATSM PET hypoxia map represent the image-based hypoxia distribution. The model can be used for anti-angiogenic treatment simulation.
Models of treatment response			
Tumour growth and response model with hypoxia effects [15]	¹⁸ F-FLT (for proliferation) & Cu-ATSM PET (for hypoxia) and CT	CT used for tumour anatomy. Behaviour of tumour voxels modelled upon PET data. FLT uptake was used as proliferation index. A sigmoid relationship was considered between Cu-ATSM SUV and pO ₂ . The Linear Quadratic model was used for cell survival.	The model accurately reproduced tumour behaviour for different oxygen distribution patterns. Treatment simulations resulted in poor control for hypoxic tumours: heterogeneous oxygen distribution resulted in heterogeneous tumour response (i.e. higher survival among hypoxic cells).
Evaluation of tumour response to anti-angiogenic therapy [16]	¹⁸ F-FDG (for metabolic activity) ¹⁸ F-FLT (for proliferation) & Cu-ATSM PET (for hypoxia) and CT	Model based on previous work [15] with an added vascular component. Microvessel density was used as model parameter in direct relationship with the vascular growth fraction. Probability density functions were used to sample capillary properties and geometry.	The maximum vascular growth fraction was found to be the most sensitive model parameter. The dosage of the anti-angiogenic agent bevacizumab can be adjusted to improve oxygenation. The model was validated on imaging data of a phase I trial with bevacizumab on head and neck cancer patients.

employing tumour-specific radiotracers play an important role in fulfilling this task. Therefore, information regarding tumour kinetics and proliferation can be obtained from proliferation-specific agents (such as FLT) while oxygen distribution data is gained from hypoxia-specific radiotracers (such as FMISO or Cu-ATSM). Additionally, with ongoing radiotracer development and evaluation, there is scope for obtaining additional tumour characteristics, such as acidosis using pHLIP and gene expression using protein-specific agents such as Galacto-RGD, FDOPA, and FES.

To further prove the usefulness of complex multiscale models, the same group has simulated the effect of bevacizumab, an anti-VEGF agent, which is administered for targeting endothelial cell population in tumours [16]. Tumour hypoxia and proliferation data were gathered from PET images taken before and after the antiangiogenic treatment. Simulated hypoxia levels were compared with mean SUV values and changes in mean SUV after the administration of bevacizumab for various levels of hypoxia, proliferation, and VEGF expression were analysed. The findings were implemented on imaging data of a phase I clinical trial that involved eight head and neck cancer patients, showing the potential of such models to optimise treatment outcome.

6. Conclusion

The incorporation of patient-specific data into multiscale models is necessary for individualized, predictive simulation. This is an essential component of predictive oncology. Image-based information can be transformed into input parameters and incorporated into either probabilistic or deterministic equations governing their relationships and interdependences. Using these tools, countless hypotheses can then be generated and scenarios of “what if” can be simulated and solved. Models usually have the benefit of independence from the manner in which input parameters are obtained. This allows for the constant refinement of parameters with future innovations in measurement techniques, particularly in PET and PET/CT. Additionally, most models can be readily adapted to include new parameters in order to better resemble the real tumour environment. The widespread, continuing research into *in silico* model development and refinement permits the simulation of cancer with ever-increasing accuracy, with the goal of optimally individualizing cancer management and improving overall patient outcome.

Conflict of Interests

The authors declare that there is no conflict of interests regarding the publication of this paper.

Acknowledgment

L. G. Marcu would like to acknowledge the support offered by a Grant of the Ministry of National Education, CNCS-UEFISCDI, Project no. PN-II-ID-PCE-2012-4-0067.

References

- [1] J. W. Fletcher, B. Djulbegovic, H. P. Soares et al., “Recommendations on the use of 18F-FDG PET in oncology,” *The Journal of Nuclear Medicine*, vol. 49, no. 3, pp. 480–508, 2008.
- [2] O. Israel and A. Kuten, “Early detection of cancer recurrence: ¹⁸F-FDG PET/CT can make a difference in diagnosis and patient care,” *The Journal of Nuclear Medicine*, vol. 48, no. 1, pp. 28S–35S, 2007.
- [3] D. Papathanassiou, C. Bruna-Muraille, J.-C. Liehn, T. D. Nguyen, and H. Curé, “Positron emission tomography in oncology: present and future of PET and PET/CT,” *Critical Reviews in Oncology/Hematology*, vol. 72, no. 3, pp. 239–254, 2009.
- [4] S. S. Gambhir, J. Czernin, J. Schwimmer, D. H. S. Silverman, R. E. Coleman, and M. E. Phelps, “A tabulated summary of the FDG PET literature,” *The Journal of Nuclear Medicine*, vol. 42, no. 5, pp. 1S–93S, 2001.
- [5] T. M. Blodgett, C. C. Meltzer, and D. W. Townsend, “PET/CT: form and function,” *Radiology*, vol. 242, no. 2, pp. 360–385, 2007.
- [6] T. Beyer, D. W. Townsend, T. Brun et al., “A combined PET/CT scanner for clinical oncology,” *The Journal of Nuclear Medicine*, vol. 41, no. 8, pp. 1369–1379, 2000.
- [7] T. Ishikita, N. Oriuchi, T. Higuchi et al., “Additional value of integrated PET/CT over PET alone in the initial staging and follow up of head and neck malignancy,” *Annals of Nuclear Medicine*, vol. 24, no. 2, pp. 77–82, 2010.
- [8] R. J. Cerfolio, B. Ojha, A. S. Bryant, V. Raghuvver, J. M. Mountz, and A. A. Bartolucci, “The accuracy of integrated PET-CT compared with dedicated PET alone for the staging of patients with nonsmall cell lung cancer,” *Annals of Thoracic Surgery*, vol. 78, no. 3, pp. 1017–1023, 2004.
- [9] G. Antoch, J. Stattaus, A. T. Nemat et al., “Non-small cell lung cancer: dual-modality PET/CT in preoperative staging,” *Radiology*, vol. 229, no. 2, pp. 526–533, 2003.
- [10] W. D. Wever, S. Ceysens, L. Mortelmans et al., “Additional value of PET-CT in the staging of lung cancer: Comparison with CT alone, PET alone and visual correlation of PET and CT,” *European Radiology*, vol. 17, no. 1, pp. 23–32, 2007.
- [11] G. W. Goerres, G. K. von Schulthess, and H. C. Steinert, “Why most PET of lung and head-and-neck cancer will be PET/CT,” *The Journal of Nuclear Medicine*, vol. 45, no. 1, pp. 66S–71S, 2004.
- [12] A. Shamma, B. Degirmenci, J. M. Mountz et al., “¹⁸F-FDG PET/CT in patients with suspected recurrent or metastatic well-differentiated thyroid cancer,” *The Journal of Nuclear Medicine*, vol. 48, no. 2, pp. 221–226, 2007.
- [13] M. MacManus, U. Nestle, K. E. Rosenzweig et al., “Use of PET and PET/CT for Radiation Therapy Planning: IAEA expert report 2006–2007,” *Radiotherapy and Oncology*, vol. 91, no. 1, pp. 85–94, 2009.
- [14] P. Tracqui, “Biophysical models of tumour growth,” *Reports on Progress in Physics*, vol. 72, no. 5, Article ID 056701, 2009.
- [15] B. Titz and R. Jeraj, “An imaging-based tumour growth and treatment response model: investigating the effect of tumour oxygenation on radiation therapy response,” *Physics in Medicine and Biology*, vol. 53, no. 17, pp. 4471–4488, 2008.
- [16] B. Titz, K. R. Kozak, and R. Jeraj, “Computational modelling of anti-angiogenic therapies based on multiparametric molecular imaging data,” *Physics in Medicine and Biology*, vol. 57, no. 19, pp. 6079–6101, 2012.
- [17] S. Sanga, H. B. Frieboes, X. Zheng, R. Gatenby, E. L. Bearer, and V. Cristini, “Predictive oncology: a review of multidisciplinary,

- multiscale in silico modeling linking phenotype, morphology and growth,” *NeuroImage*, vol. 37, pp. S120–S134, 2007.
- [18] T. S. Deisboeck, Z. Wang, P. MacKlin, and V. Cristini, “Multi-scale cancer modeling,” *Annual Review of Biomedical Engineering*, vol. 13, pp. 127–155, 2011.
- [19] J. S. Lowengrub, H. B. Frieboes, F. Jin et al., “Nonlinear modelling of cancer: bridging the gap between cells and tumours,” *Nonlinearity*, vol. 23, no. 1, pp. R1–R9, 2010.
- [20] Y. Liu, S. M. Sadowski, A. B. Weisbrod, E. Kebebew, R. M. Summers, and J. Yao, “Patient specific tumor growth prediction using multimodal images,” *Medical Image Analysis*, vol. 18, no. 3, pp. 555–566, 2014.
- [21] D. M. Brizel, G. S. Sibley, L. R. Prosnitz, R. L. Scher, and M. W. Dewhirst, “Tumor hypoxia adversely affects the prognosis of carcinoma of the head and neck,” *International Journal of Radiation Oncology, Biology, Physics*, vol. 38, no. 2, pp. 285–289, 1997.
- [22] A. L. Harris, “Hypoxia—a key regulatory factor in tumour growth,” *Nature Reviews Cancer*, vol. 2, no. 1, pp. 38–47, 2002.
- [23] V. Adhikarla and R. Jeraj, “An imaging-based stochastic model for simulation of tumour vasculature,” *Physics in Medicine and Biology*, vol. 57, no. 19, pp. 6103–6124, 2012.
- [24] W. Tuckwell, E. Bezak, E. Yeoh, and L. Marcu, “Efficient Monte Carlo modelling of individual tumour cell propagation for hypoxic head and neck cancer,” *Physics in Medicine and Biology*, vol. 53, no. 17, pp. 4489–4507, 2008.
- [25] D. Thorwarth, S. M. Eschmann, F. Paulsen, and M. Alber, “A kinetic model for dynamic ^{18}F -Fmiso PET data to analyse tumour hypoxia,” *Physics in Medicine and Biology*, vol. 50, no. 10, pp. 2209–2224, 2005.
- [26] C. J. Kelly and M. Brady, “A model to simulate tumour oxygenation and dynamic [18F]-Fmiso PET data,” *Physics in Medicine and Biology*, vol. 51, pp. 5859–5873, 2006.
- [27] W. Wang, J.-C. Georgi, S. A. Nehmeh et al., “Evaluation of a compartmental model for estimating tumor hypoxia via FMISO dynamic PET imaging,” *Physics in Medicine and Biology*, vol. 54, no. 10, pp. 3083–3099, 2009.
- [28] R. Haubner, H. J. Wester, W. A. Weber et al., “Noninvasive imaging of $\alpha_v\beta_3$ integrin expression using ^{18}F -labeled RGD-containing glycopeptide and positron emission tomography,” *Cancer Research*, vol. 61, no. 5, pp. 1781–1785, 2001.
- [29] A. J. Beer, R. Haubner, M. Sarbia et al., “Positron emission tomography using [^{18}F]Galacto-RGD identifies the level of integrin $\alpha_v\beta_3$ expression in man,” *Clinical Cancer Research*, vol. 12, no. 13, pp. 3942–3949, 2006.
- [30] X. Zhang, Y. Lin, and R. J. Gillies, “Tumor pH and its measurement,” *Journal of Nuclear Medicine*, vol. 51, no. 8, pp. 1167–1170, 2010.
- [31] R. A. Gatenby, E. T. Gawlinski, A. F. Gmitro, B. Kaylor, and R. J. Gillies, “Acid-mediated tumor invasion: a multidisciplinary study,” *Cancer Research*, vol. 66, no. 10, pp. 5216–5223, 2006.
- [32] R. A. Gatenby and E. T. Gawlinski, “A reaction-diffusion model of cancer invasion,” *Cancer Research*, vol. 56, no. 24, pp. 5745–5753, 1996.
- [33] A. L. Vavere, G. B. Biddlecombe, W. M. Spees et al., “A novel technology for the imaging of acidic prostate tumors by positron emission tomography,” *Cancer Research*, vol. 69, no. 10, pp. 4510–4516, 2009.
- [34] D. Grandér, “How do mutated oncogenes and tumor suppressor genes cause cancer?” *Medical Oncology*, vol. 15, no. 1, pp. 20–26, 1998.
- [35] J. M. Chang, H. J. Lee, J. M. Goo et al., “False positive and false negative FDG-PET scans in various thoracic diseases,” *Korean Journal of Radiology*, vol. 7, no. 1, pp. 57–69, 2006.
- [36] A. D. Culverwell, A. F. Scarsbrook, and F. U. Chowdhury, “False-positive uptake on 2- ^{18}F -fluoro-2-deoxy-D-glucose (FDG) positron-emission tomography/computed tomography (PET/CT) in oncological imaging,” *Clinical Radiology*, vol. 66, no. 4, pp. 366–382, 2011.
- [37] D. Delbeke, H. Schöder, W. H. Martin, and R. L. Wahl, “Hybrid imaging (SPECT/CT and PET/CT): improving therapeutic decisions,” *Seminars in Nuclear Medicine*, vol. 39, no. 5, pp. 308–340, 2009.
- [38] A. K. Buck, G. Halter, H. Schirrmeister et al., “Imaging proliferation in lung tumors with PET: 18F-FLT versus 18F-FDG,” *The Journal of Nuclear Medicine*, vol. 44, no. 9, pp. 1426–1431, 2003.
- [39] W. Chen, S. Delaloye, D. H. S. Silverman et al., “Predicting treatment response of malignant gliomas to bevacizumab and irinotecan by imaging proliferation with [18F] fluorothymidine positron emission tomography: a pilot study,” *Journal of Clinical Oncology*, vol. 25, no. 30, pp. 4714–4721, 2007.
- [40] B. S. Pio, C. K. Park, R. Pietras et al., “Usefulness of 3'-[F-18]fluoro-3'-deoxythymidine with positron emission tomography in predicting breast cancer response to therapy,” *Molecular Imaging and Biology*, vol. 8, no. 1, pp. 36–42, 2006.
- [41] H. Barthel, M. C. Cleij, D. R. Collingridge et al., “3'-Deoxy-3'-[^{18}F]fluorothymidine as a new marker for monitoring tumor response to antiproliferative therapy *in vivo* with positron emission tomography,” *Cancer Research*, vol. 63, no. 13, pp. 3791–3798, 2003.
- [42] J. S. Rasey, J. R. Grierson, L. W. Wiens, P. D. Kolb, and J. L. Schwartz, “Validation of FLT uptake as a measure of thymidine kinase-1 activity in A549 carcinoma cells,” *The Journal of Nuclear Medicine*, vol. 43, no. 9, pp. 1210–1217, 2002.
- [43] W. Chen, T. Cloughesy, N. Kamdar et al., “Imaging proliferation in brain tumors with 18F-FLT PET: comparison with 18F-FDG,” *Journal of Nuclear Medicine*, vol. 46, no. 6, pp. 945–952, 2005.
- [44] A. F. Shields, “PET imaging with 18F-FLT and thymidine analogs: promise and pitfalls,” *The Journal of Nuclear Medicine*, vol. 44, no. 9, pp. 1432–1434, 2003.
- [45] G. Mees, R. Dierckx, C. Vangestel, and C. van de Wiele, “Molecular imaging of hypoxia with radiolabelled agents,” *European Journal of Nuclear Medicine and Molecular Imaging*, vol. 36, no. 10, pp. 1674–1686, 2009.
- [46] W. J. Koh, J. S. Rasey, M. L. Evans et al., “Imaging of hypoxia in human tumors with [F-18]fluoromisonidazole,” *International Journal of Radiation Oncology, Biology, Physics*, vol. 22, no. 1, pp. 199–212, 1992.
- [47] S. T. Lee and A. M. Scott, “Hypoxia positron emission tomography imaging with 18F-fluoromisonidazole,” *Seminars in Nuclear Medicine*, vol. 37, no. 6, pp. 451–461, 2007.
- [48] Y. Fujibayashi, H. Taniuchi, Y. Yonekura, H. Ohtani, J. Konishi, and A. Yokoyama, “Copper-62-ATSM: a new hypoxia imaging agent with high membrane permeability and low redox potential,” *Journal of Nuclear Medicine*, vol. 38, no. 7, pp. 1155–1160, 1997.
- [49] F. Dehdashti, P. W. Grigsby, M. A. Mintun, J. S. Lewis, B. A. Siegel, and M. J. Welch, “Assessing tumor hypoxia in cervical cancer by positron emission tomography with 60Cu-ATSM: relationship to therapeutic response—a preliminary report,” *International Journal of Radiation Oncology Biology Physics*, vol. 55, no. 5, pp. 1233–1238, 2003.

- [50] Y. Minagawa, K. Shizukuishi, I. Koike et al., "Assessment of tumor hypoxia by ^{62}Cu -ATSM PET/CT as a predictor of response in head and neck cancer: a pilot study," *Annals of Nuclear Medicine*, vol. 25, no. 5, pp. 339–345, 2011.
- [51] J. P. Holland, J. S. Lewis, and F. Dehdashti, "Assessing tumor hypoxia by positron emission tomography with Cu-ATSM," *The Quarterly Journal of Nuclear Medicine and Molecular Imaging*, vol. 53, no. 2, pp. 193–200, 2009.
- [52] J. S. Lewis, D. W. McCarthy, T. J. McCarthy, Y. Fujibayashi, and M. J. Welch, "Evaluation of ^{64}Cu -ATSM in vitro and in vivo in a hypoxic tumor model," *Journal of Nuclear Medicine*, vol. 40, no. 1, pp. 177–183, 1999.
- [53] K. Smallbone, D. J. Gavaghan, R. . Gatenby, and P. K. Maini, "The role of acidity in solid tumour growth and invasion," *Journal of Theoretical Biology*, vol. 235, no. 4, pp. 476–484, 2005.
- [54] K. Smallbone, R. A. Gatenby, and P. K. Maini, "Mathematical modelling of tumour acidity," *Journal of Theoretical Biology*, vol. 255, no. 1, pp. 106–112, 2008.
- [55] N. Viola-Villegas, V. Divilov, O. Andreev, Y. Reshetnyak, and J. Lewis, "Towards the improvement of an acidosis-targeting peptide PET tracer," *The Journal of Nuclear Medicine*, vol. 53, supplement 1, abstract no. 1673, 2012.
- [56] C. Nanni, S. Fanti, and D. Rubello, " ^{18}F -DOPA PET and PET/CT," *Journal of Nuclear Medicine*, vol. 48, no. 10, pp. 1577–1579, 2007.
- [57] A. Becherer, M. Szabó, G. Karanikas et al., "Imaging of advanced neuroendocrine tumors with ^{18}F -FDOPA PET," *The Journal of Nuclear Medicine*, vol. 45, no. 7, pp. 1161–1167, 2004.
- [58] L. M. Peterson, D. A. Mankoff, T. Lawton et al., "Quantitative imaging of estrogen receptor expression in breast cancer with PET and ^{18}F -fluoroestradiol," *The Journal of Nuclear Medicine*, vol. 49, no. 3, pp. 367–374, 2008.
- [59] G. Tomasi, F. Turkheimer, and E. Aboagye, "Importance of quantification for the analysis of PET data in oncology: review of current methods and trends for the future," *Molecular Imaging and Biology*, vol. 14, no. 2, pp. 131–136, 2012.
- [60] M. Vanderhoek, S. B. Perlman, and R. Jeraj, "Impact of different standardized uptake value measures on PET-based quantification of treatment response," *The Journal of Nuclear Medicine*, vol. 54, no. 8, pp. 1188–1194, 2013.
- [61] H. Watabe, Y. Ikoma, Y. Kimura, M. Naganawa, and M. Shidahara, "PET kinetic analysis—compartmental model," *Annals of Nuclear Medicine*, vol. 20, no. 9, pp. 583–588, 2006.
- [62] L. G. Strauss, A. Dimitrakopoulou-Strauss, and U. Haberkorn, "Shortened PET data acquisition protocol for the quantification of ^{18}F -FDG kinetics," *The Journal of Nuclear Medicine*, vol. 44, no. 12, pp. 1933–1939, 2003.
- [63] L. G. Strauss, L. Pan, C. Cheng, U. Haberkorn, and A. Dimitrakopoulou-Strauss, "Shortened acquisition protocols for the quantitative assessment of the 2-tissue-compartment model using dynamic PET/CT ^{18}F -FDG studies," *Journal of Nuclear Medicine*, vol. 52, no. 3, pp. 379–385, 2011.
- [64] C. Burger, G. Goerres, S. Schoenes, A. Buck, A. Lonn, and G. von Schulthess, "PET attenuation coefficients from CT images: experimental evaluation of the transformation of CT into PET 511-keV attenuation coefficients," *European Journal of Nuclear Medicine and Molecular Imaging*, vol. 29, no. 7, pp. 922–927, 2002.
- [65] *Clinical PET-CT in Radiology. Integrated Imaging in Oncology*, Springer Science+Business Media, New York, NY, USA, 2011.
- [66] A. C. Pfannenber, P. Aschoff, K. Brechtel et al., "Low dose non-enhanced CT versus standard dose contrast-enhanced CT in combined PET/CT protocols for staging and therapy planning in non-small cell lung cancer," *European Journal of Nuclear Medicine and Molecular Imaging*, vol. 34, no. 1, pp. 36–44, 2007.
- [67] C. G. Cronin, P. Prakash, and M. A. Blake, "Oral and IV contrast agents for the CT portion of PET/CT," *The American Journal of Roentgenology*, vol. 195, no. 1, pp. W5–W13, 2010.
- [68] S. K. Haerle, K. Strobel, N. Ahmad, A. Soltermann, D. T. Schmid, and S. J. Stoeckli, "Contrast-enhanced ^{18}F -FDG-PET/CT for the assessment of necrotic lymph node metastases," *Head and Neck*, vol. 33, no. 3, pp. 324–329, 2011.
- [69] E. Dizendorf, T. F. Hany, A. Buck, G. K. Von Schulthess, and C. Burger, "Cause and magnitude of the error induced by oral CT contrast agent in CT-based attenuation correction of PET emission studies," *The Journal of Nuclear Medicine*, vol. 44, no. 5, pp. 732–738, 2003.
- [70] O. Mawlawi, J. J. Erasmus, R. F. Munden et al., "Quantifying the effect of IV contrast media on integrated PET/CT: clinical evaluation," *The American Journal of Roentgenology*, vol. 186, no. 2, pp. 308–319, 2006.
- [71] Y. Liu, S. M. Sadowski, A. B. Weisbrod, E. Kebebew, R. M. Summers, and J. Yao, "Multimodal image driven patient specific tumor growth modeling," *Medical Image Computing and Computer-Assisted Intervention*, vol. 16, no. 3, pp. 283–290, 2013.

Research Article

Multimodality Functional Imaging in Radiation Therapy Planning: Relationships between Dynamic Contrast-Enhanced MRI, Diffusion-Weighted MRI, and 18F-FDG PET

Moisés Mera Iglesias,¹ David Aramburu Núñez,¹ José Luis del Olmo Claudio,¹ Antonio López Medina,¹ Iago Landesa-Vázquez,² Francisco Salvador Gómez,¹ Brandon Driscoll,³ Catherine Coolens,³ José L. Alba Castro,² and Victor Muñoz⁴

¹ Medical Physics Department and Radiological Protection, Galaria-Hospital do Meixoeiro-Complexo Hospitalario Universitario de Vigo, 36200 Vigo, Spain

² Signal Theory and Communications Department, University of Vigo, 36310 Vigo, Spain

³ Radiation Medicine Program, Princess Margaret Cancer Centre and University Health Network, Toronto, ON, Canada M5T 2M9

⁴ Radiation Oncology Department, Galaria-Hospital do Meixoeiro-Complexo Hospitalario Universitario de Vigo, 36200 Vigo, Spain

Correspondence should be addressed to Antonio López Medina; antonio.lopez.medina@sergas.es

Received 4 July 2014; Revised 15 September 2014; Accepted 10 October 2014

Academic Editor: Alexandru Dasu

Copyright © 2015 Moisés Mera Iglesias et al. This is an open access article distributed under the Creative Commons Attribution License, which permits unrestricted use, distribution, and reproduction in any medium, provided the original work is properly cited.

Objectives. Biologically guided radiotherapy needs an understanding of how different functional imaging techniques interact and link together. We analyse three functional imaging techniques that can be useful tools for achieving this objective. **Materials and Methods.** The three different imaging modalities from one selected patient are ADC maps, DCE-MRI, and 18F-FDG PET/CT, because they are widely used and give a great amount of complementary information. We show the relationship between these three datasets and evaluate them as markers for tumour response or hypoxia marker. Thus, vascularization measured using DCE-MRI parameters can determine tumour hypoxia, and ADC maps can be used for evaluating tumour response. **Results.** ADC and DCE-MRI include information from 18F-FDG, as glucose metabolism is associated with hypoxia and tumour cell density, although 18F-FDG includes more information about the malignancy of the tumour. The main disadvantage of ADC maps is the distortion, and we used only low distorted regions, and extracellular volume calculated from DCE-MRI can be considered equivalent to ADC in well-vascularized areas. **Conclusion.** A dataset for achieving the biologically guided radiotherapy must include a tumour density study and a hypoxia marker. This information can be achieved using only MRI data or only PET/CT studies or mixing both datasets.

1. Introduction

Radiotherapy is in a process of transformation from image-guided radiotherapy to biologically guided radiotherapy [1]. To this effect, in the last few years some commercial treatment units have been developed that include an MRI unit combined with a linac in a single device [2–5], and PET/CT (positron emission tomography/computed tomography) has proven useful for tumour staging and target delineation, especially in head and neck tumours and lung tumour [6–8]. The main change in clinical practice will arrive when the prescription of a treatment moves from dose prescribed to

target volumes and to prescription of results of a function, as tumour control probability, which considers all the radiobiological phenomena and adapts the treatment to early tumour response and uses different functional images as inputs. Although not widely available yet, several tools, methods, and models have been developed for achieving these objectives in a retrospective manner:

- (1) quantitative methods in diffusion-weighted imaging- (DW-) MRI providing ADC (apparent diffusion coefficient) maps that allow determining early tumour response [9–13],

- (2) in vivo measurement of hypoxia [14, 15], using either MRI datasets [16–22] or PET/CT [23–28],
- (3) inverse-planning optimisation algorithm that includes biological criteria [29, 30] and/or functional imaging information [31, 32] or even radiobiological models adapted to functional imaging information [33].

In this paper a case study is presented using datasets from 18F-FDG (fludeoxyglucose labelled with 18F) PET/CT, DW-MRI/ADC maps, and dynamic contrast-enhanced- (DCE-) MRI for characterizing tumour behaviour and for using the multimodality parameters as predictive values of tumour response from a patient included in the ARTFIBio project [34–36].

18F-FDG PET images the glucose consumption of each region. Tumour cells use glycolysis rather than lipolysis as the metabolic process to produce ATP and they use more glucose than normal cells. Glycolysis is a rather inefficient process and therefore large amounts of glucose are needed for cell survival and tumour growth. The PET enhancement (standard uptake value or SUV) in tumours is due to three different mechanisms: (i) cancer cells produce more ATP outside the mitochondria, even in well-oxygenated conditions (Warburg effect [37]); (ii) cancer cells proliferate more than normal tissue cells [38], and then they need more glucose; and, finally, (iii) cancer cells can survive in lower oxygenated regions better than normal tissue cells [39, 40] but consume more glucose because they need to produce ATP by glycolysis in absence of oxygen (Pasteur effect).

DW-MRI measures the diffusion of protons in a medium. Its principle is based on the attenuation of the signal according to Stejskal and Tanner's model [41]. Tumour cells are abnormal in size and shape compared to normal cells, and they are more tightly packed and have higher cellularity than the tissue from which they originate. The extracellular volume is smaller in tumour regions, and therefore the freedom of movements of protons in tumour regions is restricted [42, 43]. The logarithm of the signal attenuation is a function of the applied gradient, the gap between pulses of gradient, and the pulse duration. By varying these parameters during acquisition, the ADC can be calculated for each voxel.

DCE-MRI has been proposed by several authors for treatment monitoring [44–46] and for measurement of oxygenation distribution [19–22]. The main problem is the complexity of the data analysis and the correspondence between measurement and biological parameters. Another disadvantage is the necessity of a contrast agent.

In order to characterize the tumour and to implement new predictive models based on functional imaging data, we must ensure we can extract as much information as possible from the available data. Some of the main parameters to characterize tumour behaviour, along with radiotherapy treatment, must be initial tumour density, hypoxia, malignancy/proliferation, dose to each voxel, and timing of the dose. In this work, attention is focused on showing the relationship between ADC maps, DCE-MRI parameters, dose, and 18F-FDG PET/CT SUV (standard uptake value). Many other types of images can show the main parameters we are interested in modelling (18F-fluorothymidine for proliferation

[47], Zr-89-cetuximab for response to chemotherapy [31], and dynamic FDG [28] and fluoromisonidazole (FMISO) [26] for hypoxia), but it is hypothesized that the proposed combination of techniques can give us enough information about the tumour environment to assess the treatment response, but not the tumour microenvironment (data are averaged into the voxel size): the k_{trans} parameter in DCE-MRI is related to vascularization and then to hypoxia [18] and v_e is related to extracellular volume and in heterogeneously vascularized areas to tumour density [18]; SUV is related to tumour metabolism and then is related to malignancy (enhancement of the Warburg effect to the Pasteur effect), hypoxia (Pasteur effect), and tumour density and proliferation. Finally, ADC maps are related to water mobility and then to tumour density [12]. We will explore the relationships between ADC, DCE-MRI parameters, and SUV values and will evaluate their influence on tumour response in a case study where we have in the same slice a necrotic volume, a hypoxic area, and a heterogeneously vascularized tumour volume.

2. Material and Methods

2.1. Patients. This study is conducted in accordance with the Declaration of Helsinki [48] and the study protocol was approved by the local ethics committee; informed consent was obtained from all patients.

The aim of ARTFIBio project (<http://artfibio.cesga.es/Artfibio/application/>) is to create a network for sharing information and for developing predictive individualized models of the tumour response to radiotherapy in patients with head and neck cancer based on in vivo functional data. For this purpose, several studies of MRI and PET/CT were performed. Patients within the ARTFIBio project [34–36] had oropharyngeal cancer (squamous cancer cell) of stages T3 and T4. All of them are treated with IMRT (intensity-modulated radiation therapy) and the prescribed dose was between 66 Gy and 70 Gy to the local PTV. The imaging protocol (Figure 1) is as follows:

- (i) pretreatment: MRI study (DCE-MRI + ADC) and PET/CT study (18F-FDG),
- (ii) first control (10–30 Gy): MRI study (DCE-MRI + ADC),
- (iii) second control (30 Gy–60 Gy): MRI study (DCE-MRI + ADC),
- (iv) three months after the treatment: PET/CT and MRI study (DCE-MRI + ADC).

For all imaging studies the patient is positioned using the RT immobilisation devices. The geometrical distortion on MRI images and registration process (rigid registration and deformable registration) were checked with an MRI phantom. Regardless, only central slices showing low distortion were analysed. For each patient and each set of images the ADC values, contrast exchange coefficients (K_{trans}), SUV, dose, and Hounsfield units (HU) per voxel were recorded of each volume.

TABLE 1: Main parameters of MRI acquisition protocols.

Technique	TR/TE (ms)	Field of view (cm ²)	Matrix size	Slice thickness (mm)	Gap	Sense factor	Contrast agent
T1-Turbo Spin Echo	425/4.8	23 × 23	272 × 272	6	1	1.6	—
T2-Turbo Spin Echo	6171/90	23 × 23	320 × 312	6	1	1.6	—
ADC $b = 0, 600$ s/mm ²	5270/77	25 × 25	120 × 97	6	1	—	—
ADC $b = 0, 1000$ s/mm ²	5926/85	25 × 25	120 × 97	6	1	—	—
DCE-MRI-Dynamic T1 High Resolution Isotropic Volume Excitation (THRIVE)—7 series every 33 s	4.1/1.97	24 × 24	120 × 120	6	—	1.5	Gd

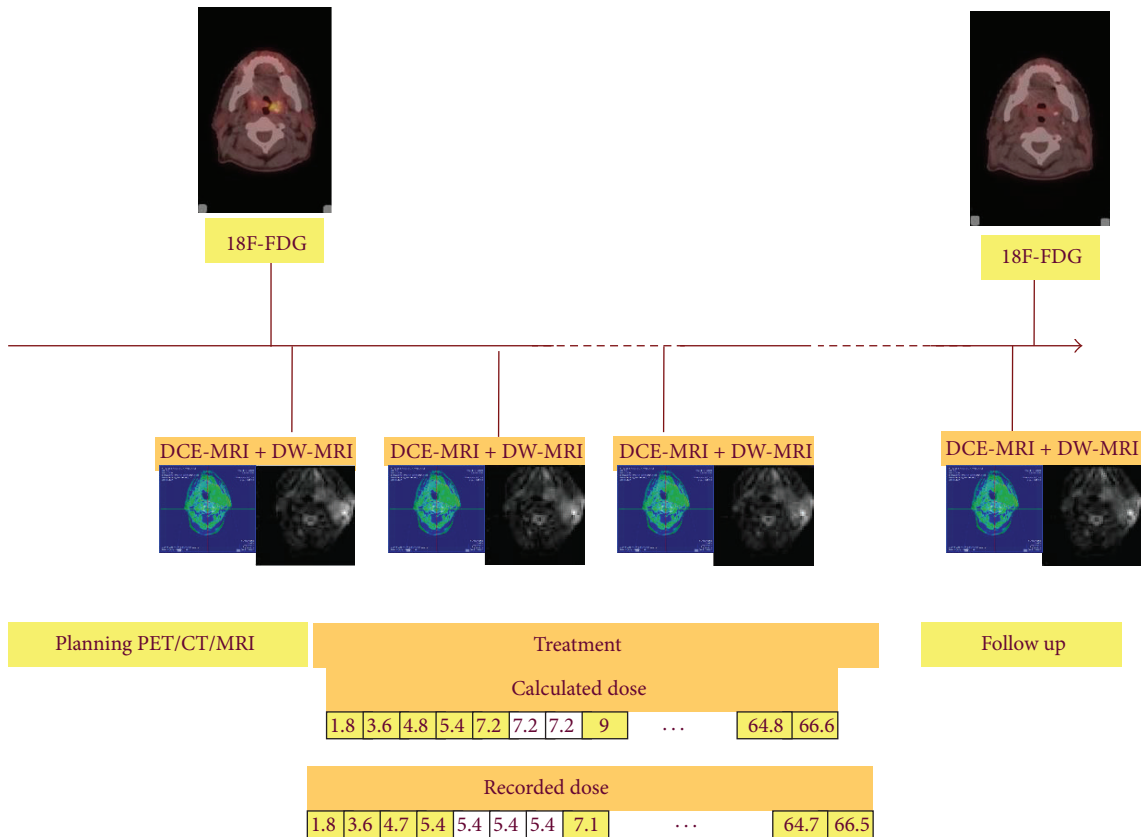


FIGURE 1: Scheme of the image acquisition process along the radiotherapy course.

In this paper a case study is highlighted from one patient who has three clearly differentiated volumes in a single slice: a heterogeneously vascularized tumour and a hypoxic region surrounding a necrotic area. This case is very useful to visualize and investigate the different behaviours of the tumour volumes in glucose metabolism and in treatment response.

2.2. Acquisition and Analysis of MR Images. All MRI examinations were performed on a 1.5-T scanner (Achieva; Philips Healthcare) with the patients in supine position. Routine T2-weighted, T1, DW-MRI, and DCE-MRI were obtained using the parameters showed in Table 1. Flex-L coil (Philips Sense Flex Medium) was placed over the neck. After image acquisition, pixel-to-pixel ADC map was reconstructed using

the standard software on the imaging console (Achieva; Philips Healthcare). According to Stejskal and Tanner's model [41] and considering the monoexponential approximation, the ADC value can be calculated using the following:

$$\text{ADC} = \frac{\ln(S_0/S_1)}{(b_1 - b_0)}, \quad (1)$$

where S_1 and S_0 are signal values of the images at b values, b_1 and b_0 , respectively, and ADC is the apparent diffusion coefficient obtained using $b_1 = 600$ and $b_0 = 0$.

A nonlinear model [49] was utilized to convert signal to gadolinium concentration in DCE-MRI as per Tofts [50]. It considers two different compartments: the blood plasma (or intravascular space) and the extracellular extravascular space

TABLE 2: Main parameters of the Tofts model.

Quantity	Definition
$C_a(t)$	Arterial concentration as a function of time
$C_t(t)$	Tissue concentration as a function of time
H_{ct}	Hematocrit volume
K_{trans}	Transfer constant from the blood plasma into the EES
K_{ep}	Transfer constant from the EES back to the blood plasma
T	Onset time of arterial contrast uptake
v_b	Whole blood volume per unit of tissue
v_e	Total EES volume ($v_e = K_{trans}/K_{ep}$)

(EES or interstitial space). The parameters utilized to generate the Tofts model are described in Table 2.

The relationship between all these parameters can be obtained by

$$C_t(t) = \frac{K_{trans}}{1 - H_{ct}} \left(C_a(t) \otimes e^{-K_{ep}(t-\tau)} \right) + V_b C_a(t). \quad (2)$$

A voxel-based perfusion analysis method was used based on the modified Tofts model [49]. A 3D voxel-wise perfusion analysis method [51, 52] was applied to the DCE-MRI data which generated perfusion parameters k_{trans} , k_{ep} , and v_b from the modified Tofts model. This method also provided semiquantitative metrics such as area under the curve (AUC) and time to max enhancement.

Variable flip angle (VFA) spoiled gradient recalled echo scans at three flip angles variations (5° , 10° , and 15°) were utilized to calculate the voxel by voxel Tl_0 of the GTV (gross tumour volume) of 3 different patients. The average Tl_0 of these patients (800 ms) was applied when calculating the concentration of the analyzed patient which unfortunately did not have VFA scans themselves.

The arterial input function (AIF) was chosen in the carotid artery near the base of skull.

2.3. Acquisition of PET/CT Images. Whole-body PET/CT scan was carried out from head to thigh, 60 min after intravenous administration of approximately 370 MBq ($\pm 10\%$) of ^{18}F -FDG on a PET/CT scanner (Discovery, GE Healthcare Bio-Sciences Corp.) with a 70 cm axial FOV, a 218×218 matrix. Study was acquired in 3D mode. The pixel spacing was 5.47 mm with a slice thickness of 3.27 mm. The spatial resolution to 1 cm varies from 3.99 mm to 4.56 mm. PET images were corrected for attenuation, scatter, decay, dead time, random coincidences, and slice sensitivity.

To calculate the SUV [53] for the selected patient and on a voxel by voxel basis, we took into account an injected activity of 345 MBq with a weight of the patient of 49 kg.

2.4. Noise Reduction and Registration. To reduce image noise a 3×3 nearest-neighbour smoothing filter was applied to the DCE-MRI, PET-CT, and ADC images. Deformable registration of the images, with the CT of treatment as reference, was performed using tailored in-house software specifically developed for the ARTFIBio project [36] and based on ITK

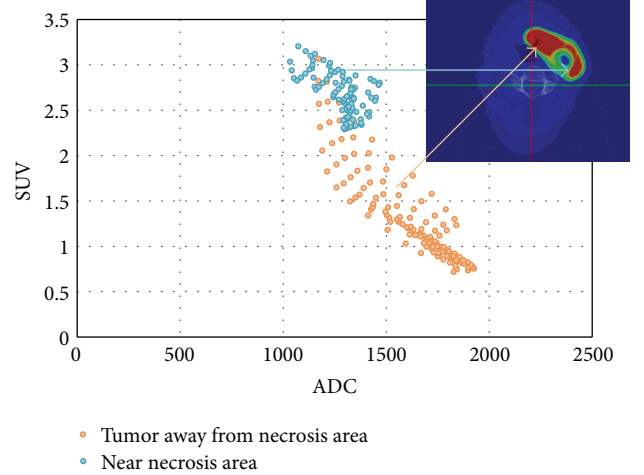


FIGURE 2: The relationship between SUV and ADC. In the hypoxic area (excluding necrotic area), high SUV values are obtained independently of the ADC value; this is explained by the addition of the Warburg effect and the Pasteur effect. In the heterogeneously vascularized area, SUV values decrease with ADC. This is likely a result of the fact that a reduction in ADC implies an increase in tumour cell density.

libraries [54]. Using the GTV contoured for radiation treatment, the numerical values of each voxel of the coregistered images were extracted. Bone and air voxels (as determined by CT) were dropped from the analysis profiles.

3. Results and Discussion

3.1. SUV versus ADC. The relationship between the different image datasets and functional parameters was investigated in order to achieve the best possible picture of the internal tumour dynamics. Using one representative patient a plot of SUV versus ADC for the CTV is displayed in Figure 2; the hypoxic area (low ADC, low K_{trans}), surrounding necrotic volume (medium-high ADC, low K_{trans}), and heterogeneously vascularized tumour (low ADC, high K_{trans}) have each been considered separately (Figure 2).

3.2. ADC versus v_e (DCE-MRI). Several parameters can be obtained from DCE-MRI, but only the relationships between K_{trans} and extracellular volume v_e have been investigated here.

In order to perform kinetic modeling of the tumour robust arterial input function (AIF) needs to be selected.

The AIF was chosen in the carotid artery near the base of skull for increased reproducibility since a larger variability was observed in the values of Tl_0 in the carotid at the level of the neck (Figure 3).

v_e should be most closely correlated to ADC information as the extracellular volume is related to the freedom of water molecules in the medium. Both sets of data were compared and they are represented in Figure 4.

For values of v_e greater than 0.02 (values less than this value correspond to badly vascularized areas and low K_{trans} in the studied data), a clear relationship between both datasets

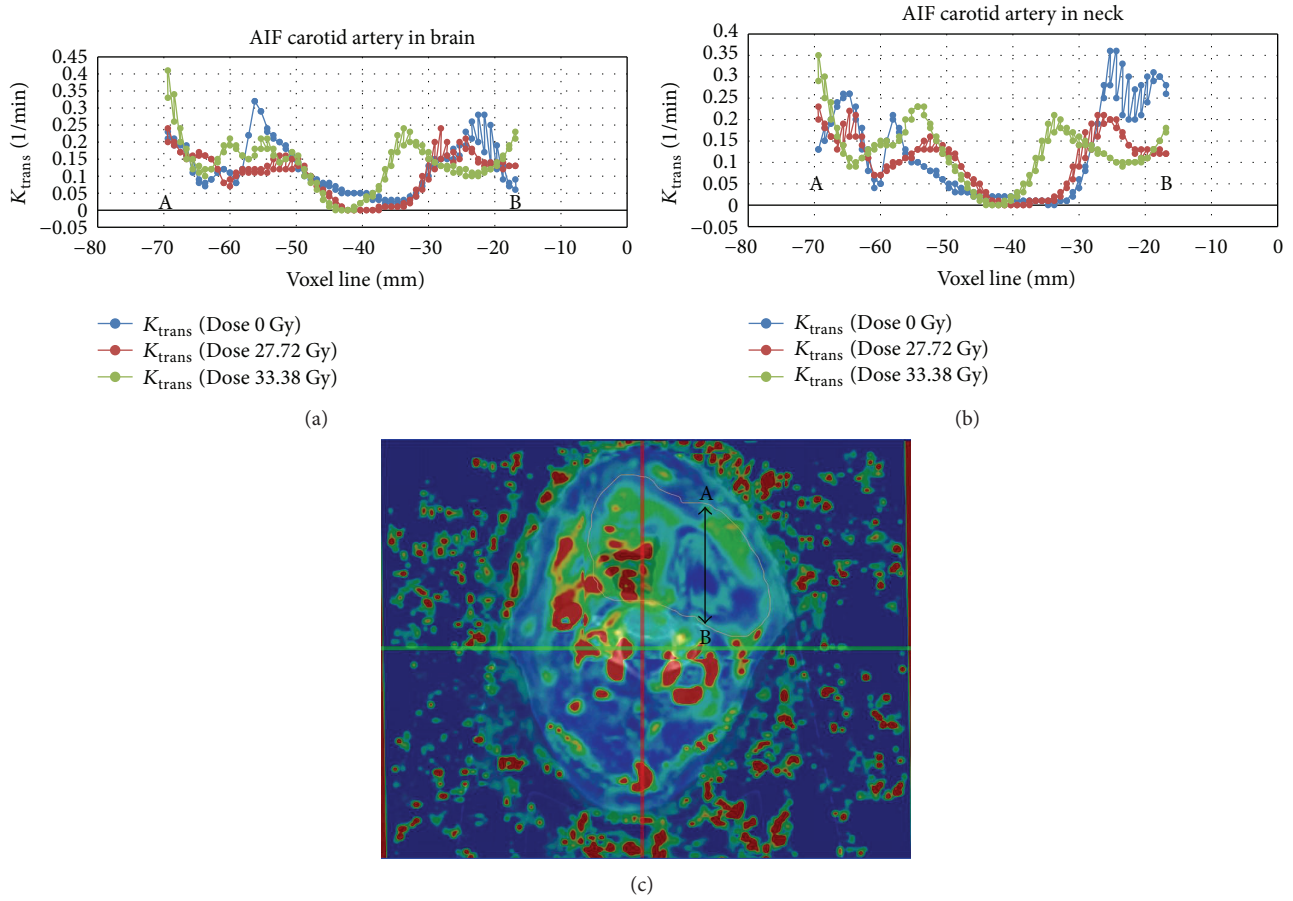


FIGURE 3: In this axial slice (bottom), k_{trans} is represented along (top) a voxel line at different stages of treatment (pretreatment, at 27.72 Gy, and at 33.38 Gy). We can see how k_{trans} increases with dose and the central U-shaped valley corresponding to the badly vascularized area is becoming increasingly narrow. In the upper left figure, we consider AIF from data of the carotid artery near brain, and in the lower left figure, we consider AIF from data of the carotid artery in neck.

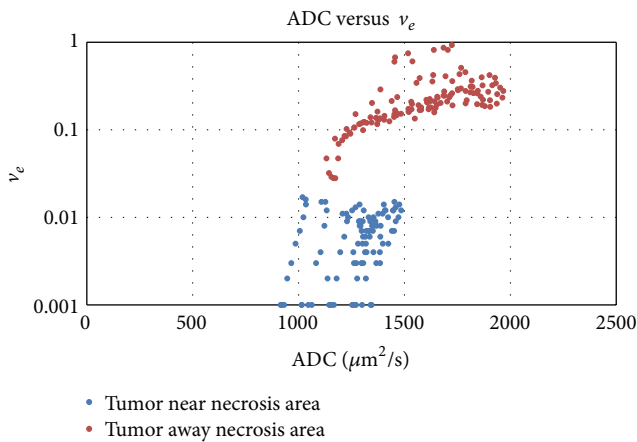


FIGURE 4: v_e versus ADC ($\mu\text{m}^2/\text{s}$) for the selected slice of the patient of Figure 3. In well-vascularized areas (red dots), a clear relationship can be found.

is found, indicating that a smaller extracellular volume corresponds to a higher tumour cell density in well-vascularized or heterogeneously vascularized areas but not hypoxic areas.

3.3. *SUV, ADC versus k_{trans} (DCE-MRI).* Of all the analyzed parameters, k_{trans} is the most related to vascularization. Vascularization must be related to oxygenation [55–59], as Figure 5 shows, because with increasing K_{trans} values, that is, increasing perfusion, SUV values decrease because of the reduction of the Pasteur effect (green dots, Figure 5(c)).

On the other hand, no clear relationship has been found between ADC map and k_{trans} values, although ADC values appear to be rather constant (blue dots, Figure 5(d)) because they are selected from a small homogeneous region. Additionally, tumour cells are able to survive in badly oxygenated areas and the tumour cell density is less variable in these areas.

3.4. *ADC versus Dose Influenced by K_{trans} .* We have generated the ADC values during the treatment for a heterogeneously vascularized tumour volume. In this case, the delivered dose to achieve an ADC value corresponding to normal tissue is much lower than for badly vascularized voxels. The influence of vascularization/oxygenation in the ADC response can be observed with the DCE-MRI studies, as shown in Figure 6.

3.5. *Discussion.* The results presented have some similarities to those obtained by Atuegwu et al. [12] and indicate that

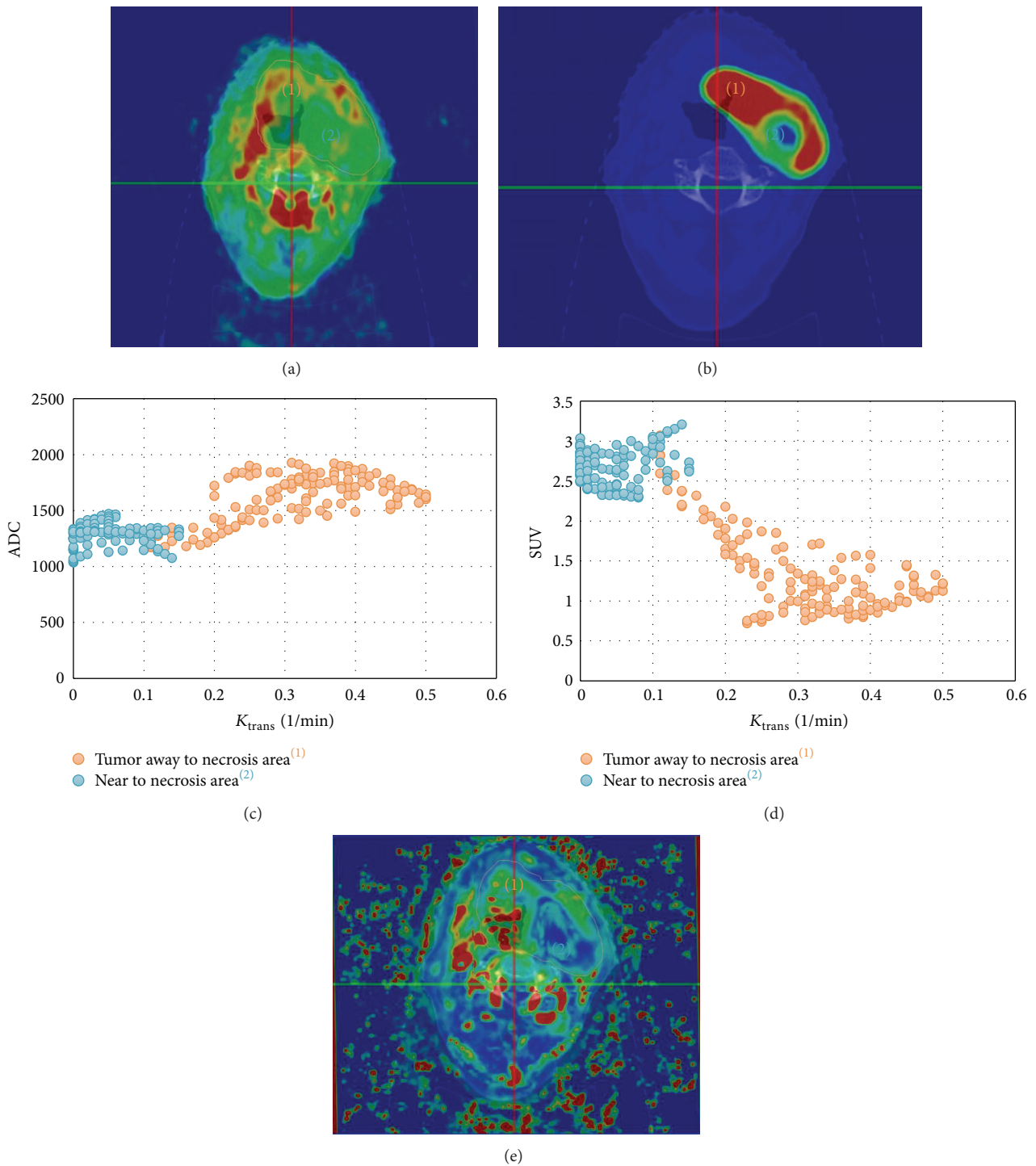


FIGURE 5: In this figure SUV versus K_{trans} and ADC versus K_{trans} are represented. (a) K_{trans} map overlaid on the simulation CT. (b) PET/CT. (c) In the hypoxic area (near necrotic area), high SUV values are obtained independently for all low K_{trans} values, because of the addition of the Warburg effect and the Pasteur effect. In the heterogeneously vascularized area, SUV values are decreasing with K_{trans} , as expected, because the Pasteur effect is reducing in this area as K_{trans} increases. (d) No clear relationship can be found between ADC and K_{trans} . (e) ADC map overlaid simulation CT.

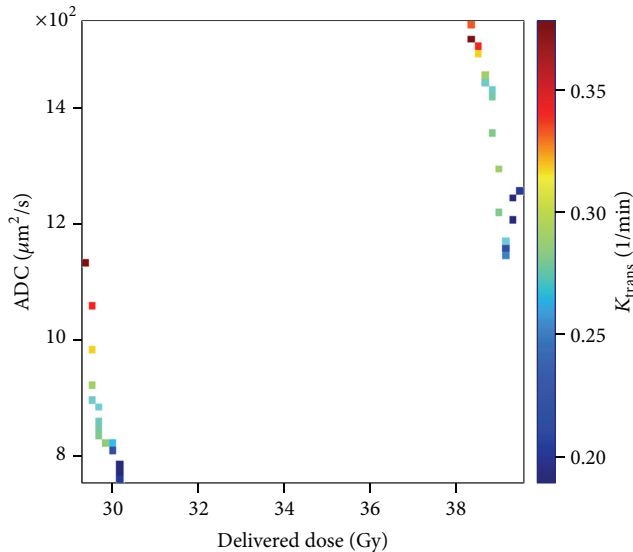


FIGURE 6: ADC values for a heterogeneously vascularized tumour volume are represented versus delivered dose (fractions 13th and 17th), and the colour represents the k_{trans} value. In this graph, it can be observed that heterogeneously vascularized voxels show a greater increment in ADC values.

ADC values can be a good marker of the tumour response [11, 12]. Further, the combination of biological information obtained from different modalities can improve the characterization of tumour behaviour. From our point of view, at least two different sets of data must be considered: one for tumour response and another one for hypoxia measurement. If geometrical distortion is not considered or can be corrected [60], ADC maps can be a suitable choice for tumour response.

The polarographic electrode has been considered by some authors as the gold standard for measuring tumour hypoxia in vivo [61], although theoretical simulations have shown that it gives only a qualitative characterisation. Considering only radiopharmaceuticals and PET/CT, the most common are FMISO [24, 26, 32, 33], dynamic FDG [28], and Cu-ATSM [47]. When considering MRI, typically BOLD [17] and DCE-MRI [19, 20, 22, 62] are the most widely used methods; however we have not found any study using them for modifying the treatment (as with FMISO [26, 33, 63]). Vascularity measurements from DCE-MRI data can provide a surrogate marker of tumour hypoxia, as was shown by Newbold et al. [20] and Donaldson et al. [21] in head and neck cancer. These measurements could potentially guide treatment [22] and are easy to obtain; however more studies are needed in order to apply to clinical practice, as input data either for dose painting or for delimiting hypoxic volumes.

^{18}F -FDG shows different aspects of the tumour behaviour, mainly associated with tumour cell density, malignancy, and oxygenation, and the quotient between ADC and SUV has been proposed as a measurement of malignancy in breast tumours [64] and in invasive ductal cancer [65]. These last papers found correlation between maximum SUV and bad prognoses that could be explained because high SUV can be associated with hypoxic areas as we have observed.

Using biomechanical models [66] that consider both the dynamics of the tumour and variation of tumour density (including diffusion) and oxygenation along the treatment, instead of static models, can be quite useful for increasing the predictability of the models.

ADC maps appear to be a good option for evaluating tumour response; however their disadvantage is image distortion. Unfortunately, this cannot be corrected using standard deformable registration algorithm, but reversed gradients method looks like a very promising algorithm to solve this problem [60]. It is possible that extracellular volume calculated from DCE-MRI can be used as an equivalent of ADC values in well-vascularized areas.

4. Conclusions

Multimodality imaging offers much more information about tumour behaviour than the individual datasets on their own. The relationship between different types of images must be studied in detail in order to establish a minimum set of data required to personalize the radiotherapy treatment and to optimize the treatment for each patient. This could comprise not only a gradient of dose along the treatment, but also different fractionation for each voxel.

Multicentre studies can be useful for recruitment of a large number of patients and increase the statistical power of the results, if imaging standards and protocol compliance are followed [67].

Voxel by voxel analysis seems possible if we consider small volumes and undistorted regions from ADC maps or corrected data.

Conflict of Interests

The authors declare that there is no conflict of interests regarding the publication of this paper.

Acknowledgments

The authors offer their sincerest thanks to patients who volunteered to participate in this study. The authors also would like to acknowledge Neil Burnet and Michael Simmons for their helpful comments about this text and the editorial committee for inviting them to collaborate in this special issue. The authors must be grateful for the exchange program of the Spanish Society of Medical Physics (SEFM) that funded the first author's visit to Princess Margaret Cancer Centre. The authors thank the National Health Institute of Spain for supporting this work with ISCIII Grant PI11/02035 and the Galician Government through Project CN 2012/260 "Consolidation Research Units: AtlantTIC."

References

- [1] C. Grau, M. Hoyer, M. Alber, J. Overgaard, J. C. Lindgaard, and L. P. Muren, "Biology-guided adaptive radiotherapy (BiGART)—more than a vision?" *Acta Oncologica*, vol. 52, no. 7, pp. 1243–1247, 2013.

- [2] K. Smit, B. van Asselen, J. G. M. Kok, A. H. L. Aalbers, J. J. W. Lagendijk, and B. W. Raaymakers, "Towards reference dosimetry for the MR-linac: magnetic field correction of the ionization chamber reading," *Physics in Medicine and Biology*, vol. 58, no. 17, pp. 5945–5957, 2013.
- [3] D. Saenz, B. Paliwal, and J. Bayouth, "A dose homogeneity and conformity evaluation between ViewRay and pinnacle-based linear accelerator IMRT treatment plans," *Journal of Medical Physics*, vol. 39, no. 2, pp. 64–70, 2014.
- [4] J. Winter, M. Westmore, M. Dahan et al., "Patient alignment in MRI guided radiation therapy," US Patent 20130235969 A1, 2013.
- [5] B. W. Raaymakers, J. J. W. Lagendijk, J. Overweg et al., "Integrating a 1.5 T MRI scanner with a 6 MV accelerator: proof of concept," *Physics in Medicine and Biology*, vol. 54, no. 12, pp. N229–N237, 2009.
- [6] V. Grégoire, K. Haustermans, X. Geets, S. Roels, and M. Lon-neux, "PET-based treatment planning in radiotherapy: a new standard?" *Journal of Nuclear Medicine*, vol. 48, supplement 1, pp. 68S–77S, 2007.
- [7] M. Lonneux, M. Hamoir, H. Reyckler et al., "Positron emission tomography with [¹⁸F]fluorodeoxyglucose improves staging and patient management in patients with head and neck squamous cell carcinoma: a multicenter prospective study," *Journal of Clinical Oncology*, vol. 28, no. 7, pp. 1190–1195, 2010.
- [8] M. MacManus, U. Nestle, K. E. Rosenzweig et al., "Use of PET and PET/CT for radiation therapy planning: IAEA expert report 2006–2007," *Radiotherapy and Oncology*, vol. 91, no. 1, pp. 85–94, 2009.
- [9] D. A. Hamstra, T. L. Chenevert, B. A. Moffat et al., "Evaluation of the functional diffusion map as an early biomarker of time-to-progression and overall survival in high-grade glioma," *Proceedings of the National Academy of Sciences of the United States of America*, vol. 102, no. 46, pp. 16759–16764, 2005.
- [10] C. J. Galbán, S. K. Mukherji, T. L. Chenevert et al., "A feasibility study of parametric response map analysis of diffusion-weighted magnetic resonance imaging scans of head and neck cancer patients for providing early detection of therapeutic efficacy," *Translational Oncology*, vol. 2, no. 3, pp. 184–190, 2009.
- [11] S. Kim, L. Loevner, H. Quon et al., "Diffusion-weighted magnetic resonance imaging for predicting and detecting early response to chemoradiation therapy of squamous cell carcinomas of the head and neck," *Clinical Cancer Research*, vol. 15, no. 3, pp. 986–994, 2009.
- [12] N. C. Atuegwu, J. C. Gore, and T. E. Yankeelov, "The integration of quantitative multi-modality imaging data into mathematical models of tumors," *Physics in Medicine and Biology*, vol. 55, no. 9, pp. 2429–2449, 2010.
- [13] L. A. P. Romasanta, M. J. G. Velloso, and A. L. Medina, "Functional imaging in radiation therapy planning for head and neck cancer," *Reports of Practical Oncology and Radiotherapy*, vol. 18, no. 6, pp. 376–382, 2013.
- [14] J. M. Arbeit, J. M. Brown, K. S. C. Chao et al., "Hypoxia: importance in tumor biology, noninvasive measurement by imaging, and value of its measurement in the management of cancer therapy," *International Journal of Radiation Biology*, vol. 82, no. 10, pp. 699–757, 2006.
- [15] A. R. Padhani, K. A. Krohn, J. S. Lewis, and M. Alber, "Imaging oxygenation of human tumours," *European Radiology*, vol. 17, no. 4, pp. 861–872, 2007.
- [16] Y. Cao, C. I. Tsien, V. Nagesh et al., "Clinical investigation survival prediction in high-grade gliomas by MRI perfusion before and during early stage of RT," *International Journal of Radiation Oncology Biology Physics*, vol. 64, no. 3, pp. 876–885, 2006.
- [17] J. F. Dunn, J. A. O'Hara, Y. Zaim-Wadghiri et al., "Changes in oxygenation of intracranial tumors with carbogen: a BOLD MRI and EPR oximetry study," *Journal of Magnetic Resonance Imaging*, vol. 16, no. 5, pp. 511–521, 2002.
- [18] M. A. Zahra, K. G. Hollingsworth, E. Sala, D. J. Lomas, and L. T. Tan, "Dynamic contrast-enhanced MRI as a predictor of tumour response to radiotherapy," *The Lancet Oncology*, vol. 8, no. 1, pp. 63–74, 2007.
- [19] J. T. Elliott, E. A. Wright, K. M. Tichauer et al., "Arterial input function of an optical tracer for dynamic contrast enhanced imaging can be determined from pulse oximetry oxygen saturation measurements," *Physics in Medicine and Biology*, vol. 57, no. 24, pp. 8285–8295, 2012.
- [20] K. Newbold, I. Castellano, E. Charles-Edwards et al., "An exploratory study into the role of dynamic contrast-enhanced magnetic resonance imaging or perfusion computed tomography for detection of intratumoral hypoxia in head and neck cancer," *International Journal of Radiation Oncology Biology Physics*, vol. 74, no. 1, pp. 29–37, 2009.
- [21] S. B. Donaldson, G. Betts, S. C. Bonington et al., "Perfusion estimated with rapid dynamic contrast-enhanced magnetic resonance imaging correlates inversely with vascular endothelial growth factor expression and pimonidazole staining in head-and-neck cancer: a pilot study," *International Journal of Radiation Oncology Biology Physics*, vol. 81, no. 4, pp. 1176–1183, 2011.
- [22] J. M. Berstein, J. J. Homer, and C. M. West, "Dynamic contrast-enhanced magnetic resonance imaging biomarkers in head and neck cancer: potential to guide treatment? A systematic review," *Oral Oncology*, vol. 50, no. 10, pp. 963–970, 2014.
- [23] M. Busk, M. R. Horsman, S. Jakobsen et al., "Can hypoxia-PET map hypoxic cell density heterogeneity accurately in an animal tumor model at a clinically obtainable image contrast?" *Radiotherapy and Oncology*, vol. 92, no. 3, pp. 429–436, 2009.
- [24] N. Y. Lee, J. G. Mechalakos, S. Nehmeh et al., "Fluorine-18-labeled fluoromisonidazole positron emission and computed tomography-guided intensity-modulated radiotherapy for head and neck cancer: a feasibility study," *International Journal of Radiation Oncology, Biology, Physics*, vol. 70, no. 1, pp. 2–13, 2008.
- [25] S. A. Nehmeh, N. Y. Lee, H. Schröder et al., "Reproducibility of intratumor distribution of (18)F-fluoromisonidazole in head and neck cancer," *International Journal of Radiation Oncology Biology Physics*, vol. 70, no. 1, pp. 235–242, 2008.
- [26] D. Thorwarth, S.-M. Eschmann, F. Paulsen, and M. Alber, "Hypoxia dose painting by numbers: a planning study," *International Journal of Radiation Oncology Biology Physics*, vol. 68, no. 1, pp. 291–300, 2007.
- [27] S.-M. Eschmann, F. Paulsen, M. Reimold et al., "Prognostic impact of hypoxia imaging with ¹⁸F-misonidazole PET in non-small cell lung cancer and head and neck cancer before radiotherapy," *Journal of Nuclear Medicine*, vol. 46, no. 2, pp. 253–260, 2005.
- [28] K. Røe, T. B. Aleksandersen, A. Kristian et al., "Preclinical dynamic 18F-FDG PET tumor characterization and radiotherapy response assessment by kinetic compartment analysis," *Acta Oncologica*, vol. 49, no. 7, pp. 914–921, 2010.

- [29] V. A. Semenenko, B. Reitz, E. Day, X. S. Qi, M. Miften, and X. A. Li, "Evaluation of a commercial biologically based IMRT treatment planning system," *Medical Physics*, vol. 35, no. 12, pp. 5851–5860, 2008.
- [30] P. Stavrev, D. Hristov, B. Warkentin, E. Sham, N. Stavreva, and B. G. Fallone, "Inverse treatment planning by physically constrained minimization of a biological objective function," *Medical Physics*, vol. 30, no. 11, pp. 2948–2958, 2003.
- [31] J. Heukelom, O. Hamming, H. Bartelink et al., "Adaptive and innovative Radiation Treatment FOR improving Cancer treatment outcomE (ARTFORCE); a randomized controlled phase II trial for individualized treatment of head and neck cancer," *BMC Cancer*, vol. 13, article 84, 2013.
- [32] D. Thorwarth and M. Alber, "Implementation of hypoxia imaging into treatment planning and delivery," *Radiotherapy and Oncology*, vol. 97, no. 2, pp. 172–175, 2010.
- [33] I. Toma-Dasu, J. Uhrdin, L. Antonovic et al., "Dose prescription and treatment planning based on FMISO-PET hypoxia," *Acta Oncologica*, vol. 51, no. 2, pp. 222–230, 2012.
- [34] A. López Medina, D. Aramburu, M. Mera et al., "ARTFIBio project: quantifying tumour response voxel by voxel," *Radiotherapy & Oncology*, vol. 106, p. S329, 2013.
- [35] A. L. Medina, D. Aramburu, M. Mera et al., "Tumour response: a multiparametric function," *Radiotherapy & Oncology*, vol. 111, supplement 1, pp. 149–150, 2014.
- [36] I. Landesa-Vázquez, J. Alba-Castro, M. Mera-Iglesias, D. Aramburu-Núñez, A. López-Medina, and V. Muñoz-Garzón, "ART-FIBio: a cross-platform image registration tool for tumor response quantification in head and neck cancer," in *Proceedings of the IEEE-EMBS International Conference on Biomedical and Health Informatics (BHI '14)*, pp. 149–152, Valencia, Spain, June 2014.
- [37] O. Warburg, "On the origin of cancer cells," *Science*, vol. 123, no. 3191, pp. 309–314, 1956.
- [38] T. Roose, S. J. Chapman, and P. K. Maini, "Mathematical models of avascular tumor growth," *SIAM Review*, vol. 49, no. 2, pp. 179–208, 2007.
- [39] M. Busk, M. R. Horsman, P. E. G. Kristjansen, A. J. van der Kogel, J. Bussink, and J. Overgaard, "Aerobic glycolysis in cancers: implications for the usability of oxygen-responsive genes and fluorodeoxyglucose-PET as markers of tissue hypoxia," *International Journal of Cancer*, vol. 122, no. 12, pp. 2726–2734, 2008.
- [40] R. A. Gatenby, E. T. Gawlinski, A. F. Gmitro, B. Kaylor, and R. J. Gillies, "Acid-mediated tumor invasion: a multidisciplinary study," *Cancer Research*, vol. 66, no. 10, pp. 5216–5223, 2006.
- [41] E. O. Stejskal and J. E. Tanner, "Spin diffusion measurements: spin echoes in the presence of a time-dependent field gradient," *The Journal of Chemical Physics*, vol. 42, no. 1, pp. 288–292, 1965.
- [42] D.-M. Koh and D. J. Collins, "Diffusion-weighted MRI in the body: applications and challenges in oncology," *American Journal of Roentgenology*, vol. 188, no. 6, pp. 1622–1635, 2007.
- [43] A. C. Morani, K. M. Elsayes, P. S. Liu et al., "Abdominal applications of diffusion-weighted magnetic resonance imaging: where do we stand?" *World Journal of Radiology*, vol. 5, no. 3, pp. 68–80, 2013.
- [44] J. F. Kallehauge, C. Nomden, and A. C. S. de Castro, "Temporal changes in DCE-MRI parameters during treatment of locally advanced cervical cancer," *Radiotherapy & Oncology*, vol. 103, p. S78, 2012.
- [45] D. S. Yoo, J. P. Kirkpatrick, O. Craciunescu et al., "Prospective trial of synchronous bevacizumab, erlotinib, and concurrent chemoradiation in locally advanced head and neck cancer," *Clinical Cancer Research*, vol. 18, no. 5, pp. 1404–1414, 2012.
- [46] D. Zheng, Y. Chen, X. Liu et al., "Early response to chemoradiotherapy for nasopharyngeal carcinoma treatment: value of dynamic contrast-enhanced 3.0 T MRI," *Journal of Magnetic Resonance Imaging*, 2014.
- [47] B. Titz and R. Jeraj, "An imaging-based tumour growth and treatment response model: investigating the effect of tumour oxygenation on radiation therapy response," *Physics in Medicine and Biology*, vol. 53, no. 17, pp. 4471–4488, 2008.
- [48] World Medical Organization, "Declaration of Helsinki," *British Medical Journal*, vol. 313, no. 7070, pp. 1448–1449, 1996.
- [49] <http://www.thedcetool.com/scientific>.
- [50] P. S. Tofts, "Modeling tracer kinetics in dynamic Gd-DTPA MR imaging," *Journal of Magnetic Resonance Imaging*, vol. 7, no. 1, pp. 91–101, 1997.
- [51] C. Coolens, B. Driscoll, C. Chung et al., "Automated voxel-based analysis of volumetric DCE CT data improves the measurement of serial changes in tumor vascular biomarkers," *International Journal of Radiation Oncology, Biology, Physics*. In press.
- [52] W. Foltz, B. Driscoll, S. J. Lee et al., "Comparison of arterial input functions by magnitude and phase signal measurement in dynamic contrast enhancement MRI using a dynamic flow phantom," *Medical Physics*. In press.
- [53] IAEA, *Quantitative Nuclear Medicine Imaging: Concepts, Requirements and Methods*. IAEA Library, 2014.
- [54] En línea, <http://www.itk.org/>.
- [55] T. W. Secomb, R. Hsu, M. W. Dewhirst, B. Klitzman, and J. F. Gross, "Analysis of oxygen transport to tumor tissue by microvascular networks," *International Journal of Radiation Oncology, Biology, Physics*, vol. 25, no. 3, pp. 481–489, 1993.
- [56] C. J. Kelly and M. Brady, "A model to simulate tumour oxygenation and dynamic [18F]-Fmiso PET data," *Physics in Medicine and Biology*, vol. 51, no. 22, pp. 5859–5873, 2006.
- [57] S. S. Foo, D. F. Abbott, N. Lawrentschuk, and A. M. Scott, "Functional imaging of intratumoral hypoxia," *Molecular Imaging and Biology*, vol. 6, no. 5, pp. 291–305, 2004.
- [58] R. A. Cooper, B. M. Carrington, J. A. Lancaster et al., "Tumour oxygenation levels correlate with dynamic contrast-enhanced magnetic resonance imaging parameters in carcinoma of the cervix," *Radiotherapy and Oncology*, vol. 57, no. 1, pp. 53–59, 2000.
- [59] H. Lyng, A. O. Vorren, K. SundfØr et al., "Assessment of tumor oxygenation in human cervical carcinoma by use of dynamic Gd-DTPA-enhanced MR imaging," *Journal of Magnetic Resonance Imaging*, vol. 14, no. 6, pp. 750–756, 2001.
- [60] P. S. Morgan, R. W. Bowtell, D. J. O. McIntyre, and B. S. Worthington, "Correction of spatial distortion in EPI due to inhomogeneous static magnetic fields using the reversed gradient method," *Journal of Magnetic Resonance Imaging*, vol. 19, no. 4, pp. 499–507, 2004.
- [61] J. G. Eriksen and M. R. Horsman, "Tumour hypoxia—a characteristic feature with a complex molecular background," *Radiotherapy and Oncology*, vol. 81, no. 2, pp. 119–121, 2006.
- [62] T. E. Yankeelov, M. Lepage, A. Chakravarthy et al., "Integration of quantitative DCE-MRI and ADC mapping to monitor treatment response in human breast cancer: initial results," *Magnetic Resonance Imaging*, vol. 25, no. 1, pp. 1–13, 2007.

- [63] P. Dirix, V. Vandecaveye, F. De Keyzer, S. Stroobants, R. Hermans, and S. Nuyts, "Dose painting in radiotherapy for head and neck squamous cell carcinoma: value of repeated functional imaging with ^{18}F -FDG PET, ^{18}F -fluoromisonidazole PET, diffusion-weighted MRI, and dynamic contrast-enhanced MRI," *Journal of Nuclear Medicine*, vol. 50, no. 7, pp. 1020–1027, 2009.
- [64] S. Baba, T. Isoda, Y. Maruoka et al., "Diagnostic and prognostic value of pretreatment SUV in ^{18}F -FDG/ PET in breast cancer: comparison with apparent diffusion coefficient from diffusion-weighted MR imaging," *Journal of Nuclear Medicine*, vol. 55, no. 5, pp. 736–742, 2014.
- [65] B. B. Choi, S. H. Kim, B. J. Kang et al., "Diffusion-weighted imaging and FDG PET/CT: predicting the prognoses with apparent diffusion coefficient values and maximum standardized uptake values in patients with invasive ductal carcinoma," *World Journal of Surgical Oncology*, vol. 10, article 126, 2012.
- [66] J. A. Weis, M. I. Miga, L. R. Arlinghaus et al., "A mechanically coupled reaction-diffusion model for predicting the response of breast tumors to neoadjuvant chemotherapy," *Physics in Medicine and Biology*, vol. 58, no. 17, pp. 5851–5866, 2013.
- [67] B. Driscoll, H. Keller, D. Jaffray, and C. Coolens, "Development of a dynamic quality assurance testing protocol for multisite clinical trial DCE-CT accreditation," *Medical Physics*, vol. 40, no. 8, Article ID 081906, 2013.

Research Article

Modeling the Relationship between Fluorodeoxyglucose Uptake and Tumor Radioresistance as a Function of the Tumor Microenvironment

Jeho Jeong and Joseph O. Deasy

The Department of Medical Physics, Memorial Sloan Kettering Cancer Center, New York, NY 10065, USA

Correspondence should be addressed to Joseph O. Deasy; deasyj@mskcc.org

Received 4 July 2014; Accepted 25 August 2014; Published 8 September 2014

Academic Editor: Iuliana Toma-Dasu

Copyright © 2014 J. Jeong and J. O. Deasy. This is an open access article distributed under the Creative Commons Attribution License, which permits unrestricted use, distribution, and reproduction in any medium, provided the original work is properly cited.

High fluorodeoxyglucose positron emission tomography (FDG-PET) uptake in tumors has often been correlated with increasing local failure and shorter overall survival, but the radiobiological mechanisms of this uptake are unclear. We explore the relationship between FDG-PET uptake and tumor radioresistance using a mechanistic model that considers cellular status as a function of microenvironmental conditions, including proliferating cells with access to oxygen and glucose, metabolically active cells with access to glucose but not oxygen, and severely hypoxic cells that are starving. However, it is unclear what the precise uptake levels of glucose should be for cells that receive oxygen and glucose versus cells that only receive glucose. Different potential FDG uptake profiles, as a function of the microenvironment, were simulated. Predicted tumor doses for 50% control (TD_{50}) in 2 Gy fractions were estimated for each assumed uptake profile and for various possible cell mixtures. The results support the hypothesis of an increased avidity of FDG for cells in the intermediate stress state (those receiving glucose but not oxygen) compared to well-oxygenated (and proliferating) cells.

1. Introduction

As the most commonly used functional imaging modality in oncology, ^{18}F -labeled fluorodeoxyglucose positron emission tomography (FDG-PET) has played a valuable role since first being synthesized in 1978 [1]. Most malignant tumors exhibit an elevated glucose uptake and FDG-PET, as a close glucose chemical analogy, results in an image of glucose uptake in the patient, offering unique information for cancer detection, staging, target definition, and response monitoring [2, 3].

As a significant predictor of prognosis in radiation therapy (RT), FDG uptake seems to reflect an increased radioresistance; however, this is poorly understood. Many clinical outcome analyses have verified that high uptake of FDG in a tumor is correlated with increased local failure and shorter survival for many tumor sites, as summarized in several meta-analyses [4–7]. Therefore, FDG-avid regions in a tumor are recognized as a possible target for dose escalation to compensate for the radioresistance [8, 9]. Recently, utilizing a novel meta-analysis tool, we showed that FDG-avid head and neck

tumors require about 20% more doses to equalize the local control rate with FDG nonavid tumors [10], although tumor size confounded that analysis to an unknown extent.

Enhanced glycolysis of tumor cells is certainly related to hypoxia, because hypoxic cells produce energy (in the form of ATP molecules) through glycolysis, without oxygen. However, it is also known that tumor cells can show increased glycolysis even in the presence of oxygen, compared to normal cells (the “Warberg effect”) [11, 12]. The oncolytic appetite for glycolysis is thought to be caused by a number of genetic or possibly epigenetic changes that drive malignancy [13, 14].

Many studies have been carried out to correlate FDG uptake with various physiological parameters, such as hypoxia, proliferation, blood flow, histology, and differentiation, utilizing FDG-PET and immunohistochemical methods [15–20]. However, although several studies have shown the relationship between the FDG uptake and hypoxia or proliferation, the underlying mechanism of FDG uptake in a tumor is still unclear.

In this study, we do not try to resolve the detailed mechanism of FDG uptake. However, we do test various assumptions correlating FDG uptake (and presumably glucose consumption) with local cell microenvironmental conditions. The model is an attempt to incorporate known radiobiological effects that have been established as being important to understand radiotherapy treatment response, such as varying access to oxygen and glucose as well as the basic mathematical features of tumors, including variable growth fractions and cell loss factors. The key starting point of the model is that there is a limited amount of chemical resources for each tumor subvolume and that this level of resources is assumed to remain constant over a course of radiotherapy. We therefore used the model to determine the assumptions relating FDG uptake to the underlying cell compartments that best fits the observed correspondence between FDG uptake and reduced local control.

2. Methods

2.1. State-Driven Tumor Response Model. To explore the potential relationship between FDG-PET uptake and classical radiobiological mechanisms, a previously developed state-based tumor response model was used [21]. In the mechanistic model, a tumor was assumed to be comprised of many small tumorlets of a PET-voxel-comparable size ($4 \times 4 \times 4 \text{ mm}^3$). Each tumorlet is comprised of three subpopulations of cells based on the level of proliferation, hypoxia, and cell loss, which is thought to be related to the available amount of oxygen and glucose, as shown by Kiran et al. [22]. Figure 1 shows the three compartments of a tumorlet in a typical tumor microenvironment. Proliferation was assumed to take place only in the *P*-compartment, wherein cells have access to glucose and oxygen, whereas cell loss in the absence of treatment only takes place in the *H*-compartment, wherein cells have no access to either oxygen or glucose. The intermediate cells in the *I*-compartment, which have access to glucose but not oxygen, were assumed to be metabolically active but do not proliferate.

After RT begins, damaged cells (as deterministically calculated by linear-quadratic model) become doomed according to a compartment-specific radiosensitivity, leading to mitotic cell death when doomed cells are attempting to proliferate in the *P*-compartment. As doomed cells die, metabolically active but hypoxic cells in the *I*-compartment receive oxygen and move into the *P*-compartment, causing reoxygenation. The model assumes a locally-constant blood supply over the course of RT. The transition of cells between compartments is determined dynamically, with the *P*-compartment always taking as many cells from the *I*-compartment as can be supported.

As a discrete-time simulation algorithm, the model keeps updating the number of cells in each compartment in a small time step. In each time step, a fraction of cells in the *P*-compartment proliferate, cell loss takes place in the *H*-compartment, the doomed cells in the *P*-compartment die probabilistically following mitosis, and the cells are re-compartmentalized based on the capacity of each compartment.

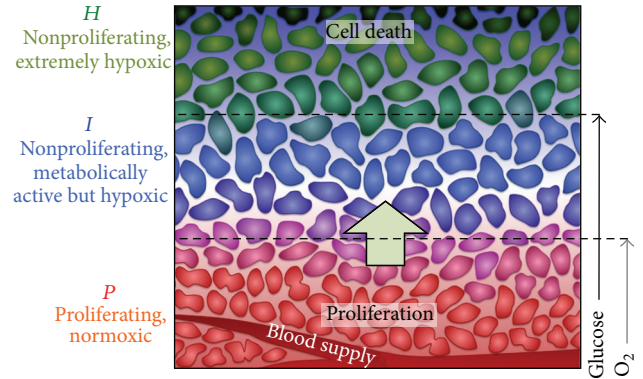


FIGURE 1: Cartoon of the microenvironment with respect to the blood supply. Due to a limited blood supply, there are limited supplies of the oxygen and the key nutrient, glucose. Cells with adequate oxygen and glucose are actively proliferating, while cells distant from vessels are starving and dying. In the model, these populations of cells were simplified into three different compartments (*P*, *I*, and *H*) that have different levels of proliferation, hypoxia, cell death, and radiosensitivity. Note that uniform levels of glucose and O_2 were assumed for each compartment.

At the time of RT fraction, a fraction of viable cells in each compartment becomes doomed according to compartment-specific radiosensitivity value.

The model can be used to evaluate clinically important phenomena, including fraction size effects, the reoxygenation effect, repopulation effects, and tumor regression. Details of the mathematical model are available elsewhere [21].

2.2. Hypothetical FDG Uptake Patterns. We consider different relative uptakes of FDG within the three compartments. The subpopulations of tumor cells in the model were distinguished based on oxygen and glucose availability [22]: only the *P*- and *I*-compartments were thought to be associated with FDG uptake given the model assumptions. Based on correlation studies between FDG and physiological factors, three different potential relationships between FDG uptake and cell subpopulations are considered here: (1) FDG uptake is proportional to the total number of metabolically viable cells (*pattern I*); (2) FDG uptake is associated mainly with proliferating cells with a reduced contribution from intermediate cells (*pattern II*); and (3) the FDG uptake is associated mainly with the intermediate cells with a reduced contribution from proliferating cells (*pattern III*), all shown in Figure 2. A reduced contribution from extremely hypoxic (starving and dying) cells in the *H*-compartment was additionally tested (*uptake pattern IV*).

2.3. Model Simulation. The model simulations were performed for a tumorlet treated with a standard RT regime of $2 \text{ Gy}/\text{fx}$ ($5 \text{ fx}/\text{week}$). The size of tumorlet was set to be 64 mm^3 (based on typical PET-voxel size) with 6.4×10^7 cells, assuming the tumor cell density of 10^6 mm^{-3} . Only a small subset of cells is known to have stem-cell-like property and 1% of viable cells were assumed to be clonogenic cells in the model [23].

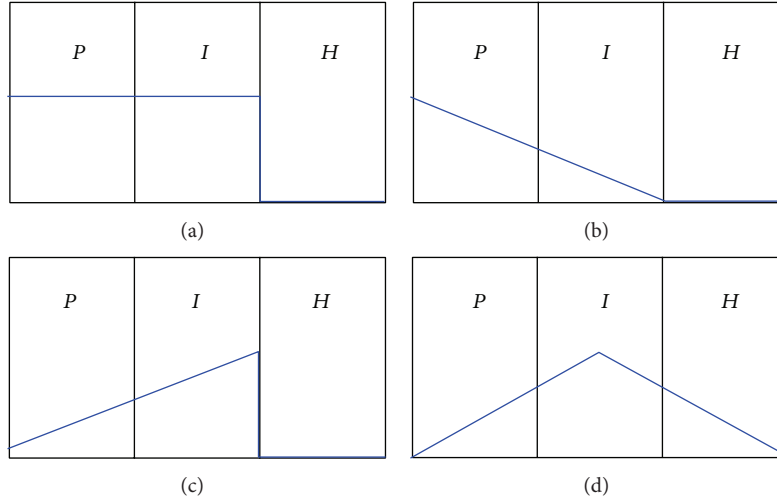


FIGURE 2: Assumed FDG uptake patterns in each compartment. We use straight lines to emphasize that uptake probably varies across compartments, even though this variation is simplified in the model. The FDG uptake patterns were assumed to be (a) proportional to the total number of viable cells (*pattern I*), (b) associated mainly with proliferation with a minor contribution from intermediate hypoxic cells (*pattern II*), (c) associated mainly with intermediate hypoxia with a minor contribution from proliferating cells (*pattern III*), and (d) associated mainly with intermediate hypoxic cells with minor contributions from proliferating and extremely hypoxic/dying cells (*pattern IV*). Note that the sizes of the three compartments are variable depending on the microenvironmental conditions, although they are shown with the same size in the figure.

TABLE 1: Parameter values for different compartments and the ranges of GF and CLF used in the model simulation.

Compartment	<i>P</i>	<i>I</i>	<i>H</i>
Oxygen enhancement ratio (OER)	1	2	1.37
Glucose uptake level per cell	Varies depending on the hypothetical FDG uptake pattern ^a		
Proliferation fraction	50–100% ^b	—	—
Cell loss mechanism and rate	Mitotic cell death due to irradiation (survival rate of each progeny after mitosis: 0.3)	—	Cell loss due to starvation (cell loss half time: 2 days)
Growth fraction (GF) range applied	0.01 to 1/(2 + CLF) [0.01 step]		
Cell loss factor (CLF) range applied	0.03 to 0.99 [0.03 step]		

^aThe relative uptake ratios in *P*:*I*:*H* are 1:1:0, 3:1:0, 1:3:0, and 2:5:2 for patterns I, II, III, and IV, respectively, as shown in Figure 2.

^bDepends on the fullness of the compartment: 50% of proliferation was assumed when the compartment is full, and 100% of proliferation was assumed when the number of cells is less than half of the capacity of the *P*-compartment.

Based on previous work [21], relevant parameter values for head and neck squamous cell carcinoma (HNSCC) were used, including the radiosensitivity of the *P*-compartment ($\alpha_p = 0.382 \text{ Gy}^{-1}$, $\alpha/\beta = 6.63 \text{ Gy}$). Hypoxic cells in the *I*- and *H*-compartments are considered to be only in the G0/G1-phase and the OER values for the *I*- and *H*-compartments were assumed to be 2 and 1.37, respectively, considering the lower OER of the G0/G1-phase and reduced repair capability of chronically hypoxic/highly stressed cells in the *H*-compartment [24].

The initial distribution of cells in each compartment is determined based on the presumed growth fraction (GF) and cell loss factor (CLF). As the GF increases, more cells are in proliferation and the *P*-compartment becomes larger. Given a higher CLF, more cells are starving and dying, resulting in a larger *H*-compartment. To consider a wide range of possible microenvironmental conditions, all possible ranges of initial

cell distributions were simulated, based on various combinations of GFs and CLFs (1315 combinations). The parameter values for different compartments and the ranges of GF and CLF used in the simulation are summarized in Table 1.

2.4. Correlation between FDG Uptake and TD_{50} . For each assumed FDG uptake pattern, the FDG uptake values were quantified for all possible ranges of initial distributions of cells in each compartment. Then, simulations were performed to determine the tumor dose for 50% control (TD_{50}) for all the possible ranges of initial cell distributions. The TD_{50} value was estimated from the Poisson formalism based on the total number of clonogenic cells in the tumorlet. Finally, we correlated the resulting FDG uptake values with the corresponding TD_{50} values and determined the linear correlation coefficient for comparison purposes.

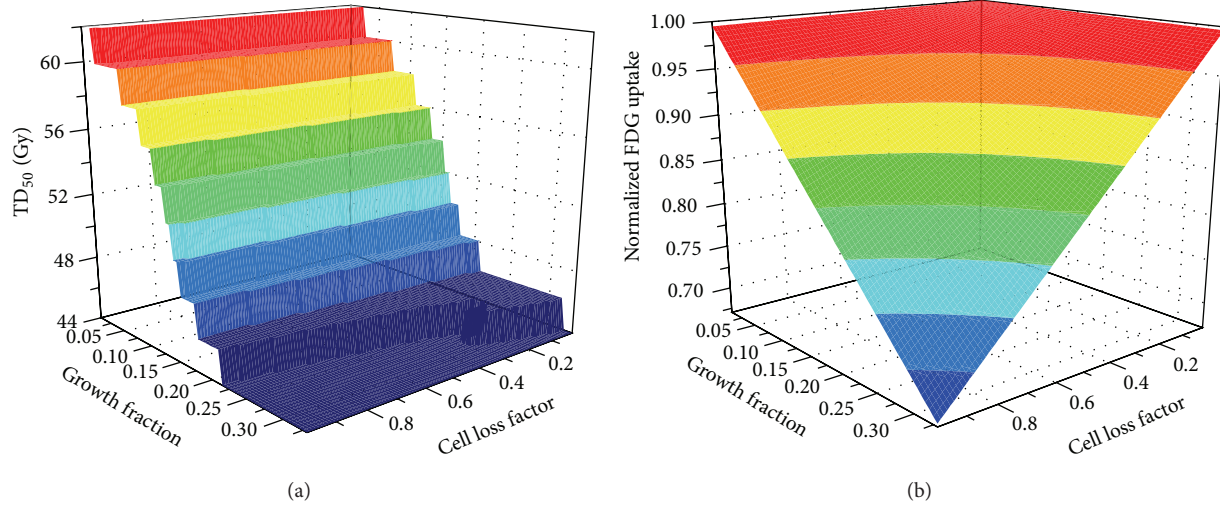


FIGURE 3: (a) Model predicted tumor dose for 50% control (TD_{50}) assuming 2 Gy/fx and (b) normalized FDG uptake (for *pattern I*) for all possible initial conditions as a function of growth fraction (GF) and cell loss factor (CLF).

3. Results

Estimated TD_{50} values for all possible ranges of initial conditions are shown in Figure 3(a). TD_{50} increased as the growth fraction decreased, due to a larger fraction of cells in the hypoxic compartments. TD_{50} decreased as the cell loss factor increased but the dependency of TD_{50} on the cell loss factor was much less significant compared to dependence on the growth fraction. The FDG uptake value was also quantified for all possible initial conditions based on the hypothesized FDG uptake patterns, as shown in Figure 3(b) for the uptake *pattern I*.

Hypothetical correlations between FDG uptake levels and corresponding TD_{50} values are shown in Figure 4, for the four different hypothetical FDG uptake patterns. For the first assumed pattern (*pattern I*), where the FDG uptake was assumed to be proportional to the total number of viable cells, only a weak positive correlation was observed between FDG uptake and TD_{50} value with a coefficient of determination (R^2) of 0.38. When the uptake pattern was assumed to be mainly associated with cell proliferation with a minor contribution from intermediate cells (*pattern II*), a significant negative correlation existed between FDG uptake and TD_{50} ($R^2 = 0.76$). For the hypothesis that metabolically-viable hypoxic cells in the *I*-compartment are avid for FDG uptake (*pattern III*), a strong positive correlation resulted ($R^2 = 0.85$). Inclusion of a reduced contribution from extremely hypoxic/starving cells in the *H*-compartment (*pattern IV*) yielded almost the same result as uptake *pattern III*, but with a slightly higher value of coefficient of determination ($R^2 = 0.86$), because the cells in *H*-compartment are either dying or reoxygenated into the *I*-compartment during the course of RT.

To better understand the potential relationship between FDG uptake and growth fraction (GF), the correlation between FDG uptake (for *pattern IV*) and TD_{50} was evaluated for a fixed cell loss factor of 0.9, as shown in Figure 5. For

the assumed uptake pattern, the FDG uptake was inversely correlated with the median GF in each bin.

4. Discussion

Potential causes for the observed clinical correlation between FDG and radioresistance was explored using a mathematical model, in which classical radiobiological mechanisms were incorporated. Several different FDG uptake patterns were explored. Among the assumed FDG uptake patterns, when the metabolically viable hypoxic compartment (the *I*-compartment) was assumed to dominate the FDG uptake (uptake *pattern III* or *IV*), a significant positive correlation between FDG uptake and the required TD_{50} was observed ($R^2 = 0.85$ or 0.86 , resp.), implying that the increased cellular radioresistance due to chronic hypoxia may be the cause of the clinically observed increase in tumor radioresistance.

We tested for any potential role of starving and dying cells (in the *H*-compartment). When the total number of cells in each hypoxic compartment (*I*- or *H*-compartment) was correlated with the required TD_{50} values, a strong positive correlation was observed for the *I*-compartment ($R^2 = 0.86$) but a weak negative correlation for the *H*-compartment ($R^2 = 0.38$), as shown in Figure 6.

This implies that the extremely hypoxic cells in the *H*-compartment are not the cause of an increased radioresistance. Mathematically, this is due to the lower OER value of the *H*-compartment used for the model simulation ($OER_H = 1.37$), compared to the OER of the *I*-compartment ($OER_I = 2$). To better understand this point, higher values of OER_H ($OER_H = 2$ or 3) were simulated (results not shown). Although the significance of the correlation was slightly reduced as the OER_H increased; quantitatively similar relationships were observed. Even when the OER_H was assumed to be as high as 3, which is certainly unreasonable radiobiologically, a strong correlation between the required TD_{50}

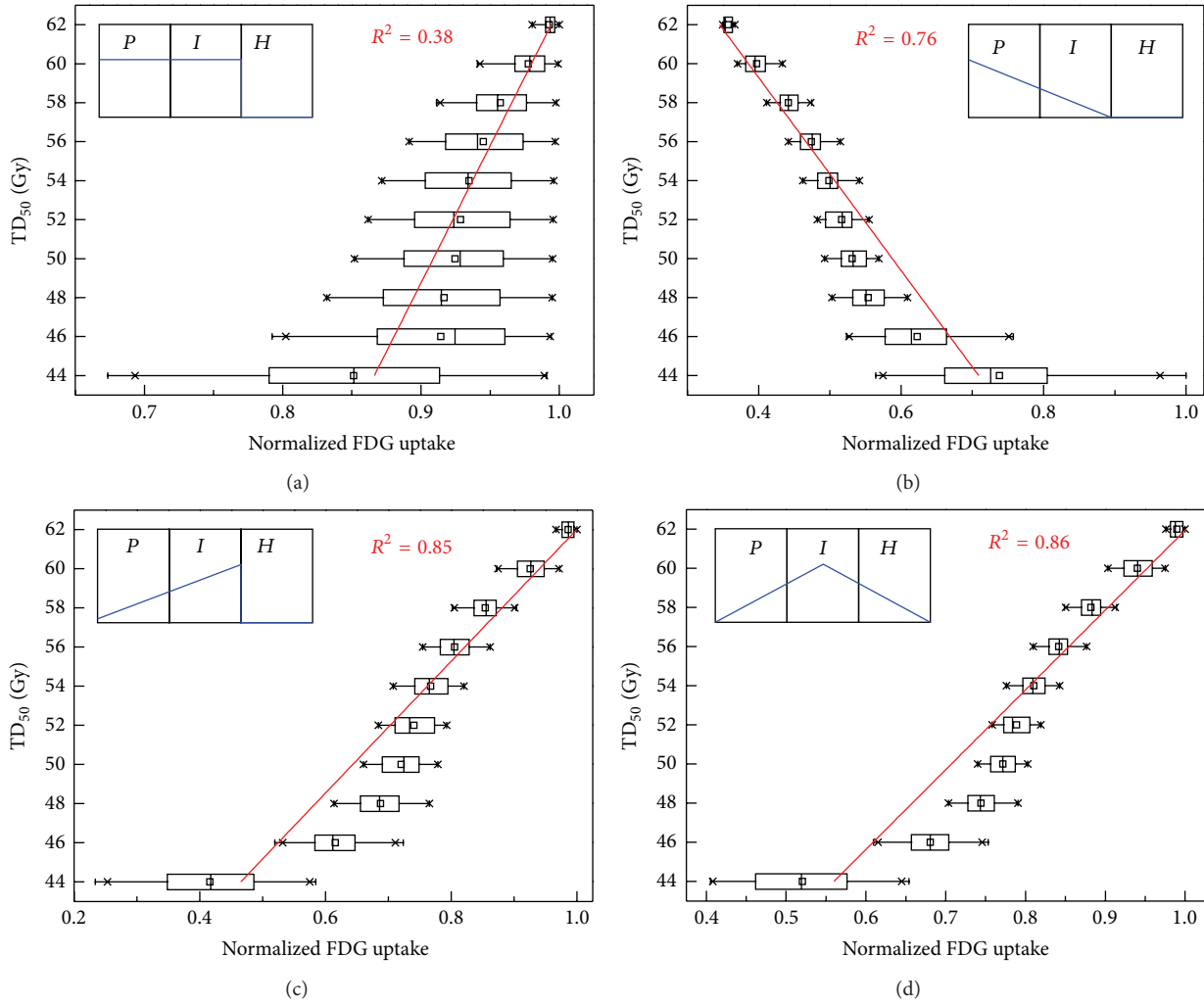


FIGURE 4: Correlations between model predicted tumor dose for 50% control (TD_{50}) in 2 Gy/fx and FDG uptake (normalized to maximum) for four different hypothetical uptake patterns. For each plot, all possible ranges of initial distributions of cells were simulated based on various combinations of growth fractions and cell loss factors. Note that each box in the plot represents 25th to 75th percentile of the dataset with tails for whole range.

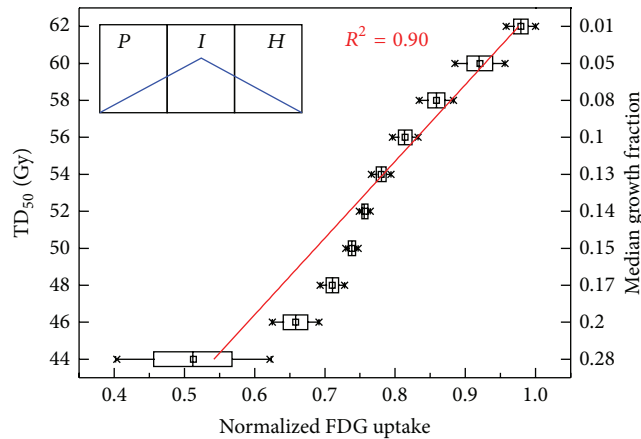


FIGURE 5: Model predicted tumor dose for 50% control (TD_{50}) in 2 Gy/fx versus FDG uptake (normalized to maximum) with median growth fraction value for each TD_{50} group (right axis) for FDG uptake *pattern IV* with fixed cell loss factor of 0.9. Note that each box in the plot represents 25th to 75th percentile of the dataset with tails for whole range.

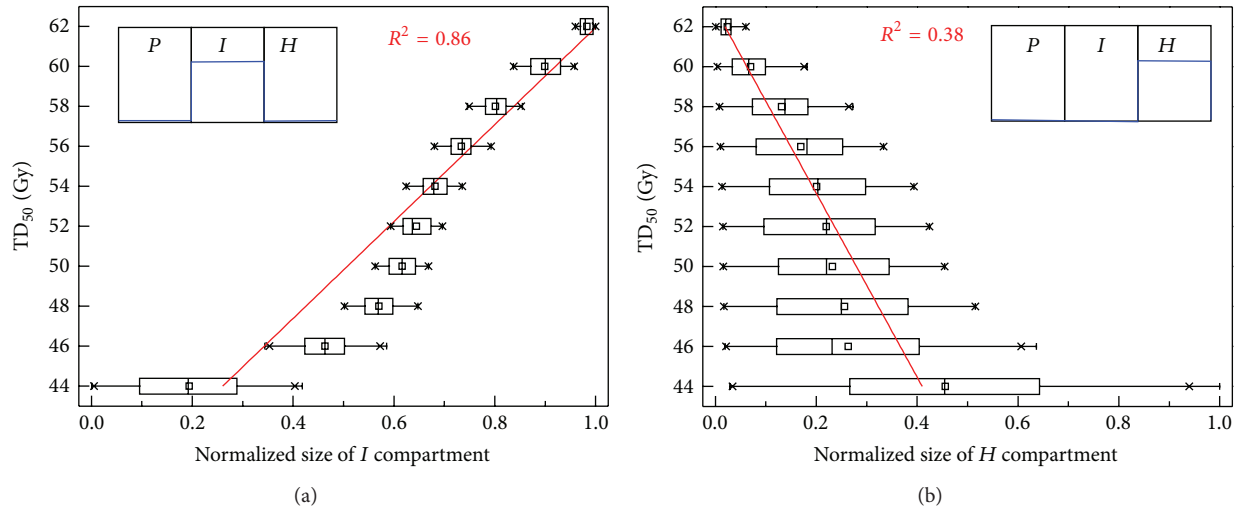


FIGURE 6: Model predicted tumor dose for 50% control (TD_{50}) in 2 Gy/fx versus the number of cells in (a) I -compartment or (b) H -compartment. Note that each box in the plot represents 25th to 75th percentile of the dataset with tails for whole range.

and the intermediate hypoxia in the I -compartment was still present ($R^2 = 0.83$).

In this work, it was assumed that there is no proliferation in the I -compartment for simplicity. Although it is known that some cells can proliferate even in hypoxic condition [25], the effect was evaluated to be not that significant due to the trade-off between increased proliferation and increased mitotic cell death, as shown in the previous work [21].

The ratio of TD_{50} values between high versus low FDG uptake tumorlets, separated by median normalized FDG uptake, was estimated to be about 1.24 for the most likely uptake pattern, *pattern III*. This implies that high FDG uptake tumorlets require about 24% extra dose, which agrees with the clinically estimated range of the extra dose ($\sim 20\%$) for FDG-avid head and neck cancers [10]. However, this estimate might be an over-estimate of the effect, since it assumes maximum heterogeneity of CLF and GF parameters, as shown in Table 1.

The results suggest that the total number of metabolically viable hypoxic cells (in I -compartment of the model) is a deterministic factor in tumor response and this subpopulation might be associated with the voxel-by-voxel correlation studies performed by Pugachev et al. [16] and Rajendran et al. [15], in which the microregional relationship between FDG and hypoxia was observed. Also the result supports the study of Wouters and Brown, in which the importance of the cells at intermediate oxygen level was emphasized [26].

5. Conclusion

In this work, the potential relationship between FDG-PET uptake and classical radiobiological mechanisms was explored using a mathematical framework based on a law of conservation of chemical resources. Several different FDG uptake patterns were hypothesized and the estimated FDG uptake values were correlated with tumor dose for 50% control (TD_{50}) using the state-driven tumor response model. The

model could generate a correlation between FDG uptake and an increase in tumor radioresistance when it was assumed that cells receiving glucose but not oxygen take up more glucose than cells that are well-oxygenated. Establishing this correspondence further, and understanding its limitations, will require appropriate FDG-PET clinical datasets.

Conflict of Interests

The authors declare that there is no conflict of interests regarding the publication of this paper.

Acknowledgments

This research was supported by Enid A. Haupt Medical Physics Endowed Chair fund at Memorial Sloan-Kettering Cancer Center, as well as the Nuclear Science and Engineering Institute of the University of Missouri and the Department of Radiation Oncology of the Washington University School of Medicine.

References

- [1] T. Ido, C.-N. Wan, and V. Casella, "Labeled 2-deoxy-D-glucose analogs. ^{18}F -labeled 2-deoxy-2-fluoro-D-glucose, 2-deoxy-2-fluoro-D-mannose and ^{14}C -deoxy-2-fluoro-D-glucose," *Journal of Labelled Compounds and Radiopharmaceuticals*, vol. 14, no. 2, pp. 175–183, 1978.
- [2] M. H. M. Janssen, H. J. W. L. Aerts, M. C. Öllers et al., "Tumor delineation based on time-activity curve differences assessed with dynamic fluorodeoxyglucose positron emission tomography-computed tomography in rectal cancer patients," *International Journal of Radiation Oncology Biology Physics*, vol. 73, no. 2, pp. 456–465, 2009.
- [3] S. Ben-Haim and P. Ell, " ^{18}F -FDG PET and PET/CT in the evaluation of cancer treatment response," *Journal of Nuclear Medicine*, vol. 50, no. 1, pp. 88–99, 2009.

- [4] P. Xie, M. Li, H. Zhao, X. Sun, Z. Fu, and J. Yu, “ ^{18}F -FDG PET or PET-CT to evaluate prognosis for head and neck cancer: a meta-analysis,” *Journal of Cancer Research and Clinical Oncology*, vol. 137, no. 7, pp. 1085–1093, 2011.
- [5] H. Ghooshkhanei, G. Treglia, G. Sabouri, R. Davoodi, and R. Sadeghi, “Risk stratification and prognosis determination using ^{18}F -FDG PET imaging in endometrial cancer patients: a systematic review and meta-analysis,” *Gynecologic Oncology*, vol. 132, no. 3, pp. 669–676, 2014.
- [6] K. Pak, G. J. Cheon, H. Y. Nam et al., “Prognostic value of metabolic tumor volume and total lesion glycolysis in head and neck cancer: a systematic review and meta-analysis,” *Journal of Nuclear Medicine*, vol. 55, no. 6, pp. 884–890, 2014.
- [7] Z. Wang, J.-Q. Chen, J.-L. Liu, X.-G. Qin, and Y. Huang, “FDG-PET in diagnosis, staging and prognosis of pancreatic carcinoma: a meta-analysis,” *World Journal of Gastroenterology*, vol. 19, no. 29, pp. 4808–4817, 2013.
- [8] M. Feng, F.-M. Kong, M. Gross, S. Fernando, J. A. Hayman, and R. K. Ten Haken, “Using fluorodeoxyglucose positron emission tomography to assess tumor volume during radiotherapy for non-small-cell lung cancer and its potential impact on adaptive dose escalation and normal tissue sparing,” *International Journal of Radiation Oncology Biology Physics*, vol. 73, no. 4, pp. 1228–1234, 2009.
- [9] D. de Ruyscher, S. Wanders, A. Mincken et al., “Effects of radiotherapy planning with a dedicated combined PET-CT-simulator of patients with non-small cell lung cancer on dose limiting normal tissues and radiation dose-escalation: a planning study,” *Radiotherapy and Oncology*, vol. 77, no. 1, pp. 5–10, 2005.
- [10] J. Jeong, J. S. Setton, N. Y. Lee, J. H. Oh, and J. O. Deasy, “Estimate of the impact of FDG-avidity on the dose required for head and neck radiotherapy local control,” *Radiotherapy and Oncology*, vol. 111, no. 3, pp. 340–347, 2014.
- [11] O. Warburg, “On the origin of cancer cells,” *Science*, vol. 123, no. 3191, pp. 309–314, 1956.
- [12] R. A. Gatenby and R. J. Gillies, “Why do cancers have high aerobic glycolysis?” *Nature Reviews Cancer*, vol. 4, no. 11, pp. 891–899, 2004.
- [13] J.-W. Kim and C. V. Dang, “Cancer’s molecular sweet tooth and the warburg effect,” *Cancer Research*, vol. 66, no. 18, pp. 8927–8930, 2006.
- [14] M. G. V. Heiden, L. C. Cantley, and C. B. Thompson, “Understanding the warburg effect: the metabolic requirements of cell proliferation,” *Science*, vol. 324, no. 5930, pp. 1029–1033, 2009.
- [15] J. G. Rajendran, D. A. Mankoff, F. O’Sullivan et al., “Hypoxia and glucose metabolism in malignant tumors: evaluation by [^{18}F]Fluoromisonidazole and [^{18}F]fluorodeoxyglucose positron emission tomography imaging,” *Clinical Cancer Research*, vol. 10, no. 7, pp. 2245–2252, 2004.
- [16] A. Pugachev, S. Ruan, S. Carlin et al., “Dependence of FDG uptake on tumor microenvironment,” *International Journal of Radiation Oncology Biology Physics*, vol. 62, no. 2, pp. 545–553, 2005.
- [17] M. Zimny, B. Gagel, E. DiMartino et al., “FDG—a marker of tumour hypoxia? A comparison with [^{18}F] fluoromisonidazole and pO_2 -polarography in metastatic head and neck cancer,” *European Journal of Nuclear Medicine and Molecular Imaging*, vol. 33, no. 12, pp. 1426–1431, 2006.
- [18] I. Buchmann, U. Haberkorn, I. Schmidtman et al., “Influence of cell proportions and proliferation rates on FDG uptake in squamous-cell esophageal carcinoma: a PET study,” *Cancer Biotherapy and Radiopharmaceuticals*, vol. 23, no. 2, pp. 172–180, 2008.
- [19] R. A. Dierckx and C. van de Wiele, “FDG uptake, a surrogate of tumour hypoxia?” *European Journal of Nuclear Medicine and Molecular Imaging*, vol. 35, no. 8, pp. 1544–1549, 2008.
- [20] H. Vesselle, A. Salskov, E. Turcotte et al., “Relationship between non-small cell lung cancer FDG uptake at PET, tumor histology, and Ki-67 proliferation index,” *Journal of Thoracic Oncology*, vol. 3, no. 9, pp. 971–978, 2008.
- [21] J. Jeong, K. I. Shoghi, and J. O. Deasy, “Modelling the interplay between hypoxia and proliferation in radiotherapy tumour response,” *Physics in Medicine and Biology*, vol. 58, no. 14, pp. 4897–4919, 2013.
- [22] K. L. Kiran, D. Jayachandran, and S. Lakshminarayanan, “Mathematical modelling of avascular tumour growth based on diffusion of nutrients and its validation,” *The Canadian Journal of Chemical Engineering*, vol. 87, no. 5, pp. 732–740, 2009.
- [23] C. Hemmings, “The elaboration of a critical framework for understanding cancer: the cancer stem cell hypothesis,” *Pathology*, vol. 42, no. 2, pp. 105–112, 2010.
- [24] N. Chan, M. Koritzinsky, H. Zhao et al., “Chronic hypoxia decreases synthesis of homologous recombination proteins to offset chemoresistance and radioresistance,” *Cancer Research*, vol. 68, no. 2, pp. 605–614, 2008.
- [25] K. I. E. M. Wijffels, H. A. M. Marres, J. P. W. Peters, P. F. J. W. Rijken, A. J. van der Kogel, and J. H. A. M. Kaanders, “Tumour cell proliferation under hypoxic conditions in human head and neck squamous cell carcinomas,” *Oral Oncology*, vol. 44, no. 4, pp. 335–344, 2008.
- [26] B. G. Wouters and J. M. Brown, “Cells at intermediate oxygen levels can be more important than the “hypoxic fraction” in determining tumor response to fractionated radiotherapy,” *Radiation Research*, vol. 147, no. 5, pp. 541–550, 1997.

Review Article

Hypoxia in Head and Neck Cancer in Theory and Practice: A PET-Based Imaging Approach

Loredana G. Marcu,^{1,2} Wendy M. Harriss-Phillips,^{2,3} and Sanda M. Filip¹

¹ Department of Physics, Faculty of Science, University of Oradea, 410087 Oradea, Romania

² School of Chemistry and Physics, University of Adelaide, Adelaide, SA 5000, Australia

³ Department of Medical Physics, Royal Adelaide Hospital, Adelaide, SA 5000, Australia

Correspondence should be addressed to Loredana G. Marcu; loredana@marcunet.com

Received 13 June 2014; Accepted 6 August 2014; Published 21 August 2014

Academic Editor: Eva Bezak

Copyright © 2014 Loredana G. Marcu et al. This is an open access article distributed under the Creative Commons Attribution License, which permits unrestricted use, distribution, and reproduction in any medium, provided the original work is properly cited.

Hypoxia plays an important role in tumour recurrence among head and neck cancer patients. The identification and quantification of hypoxic regions are therefore an essential aspect of disease management. Several predictive assays for tumour oxygenation status have been developed in the past with varying degrees of success. To date, functional imaging techniques employing positron emission tomography (PET) have been shown to be an important tool for both pretreatment assessment and tumour response evaluation during therapy. Hypoxia-specific PET markers have been implemented in several clinics to quantify hypoxic tumour subvolumes for dose painting and personalized treatment planning and delivery. Several new radiotracers are under investigation. PET-derived functional parameters and tracer pharmacokinetics serve as valuable input data for computational models aiming at simulating or interpreting PET acquired data, for the purposes of input into treatment planning or radio/chemotherapy response prediction programs. The present paper aims to cover the current status of hypoxia imaging in head and neck cancer together with the justification for the need and the role of computer models based on PET parameters in understanding patient-specific tumour behaviour.

1. Introduction

1.1. The Challenge of Hypoxia in Head and Neck Cancer. Tumour hypoxia remains one of the major causes of treatment failure in solid cancers. Advanced head and neck carcinomas are often aggressive and commonly hypoxic, features that are associated with treatment resistance to both radio- and chemotherapy and also poor survival [1]. Additionally, there is evidence that hypoxia limits the effectiveness of surgery as well [2]. Studies undertaken on head and neck squamous cell carcinomas have concluded that the median partial oxygen pressure (pO_2) is one of the strongest independent prognostic factors of both disease-free and overall survival in these patients, regardless of treatment modality [1, 3].

Hypoxia was shown to promote angiogenesis and distant metastases [4, 5] processes that add to the challenge

of managing hypoxic solid tumours. Furthermore, a bell-shaped relation was found between the microvascular density of head and neck tumours and patient survival, meaning that both very low and very high concentrations of blood vessels are associated with poor prognosis [6]. Therefore, low oxygenation status and intensified angiogenesis are equally linked to treatment failure in head and neck cancer.

As a response to cell loss during treatment, head and neck tumour cells activate various mechanisms to trigger tumour repopulation. Similarly to tumour cells, endothelial cells, which form the lining of blood vessels, have also exhibited high activity during treatment, leading to regeneration of microvessel density [7]. The process of tumour repopulation and/or vascular regeneration in head and neck cancer during radiotherapy creates a vicious circle that is difficult to interrupt, which is the reason why these occurrences are commonly associated with treatment failure.

1.2. Hypoxia as a Promoter of Angiogenesis. Tumours need oxygen and nutrients to survive and thrive. Tumours that outgrow their own vasculature lack oxygen supplies and therefore they start creating their own vascular network to allow the oxygen transport. In fact, there is experimental evidence showing that the induction of new blood vessel formation (i.e., angiogenesis) is activated well before the tumour outgrows its vasculature [8]. Tumours exceeding the size of 1 mm^3 are reliant on blood supply from the newly created vascular network [9].

Once the angiogenic switch is turned on, new capillaries start to sprout and generate a whole new vascular network. The newly formed vessels, however, are abnormal looking and present with leaks, shunts, and blind ends, which can often be obstructed. These obstructions cause further problems, as oxygen cannot reach the cells in the affected areas. Consequently, temporary hypoxia arises which renders the cells resistant to treatment. This type of hypoxia, also known as acute hypoxia, is one of the biggest challenges in the management of malignant neoplasms as they are both spatially and temporally unstable. In other words, it is impossible to predict where, when, and for how long a specific tumour region will be hypoxic. This fact has further repercussions on treatment planning and delivery, as the hypoxic areas based on pretreatment images might not coincide with the hypoxic areas that are present during treatment.

Chronic hypoxia, on the other hand, is more predictable, as it typically occurs in the core of the tumour and the reoxygenation process befalls during fractionated radiotherapy.

1.3. Hypoxia as a Promoter of Distant Metastases. Tumour hypoxia has been shown to play an essential role in the promotion of distant metastasis [4] given that the hypoxia-inducible factor- 1α (HIF- 1α) regulates several processes along the metastatic pathway.

Head and neck cancer metastasizes predominantly to regional lymph nodes. Both large and small tumours have the capacity to metastasize given that the primary tumour expresses the gene for metastatic spread. For instance, increased gene expression levels of the glucose transporter protein Glut-1 were found to be correlated with local recurrence, regional lymph node metastases, and poor survival in patients treated for oral squamous cell carcinomas [10]. Similar results were achieved by Zhou et al. in head and neck cancer patients, indicating a strong relationship between elevated Glut-1 levels and poor prognosis [11]. However, the risk of distant metastases was shown to be lower in head and neck tumours treated with hypoxia modifiers [12].

With today's technological advances, locoregional control of several types of cancers, including head and neck, has improved. The challenge, however, remains controlling the metastatic spread and thus in the management of the systemic disease. Despite the fact that tumour metastases are the most common cause of death among cancer patients, methods to specifically target this process are scarce. Alongside hypoxia, the metabolic information supplied by PET imaging offers valuable assessment of tumour metastases. Such information

allows for further treatment planning materialized by either chemotherapy or targeted radioimmunotherapy [13, 14].

2. Common Assays for Tumour Oxygenation Status

Over the decades, several methods, including a variety of imaging modalities, have been trialled to detect hypoxia and differentiate between the acute and the chronic type, whenever possible. Hypoxic subvolumes within a tumour need adequate considerations during treatment planning and delivery; thus they need to be reliably identified. Due to large heterogeneities in tissue oxygenation and interpatient variations [15], hypoxia needs to be individually assessed for each patient for an accurate target definition and identification of hypoxic subvolumes for dose painting.

Despite all efforts to develop pretreatment assays to evaluate the association between the level of hypoxia and treatment outcome, several predictive assays failed the *in vivo* testing [40]. The main objective of predictive assays for tumour oxygenation status is to select the likelihood of benefit from the addition of hypoxic cell sensitizers, hypoxic cytotoxins, or other adjuvant therapies that would lead to an increased therapeutic ratio in hypoxic tumours. Nowadays, the importance of microvessel density assessment increases, together with the development of antiangiogenic agents and their inclusion in treatment protocols for patients who might benefit from these therapies.

Both direct and indirect methods have been developed in order to evaluate and quantify the level of oxygenation in tumours (Table 1). The most common methods involve (1) the use of polarographic electrodes, (2) immunohistochemical staining of hypoxic cells, and (3) a less invasive approach—PET imaging using hypoxia-specific radiotracers.

It has already been mentioned that microvessel density is a good predictive factor of treatment outcome in head and neck cancer [6]. The evaluation of vascular density represents an indirect method to determine tumour oxygenation and is undertaken using tumour biopsies. This technique originated in the 1960s, when Kolstad showed that tumours with long intercapillary distances (i.e., with poor vascular networks) had low oxygenation and higher probability to recur than tumours with short intercapillary distances [41]. Microvascular density measurements involve immunohistochemical techniques for counting of vessels that were previously labeled with endothelium-specific markers. One drawback of this method is the lack of information on acutely hypoxic cell populations. However, vascular density measurements offer indications regarding chronic hypoxia, demonstrating that chronically hypoxic cells significantly contribute to the overall hypoxic fraction and also influence treatment outcome.

One of the most widely used tools for tumour oxygenation measurements (oxygen tension or pO_2) is the polarographic oxygen electrode. The principle of this technique is based on the polarographic reduction of molecular oxygen at a platinum electrode, which creates an electric current. The magnitude of the current depends on the oxygen quantities

TABLE 1: Techniques for tumour hypoxia evaluation/measurement.

Technique	Characteristics
Polarographic electrode (Eppendorf oxygen electrode)	Direct and invasive technique involving a fine-needle electrode (cathode) for tumour hypoxia measurement. The current between the cathode and the reference electrode is directly proportional to tissue pO_2 .
Cryospectrophotometry	Indirect, histomorphometric assay of oxygen levels in tumour vasculature assessed on frozen tissue samples.
Microvessel density (angiogenesis assessment)	Indirect way to assess hypoxia using immunohistochemical techniques for counting blood vessels that were previously labeled with endothelium-specific markers.
DNA strand break assay (comet assay)	Indirect way to assess tumour hypoxia through DNA strand breaks after radiation exposure and fluorescent staining, based on the fact that oxic cells get more damage than hypoxic cells. The DNA fragments detached from the nucleus resemble the tail of a comet.
Endogenous hypoxia markers	Indirect method to evaluate the hypoxic fraction in tumours. Hypoxia inducible factor (HIF)-1 alpha, glucose transporter 1 (GLUT 1), and carbonic anhydrase 9 (CA 9) have been identified as proteins, which under hypoxic exposure induce the transcription of several genes.
Exogenous hypoxia markers	Indirect method to evaluate tumour hypoxia (using biopsies). Exogenous markers are nitroaromatic compounds (pimo-, miso-, eta-nidazole) which selectively bind to hypoxic cells.
Oximetry with electron paramagnetic resonance	Noninvasive and direct method to quantify pO_2 in tissue using stable nitroxides that interact with molecular oxygen.
Blood oxygen level-dependent magnetic resonance imaging (BOLD MRI)	Noninvasive method for evaluation of hypoxia through correlation of BOLD signals with pO_2 .
Positron emission tomography	Noninvasive and direct method to evaluate hypoxia via injection of hypoxia-specific radiotracers.

that reach the electrode. The oxygen electrode that is currently used in labs is manufactured by Eppendorf-Netheler-Hinz GmbH, Hamburg, Germany. Due to its good correlation with the clinical outcome, the Eppendorf electrode is still considered the gold standard in determining the oxygen tension [42].

One advantage of this technique is that allows quantitative assessment of oxygen distribution levels within the tumour, without, however, distinguishing between necrotic and viable cancerous tissues. A main drawback is linked to the invasive approach, which limits the technique to superficial tumours only.

Functional imaging techniques, besides having other advantages, are noninvasive methods for the assessment of tumour metabolism and of various tumour-related kinetic parameters. Nowadays, tumour hypoxia is successfully evaluated using such imaging techniques. Positron emission tomography (PET) and blood oxygen level-dependent magnetic resonance imaging (BOLD MRI) are two diagnostic imaging methods widely used for oncologic investigations. These two robust techniques are characterized by ease of use and reliability and are able to assess the heterogeneous distribution of oxygen with the tumour [43].

BOLD MRI uses paramagnetic deoxyhaemoglobin as contrast agent (to target red blood cells), which makes the method sensitive to pO_2 in blood vessels and also in the neighbouring tissues. However, the technique does not allow direct measurement of tissue pO_2 . There are various studies looking into the relationship between pO_2 and BOLD

signal changes to find a reliable correlation between these parameters [44, 45]. Given that in acute hypoxia the poorly oxygenated regions extend up to the vasculature, BOLD MRI seems to be a more sensitive measure of oxygen levels for perfusion-related hypoxia than for diffusion-dependent or chronic hypoxia. Due to the large distance between chronically hypoxic areas and the red blood cells from existing tumour vessels, BOLD MRI cannot reflect the status of chronically hypoxic tumour regions [43]. While this MRI technique does not provide a quantitative measure of pO_2 , there is experimental evidence showing an association between variations in tumour oxygenation and changes in BOLD signals (spin lattice relaxation rate) [44].

Of all the currently existing techniques for *in vivo* detection of hypoxia, positron emission tomography is the best validated and the most used clinical method. PET is a noninvasive, functional imaging technique, which measures the *in vivo* distribution of radiolabelled isotopes, after the injection of a radioactive contrast material. For hypoxia imaging, PET uses hypoxia-specific radioisotopes which together with ^{18}F -FDG (fluorodeoxyglucose) offer a complex picture of the tumour.

3. The Role of PET in Hypoxia Imaging of Head and Neck Cancer

PET imaging is a valuable tool in assessing oxygenation levels in tumours for the purpose of treatment planning and also as a prognostic indicator. It was shown that the information

TABLE 2: Trials involving hypoxia-specific PET imaging in head and neck cancer over the last 10 years.

Radiotracer	Reference	Trial and aim	Results
¹⁸ F-MISO	Rischin et al. 2006 [16]	<i>TROG randomized trial (45 patients)</i> To determine the association between tumour hypoxia, treatment regimen, and locoregional failure in advanced HNC	¹⁸ F-MISO-detected hypoxia is associated with high locoregional failure in patients not receiving tirapazamine.
	Kikuchi et al. 2011 [17]	<i>Clinical study (17 patients)</i> To evaluate the role of ¹⁸ F-MISO as a predictor of treatment outcome in HNC	Local control after radiotherapy was significantly lower in patients with high uptake than in those with low tracer uptake. Pretreatment scan with ¹⁸ F-MISO may predict treatment outcome.
¹⁸ F-FAZA	Souvatzoglou et al. 2007 [18]	<i>Phase I trial (11 patients)</i> Feasibility of ¹⁸ F-FAZA for hypoxia imaging in HNC patients	Feasible for clinical use and offers adequate image quality for hypoxia assessment.
	Postema et al. 2009 [19]	<i>Phase I trial (9 HNC patients out of 50 overall cancer patients)</i> To demonstrate the safety and biodistribution pattern of ¹⁸ F-FAZA in patients with HNC, lung cancer, gliomas, and lymphomas	Clear uptake of ¹⁸ F-FAZA was observed in 6 out of 9 HNC patients; good imaging properties; good tumour-to-blood ratio. Promising agent for hypoxia imaging in HNC.
¹⁸ F-EF3	Mahy et al. 2008 [20]	<i>Phase I trial (10 patients)</i> To assess the pharmacokinetics, biodistribution, and metabolism (324 MBq versus 1,134 MBq)	Uptake and retention in tumour was observed; no difference between the radioactivity groups; no side effects; safe and feasible.
¹⁸ F-EF5	Komar et al. 2008 [21]	<i>Phase I trial (15 patients)</i> To determine the optimal PET protocol for ¹⁸ F-EF5 as a hypoxia imaging agent	Initial ¹⁸ F-EF5 uptake is governed by blood flow; later phase uptake is hypoxia specific (optimal detection time is 3 h after injection); warranting more study.
¹⁸ F-HX4	Chen et al. 2012 [22]	<i>Phase I trial (12 patients)</i> To evaluate the feasibility of HX4 compared with ¹⁸ F-MISO	HX4 possibly has higher sensitivity and specificity and shorter injection-acquisition time (1.5 h) than ¹⁸ F-MISO
Cu-ATSM	Minagawa et al. 2011 [23]	<i>Phase I/II trial (17 patients)</i> To evaluate the relationship between ⁶² Cu-ATSM tumour uptake and chemoradiotherapy	⁶² Cu-ATSM SUV _{max} greatly differed between patients with and without residual disease. ⁶² Cu-ATSM could be a predictor of tumour response to treatment.
	Grassi et al. 2014 [24]	<i>Preliminary prospective study (11 patients)</i> To assess the efficacy of pretreatment ⁶⁴ Cu-ATSM as a prognostic factor and its role as a marker of disease progression	⁶⁴ Cu-ATSM showed high sensitivity but low specificity in predicting response to chemoradiotherapy. There were no differences between early and late scans.

HNC: head and neck cancer.

provided by PET/CT during therapy leads to changes in treatment management in up to 40% of the cases [46].

To date, there are several hypoxia-specific PET radioisotopes in clinical use or under trial (Table 2). The feasibility and clinical adequacy of new radiolabelled isotopes are assessed by means of (1) tumour uptake and retention, (2) metabolic information supplied, and (3) patient safety. While several radioisotopes fulfill the clinical criteria as PET radiotracers, there is need for more comprehensive trials in order to distinguish in a qualitative manner between the various compounds currently used.

One category of hypoxia-specific radioisotopes is the group of radiolabelled nitroimidazole given that nitroimidazoles are known to bind selectively to hypoxic cells where they are reduced [47]. The first labeled nitroimidazole compound developed for PET detection was ¹⁸F-MISO ([¹⁸F] fluoromisonidazole) [48]. Pretreatment ¹⁸F-MISO uptake has been shown to be an independent prognostic indicator following treatment of head and neck cancer (high FMISO uptakes correspond to low tissue oxygen concentrations, which usually are indicative of poor response to treatment) [49]. A comparative study aiming at assessing tumour

hypoxia in 38 head and neck cancer patients has been undertaken by Gagel et al. [50] using the polarographic electrode versus PET imaging with ^{18}F -MISO combined with ^{18}F -FDG. The group concluded that the noninvasive PET technique is valid and represents a feasible *in vivo* method for determining clinically relevant hypoxia, despite some of its limitations (such as limited spatial resolution of PET which can be a challenge when imaging small tumours).

Beside the quantitative evaluation of hypoxia-specific radiotracers, there are studies investigating the reproducibility of the tracer's uptake in the assessment of hypoxia. A study undertaken by Okamoto et al. [51] involved eleven head and neck cancer patients twice scanned with ^{18}F -MISO within a 48 h interval. The difference between the two maximum standardized uptake values was 7% while the difference between the two tumour-to-blood ratios was 9.9%. The study demonstrated the reliability and reproducibility of ^{18}F -MISO in regard to tumour hypoxia in head and neck carcinomas.

Another radiotracer that has been intensively studied in relation to hypoxia is ^{18}F -FAZA (fluoroazomycin-araboside). A comparative study between ^{18}F -FAZA and ^{18}F -MISO undertaken on rat tumours has shown only minor advantages of the former, consisting of higher tumour to background and tumour-to-blood ratios due to more rapid clearance from blood and nontarget tissues [52].

More lipophilic fluorine-based radiotracers have also been investigated (^{18}F -EF3, ^{18}F -EF5); however clinical findings have shown similar results to those obtained with ^{18}F -MISO. One of the newer hypoxia-specific PET agents is ^{18}F -HX4 (2-nitroimidazole nucleoside analogue), which was shown to have better water solubility and faster clearance than the well-established tracers, presenting also a strong dependence on tumour hypoxia [53].

Next to fluorine, copper-based radiotracers play an important role in PET imaging of hypoxic tumour regions. Lewis et al. have published the first report on the oxygen-dependent uptake of Cu-ATSM both *in vitro* and *in vivo*, showing that hypoxic cells present with a threefold higher uptake compared to normally oxygenated cells [54].

While ^{18}F -FDG is not particularly useful for the assessment of hypoxia with static PET imaging, dynamic PET offers valuable quantitative information on blood perfusion and also drug pharmacokinetics, which represents an indirect evaluation of vascular density and functionality [55].

Nevertheless, Mullani et al. [56] have shown that tumour blood flow measurements can be undertaken from the first pass of ^{18}F -FDG through the tumour using a simple scan. This idea is supported by the fact that the initial large influx of the radiotracer into tissue during the first pass is delivered as a function of the blood flow to the respective tissue [55].

While more expertise is needed for dynamic PET image acquisition and interpretation, the advantage of this approach is the possibility of following over time the radiotracer's metabolism in the region of interest. This allows for a better differentiation among metabolically dissimilar areas, including differently oxygenated regions. Furthermore, dynamic

PET with ^{18}F -FDG gives indications not only on metabolic changes but also on vascular alterations during fractionated radiotherapy [57].

It is probably safe to suggest that all radiolabelled compounds trialed so far are valuable instruments, which assist the clinicians to decide on the most favorable subsequent treatment, thus bringing the individualized treatment planning one step closer to clinical implementation worldwide. Developing clinically robust tools for tumour hypoxia assessment would allow clinicians to choose treatment based on an individualized, scientific foundation and select those patients that would benefit from adjuvant therapies in order to sensitize the tumour to radiation. As stated by Isa et al. in a review paper published in 2006 [2]: "*there is an unmet need for biological parameters to individualize treatments.*" Several years later, while we have a larger pool of markers and biological targets available, the above statement remains valid.

4. Models of Hypoxia Based on PET-Imaging

Computational modelling of PET tracer dynamics is a crucial step in understanding complex individualised data acquired during PET imaging. Combined PET/CT image sets provide functional as well as spatial data from tissue regions that are, for example, highly metabolically active or relatively low in oxygen, depending on the specific radioactive tracer (or label) used. Only through the use of sophisticated models can we begin to quantitatively analyse PET tracer pharmacokinetics (PK) within *in vivo* tumours or normal tissues.

Motivation for this understanding stems from the desire of clinicians and radiobiologists to utilise specific PET data to predict tumour behaviour and responses to different treatment options, such as fractionated radiotherapy. This utilisation often requires development of further complex computational models that can read in the PET data and then apply cell line or tumour specific kinetic processes and tumour/vessel architecture to simulate proliferation and treatment induced cell death.

An initial step in interpreting and utilising complex PET data is to develop a computational model, with the aims of setting parameters with realistic values (through comparison with reported biological values) and eventually the generation of a complete virtual PET image. By these means, parameters, such as drug uptake, diffusion, and binding rates for a specific tracer, can be analysed in a model sensitivity study, with multiple-parameter solutions and associated stochastic uncertainties generated, using the real PET data as a baseline for comparison. However, model parameter values may also be patient dependent and at present the field of tracer modelling is still to reach a consensus on optimal average population values and their uncertainties.

To be case specific, the model cannot be purely based on a first principles approach using simple geometry; it requires information to spatially place important structures such as blood vessels so that the compound of interest can be accurately simulated in the blood stream and into the target tissue. This step can add imaging modality related uncertainties or

other uncertainties if the data is estimated, for example, from the average vascular densities and diameters from tumour xenografts.

Two streams of reports exist on the topic of PET tracer modelling.

- (1) Modelling of specific tracer/oxygen dynamics—with the aim of simulating PET images with results that are in close agreement with real PET images [26, 58].
- (2) Utilisation of PET data within a separate tumour model—with the aim of making the tumour model more specific and predictive of response to treatment [33–35].

The subsections below are separated into the aforementioned categories, which exist due to the specific aims of the authors in either studying PET pharmacokinetics (with a strong emphasis on tumour oxygenation related tracers) or input and interpretation of voxelized PET data into computational tumour response models. Models in these two categories may utilise stochastic and/or analytical methods. The former may have final objectives of optimising PET injection and imaging sequencing protocols or investigation of the impact of acute versus chronic hypoxia on tracer uptake [26, 58], while the latter may have final aims which vary due to the treatment modality considered. However will generally have final objectives related to predicting if treatment response is enhanced with modified treatment regimes, compared to the current standard of care. In this review, the latter topic is discussed in terms of the input of specific patient PET information into cellular-scale models of tumour proliferation and radiotherapy response [33–35].

4.1. Modelling PET Pharmacokinetics (PK). Modelling of the transport of drug molecules through tissue, or “pharmacokinetics,” applied to the field of PET radioactive tracers, has been studied for a number of decades. For the modelling of tracers that preferentially reduce and bind in the presence hypoxia or anoxia (i.e., a lack of or no presence of oxygenation), early 2- and 3-compartmental analytical model work was published from approximately the mid-nineteen seventies and into the first years of the twenty-first century [59–61].

Compartmental modelling in this respect refers to the spatial location (it’s “state” may also be specified) of the tracer as it moves through tissue after injection; that is, the tracer could exist: (1) in a free state within vessels (within blood plasma), (2) in the interstitial space, or (3) in the intracellular space, (i) a free or (ii) a bound (reduced/phosphorylated) state. Note that the 2-compartment models neglect the second step. The tracer may be modelled to move from (1) to (2) via diffusion and/or interstitial fluid convection, while movement from (2) to (3) requires active transport, facilitated diffusion, and/or passive diffusion [25, 28].

Tabulated above is a selection of recent reports, where modelling groups have aimed to predict and better understand PET imaging data for specific tracers (Table 3). These groups may have also performed simultaneous histological or secondary imaging tests to compare with their primary PET

data set and model results, to validate the placement of well vascularised, proliferative, or hypoxic tumour subvolumes [25, 28, 29]. Secondary imaging has in some cases also enabled realistic (and specific for the tissue being studied) vessel maps to be incorporated into models for particular tumour cell lines [30]. This allows the tracer and also oxygen transport to be simulated in as close a manner (spatially) as possible to the real situation. In general, model predictions may be in the form of 2-dimensional virtual PET images which can be compared to real PET images, or in the form of parametric solutions for the mathematical model utilised, that is, the best fit and statistical analysis of all compartment model coefficients/ parameters.

To summarise the contents of Table 3, analytical compartment model work has been extended in recent years to specific and relevant PET tracer molecules, with statistical analysis of the best fit of the model parameters being found to be in good agreement with biological interpretation of the parameters (e.g., the diffusion rate constant of the tracer through capillary walls) and with the generated virtual PET images correlating well with patient and animal model PET image sets. These models show that due to the dynamic action of the tracer molecules, multiple or dynamic PET sequences are required to best interpret PET data (e.g., to assess hypoxic tumour regions). Early scans tend to indicate blood vessel tracer presence, whereas later scans are required to gain information about the desired more “final” end points of these tracers in the target cells. However, specific tracer PK information is vital. Modellers as well as clinical PET researchers may have analysed their results using different terms, commonly, time-activity-curves [25], standard uptake value (SUV) with the mean or maximum values analysed for each voxel [17], or tumour-muscle (TMR) or tumour-blood (TBR) signal ratios [62]. The latter method normalizes results for each individual to base-line levels within their own normal tissue.

Problems in the comparison of virtual PET results with real data inevitably arise due to noise in the images and the absence of tracer in tissue regions in which the tracer has difficulty in reaching, for example, very hypoxic/necrotic tissue. As a consequence, the functions of tracer concentration (at any time point) required in models are not likely to correspond linearly with tissue oxygenation. Rather, the highest signal is likely to emanate from regions of low to moderate hypoxia, where transport and binding probability of the tracer is the highest compared to very low oxygenated regions where binding is possible but vessel integrity and density is insufficient. The PET tracer utilised may also have multiple biological pathways and reactions; for example, Cu^{64} [ATSM] has been shown to correlate well with hypoxic tumour data due to its electrochemical properties, however “. . .the precise mechanism of Cu-ATSM accumulation remains largely unknown, as Cu-ATSM accumulation occurs under normoxic conditions and is strongly influenced by genetic characteristics that are independent of $p\text{O}_2$ status” [29].

Common assumptions made in PK and O_2 diffusion models due to limitations of complexity, time, computing power, and available parametric data include the following.

TABLE 3: Models from the literature that simulate the pharmacokinetics (PK) of PET tracers to predict and analyse PET scan images.

Reference	Modelling Methods	Details and Outcomes
(Kelly and Brady 2006) [25]	2-compartment F^{18} [MISO] PK model with reversible binding, with transport via diffusion only. 2-dimensional analytical spatiotemporal model.	Michaelis-Menten techniques were used to model the conservation of O_2 and cap consumption in oxidic tissue (pO_2 dependent equation). Randomly angled/oriented vessels, temporal dynamics modelled by changing vessel pressure and hence flow. Hypoxic tissue: gradual increase in activity then an accumulation curve. Oxidic tissue: activity follows plasma levels then accumulation curve seen at later stages. Late slope of TAC curve indicated hypoxia while the beginning represented local vascular supply. Results compared to pimonidazole stained tumour sections from clinical colorectal cancer data.
(Wang et al. 2009) [26]	Iterative stochastic optimisation algorithm to delineate acute and chronic hypoxia in sequential F^{18} [MISO] and FDG PET in 2-dimensional image maps, with comparisons to HNSCC clinical data.	Simulated images (known hypoxic regions) as well as sequential PET Data from 14 male HNSCC patients analysed assuming chronic (Gaussian histogram of number of voxels versus SUV) hypoxia remained constant while acute hypoxia (Poisson histogram) was varied. Normalisation methods forced the volume of hypoxia to be the same in both time-point scans; however the location of acute hypoxia varied. Image registration and resolution issues are discussed. Model predicted Gaussian chronic hypoxia distributions well in the generated images ($r^2 = 0.93$). Good fit found (13/14 cases), with acute hypoxia described well by a Poisson curve (11/14 cases) with an average of 34% (acute hypoxic volume). Suggested a third scan to increase temporal hypoxia information. 4 mm PET pixel size issue accounted for using power law distribution of chronic versus acute hypoxia within each pixel.
(Bartlett et al. 2012) [27]	Two varieties of 2-compartment, 3-rate-constant models applied to F^{18} [MISO] PET images of human prostate tumour xenografts in rats.	One model constrained kinetic parameters k_1 and k_2 to be equal while the other did not. Intratumoural pO_2 was assessed using a robotic driven probe in tumour versus plasma regions of the animal's tumour mass. Pimonidazole and perfusion Hoechst 33342 staining also analysed. Kinetic voxelised modelling (of parameter k_3) identified hypoxia with greater accuracy than tumour-to-plasma ratios. Constraining k_1 to equal k_2 during fitting was effective in controlling noise in the trapping rate constant, k_3 , without introducing bias. No obvious pO_2 cutoff for isolating hypoxic and nonhypoxic volumes (3.4 mm Hg applied) however noise of approx. 0.7 mm Hg in measurement technique.
(Gu et al. 2012) [28]	3-compartment F^{18} [FLT] PK model (3 rate constants) applied to a separate GBM growth model utilising spatial MR data and considering invasion, hypoxia, necrosis, and angiogenesis.	Voxels assigned "cell density" values with hypoxic versus oxidic percentages (e.g., 70 versus 30%) generated. Model simulated the dynamic clinical-scale imaging process in terms of noise and reconstruction uncertainties of PET. Clinical GBM patient data used for comparison, with patient specific virtual PET scans generated with no statistical difference to real hypoxic tumour image sets. Model could predict and distinguish hypoxic cell hyperactivity versus hyperdensity on the PET image.
(McCall et al. 2012) [29]	TACs derived from mean tissue activity concentration functions for Cu^{64} [ATSM] (Ct) in HNSCC and muscle and compared to venous input functions (Cp).	Tracer dynamics studied in HNSCC (FaDu) xenografts in rats and analytical parameters of the model fitted to generated results matching real PET data. Influx-constants (K_i) calculated by analysis of Patlak plots of Ct/Cp ratios versus normalized time integrals of Cp. PET mean data analysed from 1 min up to 18 hours after injection. Distribution volumes (V_d) calculated. High tumour to muscle uptake ratios found (4:1 tumour to muscle ratio at 20 min). No Cu^{64} [ATSM] correlation to pimonidazole hypoxia staining (early or late). Cu dynamics are not only pO_2 dependent, more study recommended. Early uptake of tracer in tumour at 1 min found followed by slower but steady increase, while muscle signal increased quickly then plateaued. Wash out rates in tumour and normal tissue difficult to define.

TABLE 3: Continued.

Reference	Modelling Methods	Details and Outcomes
(Monnich et al. 2013 [30], Mönlich et al. 2011) [31]	O ₂ kinetic and F ¹⁸ [MISO] tracer PK model simulating 2-dimensional virtual PET maps, based on blood vessel maps from human HNSCC xenografts stained for endothelial structures	Xenografts were utilised to derive 2D vessel maps (~3% vascular fraction) and an explicit pO ₂ -dependent binding rate, $K(P)$. Oxygen and tracer flux across vessel walls, J_T , assumed proportional to the concentration differences on the intra- and extravascular side. Tracer moved via diffusion. Irreversible binding rate modelled as dependent on pO ₂ only. Nonlinear Michaelis-Menten oxygen consumption versus pO ₂ tension. Individual time-point data did not show correlation with real data (2.5 mm Hg threshold for each voxel with median pO ₂ in each voxel assessed); however, ratios of 0–15 min versus 4-hour data had significant outcomes. Four-hour data did correlate but not as well as ratio data. From 2011: binding versus pO ₂ function described with steep initial increase (<0.5 mm Hg). Simulated local TACs share characteristics with clinical PET TACs hence it may be possible to measure perfusion from early dynamic PET. Alternative tracer dynamics (faster clearance) also simulated with earlier time point PET scans predicted optimum, although free-tracer signals limit earlier time feasibility.
(Liu et al. 2014) [32]	F ¹⁸ [FLT] 2- and 3-compartment PK models compared for HNSCC clinical PET images, incorporating diffusion as well as convection transport of the tracer.	A comprehensive statistical analysis of the PK model is reported. “EM-BIC” clustering methodology described, and model used to analyse raw PET images and reduce noise and hence uncertainty in the rate constant parameters derived. Model results compared to 10 × 1-hour dynamic HNSCC clinical PET data sets, with the 3-compartment (6 rate constants) “3C6K” model best fitted patient data.

[TAC: time activity curve; HNSCC: head and neck squamous cell carcinoma; GBM: glioblastoma multiforme; PK: pharmacokinetic; pO₂: partial pressure of oxygen; SUV: standard uptake value].

- (1) Homogeneous cellular density, diffusion, and consumption coefficients, which is not the case in a heterogeneous tumour.
- (2) The use of static histological data used to generate vessel maps and hence the assigning of O₂ in 2- or 3-dimensional maps does not reflect acute hypoxic dynamics, which can be overcome by specifically modelling O₂ kinetics [30] with realistic temporal fluctuations in O₂ supply and realistic cellular O₂ consumption [28].
- (3) The lack of machine specific corrections (dead time, decay rate, noise, scatter, attenuation correction, and time-of-flight) and reconstruction related random and systematic uncertainties, considered however by some groups [28, 33] and specifically investigated in terms of attenuation correction based on X-ray CT data [63] or segmentation of emission images and in terms of partial volume effects [64].

Neglected in Table 3 are reports from authors addressing oxygen and/or tracer dynamics using multimodality imaging techniques without a “modelling” approach (see Section 3). These reports can add valuable data in terms of correlations between anatomy, tracer, and oxygenation in space and time, for example, the work of Cho et al., who have combined PET (F¹⁸[MISO]), MR, H&E, pimonidazole, and F¹⁸ autoradiography techniques in a prostate xenograft tumour model to analyse necrosis, hypoxia, and well perfused tissue and to confirm the validity of the different imaging modalities

in identifying these tumour subvolumes [37]. Cho et al. [37] found that combined hypoxia and perfusion data could predict outcome but could neither alone correlate well with regions of perfused tissue (as indicated by early PET uptake).

4.2. Utilisation of PET Data in Treatment Response Models.

As the previous section has shown, there are many factors that influence final PET image voxel intensities. These factors reduce down to being related to both tracer pharmacokinetics and specificity or machine intrinsic spatial resolution limits. When desiring to take this data and use it for input into computational tumour models, these factors must also be of paramount concern. The tumour model, if at the cellular-scale, will require a suitable scaling paradigm to convert data at the mm scale down to an approximate 10–50 μm scale and also method of converting the PET signal intensity assigned to each tumour voxel or “cell” into an actual parameter value, such as pO₂ if, for example, oxygenation data has been the intention of the PET scan.

Stochastic methods utilising probability distributions may be useful for both of these tasks. Models capable of simulating tumours at the cellular level with real tumour-like proportions are challenging, hence limited number of papers reviewed. This topic is however at a stage of expansion and it is foreseen that more groups will report of their modelling experiences in the field of PET data tumour response modelling within the present decade. This will be aided by not only computing power increases, but also the demand by clinicians and the public to use currently,

TABLE 4: Stochastic tumour models utilising PET oxygenation data to predict the efficacy of nonstandard treatment solutions.

Reference	Modelling methods	Details and outcomes
(Toma-Daşu et al. 2009) [33]	F^{18} [MISO] and Cu[ATSM] distribution functions modelled in a 10^8 cell tumour growth and O_2 transport model followed by uniform or central boost RT.	Tracer binding versus pO_2 functions used (higher uptake at intermediate O_2 for Cu) to generate tracer uptake maps for each tracer on a 2D slice of heterogeneous spherical tumour. Convolution function used to describe finite resolution of the imaging modality. Local temporal changes in cellular O_2 accounted for. Virtual image maps generated to predict LQ survival and Poisson tumour control using 2 different circular dose distributions with central boost doses. Redistribution of dose (same integral dose but hotter in the centre) was possible for each tracer without decreasing the target tumour control (90%).
(Titz and Jeraj 2008, Titz et al. 2012) [34, 35]	Simulating effects of antiangiogenic treatment using F^{18} [FDG], F^{18} [FLT] and Cu 61 [ATSM] PET data in a tumour proliferation and therapy model (2008—where RT is modelled as the treatment modality) with an added vascular and PET/drug PK/PD component (open 2-compartment) (2012).	<i>BvMb</i> plasma concentration-time-profiles $cbev(t)$ utilised, with model parameters adapted to population-based values (e.g., MVD to determine <i>BvMb</i> PD). A linear relationship between VEGF expression and endothelial cell (EC) proliferation used. Nonnormal distributions manipulated the raw data O_2 PET data (~4 mm pixels) for cellular level input to generate 2D oxygenation maps considering multiple diameters and angles of the vessels. 8 HNSCC PET scans used (phase 1 trial data), before and after RT for input and comparison to model predictions. A decrease in SUVs (i.e., reduction in vasculature) after <i>BvMb</i> agreed with follow-up PET. Increase in hypoxia due to <i>BvMb</i> observed, peaking at week 2 after treatment, but decreasing with increasing baseline levels of hypoxia and increasing CCT. Due to pO_2 and proliferation interdynamics, simulations could provide estimates of optimal drug administration times (i.e., every 2 or 3 weeks). Expansion planned for the use of voxel-based kinetic parameters to model drug uptake more precisely and vessel “remodelling” in response drugs.

[PD: pharmacodynamic; CCT: cell cycle time; BvMb: bevacizumab].

or soon-to-be, available individualised PET data for specific (not only region of interest contouring) purposes during treatment planning.

Two reports from stochastic tumour modelling groups are summarised in Table 4. These groups have developed models of varying complexities, including treatment response modelling, with discussions about how the previously presented limitations and issues have been considered.

To expand upon the work that has been performed to estimate modified treatment responses, Table 5 has been included to further highlight efforts that have been made to consider tumour model predictions within clinical radiotherapy treatment planning systems (TPS) dose distributions, where the plan has either been delivered to real patients or the distributions analysed for their feasibility in terms of deliverability and toxicity.

A thorough overview of the process of gaining information from PET/CT and using it to optimise pre- and midtherapy planning processes was published in 2013 [65]. The authors concentrate on how hypoxia related information can be obtained and used in the planning process, from interpretation of PET data to final planning and prescriptions for radiotherapy. Dose painting (DP) methods, for example, methods to “redistribute dose” to the most radioresistant HTVs or escalating/boosting the dose to HTVs above the standard uniform dose prescription, are discussed along with

many of the current challenges that require more research and validation. Indeed, modern IMRT techniques are confirmed here as being capable of delivering complex nonuniform dose gradients with a resolution similar to that of PET images which could in theory deliver a gradient of prescription doses to subvolumes with different severities of oxygen deprivation.

Geets et al. remind us of the difficulties faced in implementation arising not only from intrinsic noise, blur, and partial volume effects in PET data, but also in the use of a suitable tracer that is specific and can reach the hypoxic tumour environment (i.e., low probability of being bound/reduced due to other microenvironmental factors such as low pH) and the use of suitable scan time protocols. References are provided from groups reporting workable solutions to uncertainties arising due to the image acquisition itself; however, as the reports in Table 3 confirm, the latter issues may not be easily overcome without future tracer specificity research and scanning at multiple time points after injection. F^{18} [FAZA] is mentioned as showing promise as good hypoxia tracer; however all tracers did [65] and continue to have issues, with no compound standing out as superior.

This report also discusses the issues of converting oxygenation information into radioresistance estimates and hence prescription requirements, in order to achieve increased tumour control. These are nontrivial challenges, as both functions of converting pO_2 to cell death probably,

TABLE 5: Application of model predictions to clinical radiotherapy dose distributions to increase tumour control in hypoxic tumours.

Reference	Treatment/Model Methods	Details and Outcomes
(Thorwarth and Alber 2008) [36]	F^{18} [MISO] PET/CT performed on 15 HNC patients, with mid-RT scan after 20 Gy and with total dose of 70 Gy. DP strategies investigated.	Hypoxia and well as perfusion parameters combined could predict for RT outcomes, but neither alone (similar to study by Cho et al. 2009) [37] Model was calibrated using hypoxia and perfusion outcomes from this patient set and was designed to be used to predict optimal dose escalation factors to radioresistant HTVs. DP found feasible without increased toxicity to normal tissues.
(Choi et al. 2010) [38]	IMRT dose escalation to the HTV (from 2.4 to 2.6–3.6 Gy/30 fractions) planned for 8 HNSCC patients after F^{18} [MISO] PET/CT (4 hours post injection). ECLIPSE TPS and 6 MV X-rays beams utilised.	Tumour/cerebellum activity ratio of 1.3 used as a cut-off value for HTV definitions. Dose escalation to at least 2.6 Gy to the HTV found feasible for 6/8 patients, where the HTV received a total of 78 Gy, without increasing normal tissue doses.
(Toma-Dasu et al. 2012) [39]	IMRT optimisation performed using a research TPS to plan dose distributions for various scenarios of HTV evolution during RT. Data from 7 HNSCC patients after F^{18} [MISO] PET/CT (120–160 min post injection) applied. HTV aim (dynamic pO_2 case) of increasing dose from 60 to 77 Gy.	PET signal to uptake (and hence pO_2 and then radiosensitivity) data conversion used a maximal pO_2 level of 60 mm Hg and analytical formula. Model provides an objective method to set minimum doses to hypoxic regions to counteract increased radioresistance in individual tumours, without comprising tumour control, that is no decreasing non-hypoxic volume doses below current clinical doses.

[DP: Dose Painting; HTV: Hypoxic Target Volume; IMRT: Intensity Modulated Radiotherapy; TPS: Treatment Planning System; RT: Radiotherapy].

that is, radiosensitivity, or cell death to tumour control are nonlinear and dependent on patient specific parameters. The authors remind us that chronic hypoxia remains the focus of the discussed techniques, as opposed to acute/transient hypoxia which may alter in oxygenation faster than the time a PET scan can be acquired and analysed (or radiotherapy planned/delivered). Logistical noteworthy challenges are discussed, for example, the set-up accuracies required, volume expansion protocols for adding margins onto regions of interest nonuniform dose prescription, and how often to rescan during therapy to balance workload of scanning and replanning with the timing of substantial biological change and hence improvement in therapeutic ratio if the plan is altered.

5. Conclusions

Tumour hypoxia remains one of the major causes of treatment failure in head and neck cancer. By promoting angiogenesis as well as distant metastases, hypoxia becomes an important treatment target. In order to increase the therapeutic ratio it is crucial to identify and to quantify the hypoxic subvolumes. To date, PET-based molecular imaging is the most commonly employed technique applied for this purpose.

The use of computational models for treatment assessment and prediction is fast growing. Whether simulated or actual PET data has been applied to a tumour response model, overall the current literature suggests that targeting radioresistant hypoxic tumour subvolumes using complex dose gradients or even simpler boost doses is feasible using modern radiotherapy techniques. Research has also shown that toxicity need not be compromised if careful planning is performed, with a possible solution being not to increase

the integral dose but rather decrease the prescription to well oxygenated regions and increase it to chronically hypoxic areas. This is still to be confirmed in randomised clinical trials.

As it stands currently, all the signs point to hypoxia dose painting as being feasible to tackle notoriously hypoxic tumours, such as head and neck carcinomas. To further improve, the field moves into requiring individual tracer pharmacokinetic information/analysis so that PET data can be accurately interpreted and then utilised appropriately to predict optimal treatment plans and overall outcome improvement.

Health institutions will need to encourage and support multidisciplinary research and prioritize resources to make the use of functional PET information feasible, as assessing the dynamic changes of the tumour characteristics at a number of time points after PET injections and then at multiple intervals throughout radiotherapy will always inevitably be highly resource intensive. This will be especially true during the learning phase as this technique is translated from research into the routine clinical environment. Computational pharmacokinetics and tumour models will be vital in this translation process.

Conflict of Interests

The authors declare that there is no conflict of interests regarding the publication of this paper.

Acknowledgment

Loredana G. Marcu and Sanda M. Filip would like to acknowledge the support offered by a grant of the Ministry

of National Education, CNCS-UEFISCDI, Project no. PN-II-ID-PCE-2012-4-0067.

References

- [1] M. Nordmark, S. M. Bentzen, V. Rudat et al., “Prognostic value of tumor oxygenation in 397 head and neck tumors after primary radiation therapy. An international multi-center study,” *Radiotherapy and Oncology*, vol. 77, no. 1, pp. 18–24, 2005.
- [2] A. Y. Isa, T. H. Ward, C. M. L. West, N. J. Slevin, and J. J. Homer, “Hypoxia in head and neck cancer,” *British Journal of Radiology*, vol. 79, no. 946, pp. 791–798, 2006.
- [3] P. Stadler, A. Becker, H. J. Feldmann et al., “Influence of the hypoxic subvolume on the survival of patients with head and neck cancer,” *International Journal of Radiation Oncology, Biology, Physics*, vol. 44, no. 4, pp. 749–754, 1999.
- [4] G. U. Dachs and G. M. Tozer, “Hypoxia modulated gene expression: angiogenesis, metastasis and therapeutic exploitation,” *European Journal of Cancer*, vol. 36, no. 13, pp. 1649–1660, 2000.
- [5] A. Facciabene, X. Peng, I. S. Hagemann et al., “Tumour hypoxia promotes tolerance and angiogenesis via CCL28 and T_{reg} cells,” *Nature*, vol. 475, no. 7355, pp. 226–230, 2011.
- [6] M. I. Koukourakis, A. Giatromanolaki, E. Sivridis, and I. Fezoulidis, “Cancer vascularization: implications in radiotherapy?” *International Journal of Radiation Oncology Biology Physics*, vol. 48, no. 2, pp. 545–553, 2000.
- [7] M. I. Koukourakis, A. Giatromanolaki, E. Sivridis et al., “Squamous cell head and neck cancer: evidence of angiogenic regeneration during radiotherapy,” *Anticancer Research*, vol. 21, no. 6B, pp. 4301–4310, 2001.
- [8] D. Hanahan and J. Folkman, “Patterns and emerging mechanisms of the angiogenic switch during tumorigenesis,” *Cell*, vol. 86, no. 3, pp. 353–364, 1996.
- [9] F. A. L. M. Eskens, “Angiogenesis inhibitors in clinical development; where are we now and where are we going?” *British Journal of Cancer*, vol. 90, no. 1, pp. 1–7, 2004.
- [10] R. J. Oliver, R. T. M. Woodwards, P. Sloan, N. S. Thakker, I. J. Stratford, and R. E. Airley, “Prognostic value of facilitative glucose transporter Glut-1 in oral squamous cell carcinomas treated by surgical resection: results of EORTC translational research fund studies,” *European Journal of Cancer*, vol. 40, no. 4, pp. 503–507, 2004.
- [11] S. Zhou, S. Wang, Q. Wu, J. Fan, and Q. Wang, “Expression of glucose transporter-1 and -3 in the head and neck carcinoma—the correlation of the expression with the biological behaviors,” *ORL*, vol. 70, no. 3, pp. 189–194, 2008.
- [12] J. Overgaard, “Hypoxic modification of radiotherapy in squamous cell carcinoma of the head and neck—a systematic review and meta-analysis,” *Radiotherapy and Oncology*, vol. 100, no. 1, pp. 22–32, 2011.
- [13] G. Niu, X. Sun, Q. Cao et al., “Cetuximab-based immunotherapy and radioimmunotherapy of head and neck squamous cell carcinoma,” *Clinical Cancer Research*, vol. 16, no. 7, pp. 2095–2105, 2010.
- [14] P. Castaldi, L. Leccisotti, F. Bussu, F. Miccichè, and V. Rufini, “Role of 18F-FDG PET-CT in head and neck squamous cell carcinoma,” *Acta Otorhinolaryngologica Italica*, vol. 33, no. 1, pp. 1–8, 2013.
- [15] D. K. Harrison and P. Vaupel, “Heterogeneity in tissue oxygenation: from physiological variability in normal tissues to pathophysiological chaos in malignant tumours,” *Advances in Experimental Medicine and Biology*, vol. 812, pp. 25–31, 2014.
- [16] D. Rischin, R. J. Hicks, R. Fisher et al., “Prognostic significance of [18F]-misonidazole positron emission tomography-detected tumor hypoxia in patients with advanced head and neck cancer randomly assigned to chemoradiation with or without tirapazamine: a substudy of Trans-Tasman Radiation Oncology Group study 98.02,” *Journal of Clinical Oncology*, vol. 24, no. 13, pp. 2098–2104, 2006.
- [17] M. Kikuchi, T. Yamane, S. Shinohara et al., “18F-fluoromisonidazole positron emission tomography before treatment is a predictor of radiotherapy outcome and survival prognosis in patients with head and neck squamous cell carcinoma,” *Annals of Nuclear Medicine*, vol. 25, no. 9, pp. 625–633, 2011.
- [18] M. Souvatzoglou, A. L. Grosu, B. Röper et al., “Tumour hypoxia imaging with [¹⁸F]FAZA PET in head and neck cancer patients: a pilot study,” *European Journal of Nuclear Medicine and Molecular Imaging*, vol. 34, no. 10, pp. 1566–1575, 2007.
- [19] E. J. Postema, A. J. B. McEwan, T. A. Riauka et al., “Initial results of hypoxia imaging using 1- α -d-(5-deoxy-5-[¹⁸F]-fluoroarabinofuranosyl)-2-nitroimidazole (¹⁸F-FAZA),” *European Journal of Nuclear Medicine and Molecular Imaging*, vol. 36, no. 10, pp. 1565–1573, 2009.
- [20] P. Mahy, X. Geets, M. Lonneux et al., “Determination of tumour hypoxia with [18F]EF3 in patients with head and neck tumours: a phase I study to assess the tracer pharmacokinetics, biodistribution and metabolism,” *European Journal of Nuclear Medicine and Molecular Imaging*, vol. 35, no. 7, pp. 1282–1289, 2008.
- [21] G. Komar, M. Seppänen, O. Eskola et al., “18F-EF5: A new PET tracer for imaging hypoxia in head and neck cancer,” *Journal of Nuclear Medicine*, vol. 49, no. 12, pp. 1944–1951, 2008.
- [22] L. Chen, Z. Zhang, H. C. Kolb, J. C. Walsh, J. Zhang, and Y. Guan, “¹⁸F-HX4 hypoxia imaging with PET/CT in head and neck cancer: a comparison with ¹⁸F-FMISO,” *Nuclear Medicine Communications*, vol. 33, no. 10, pp. 1096–1102, 2012.
- [23] Y. Minagawa, K. Shizukuishi, I. Koike et al., “Assessment of tumor hypoxia by ⁶²Cu-ATSM PET/CT as a predictor of response in head and neck cancer: a pilot study,” *Annals of Nuclear Medicine*, vol. 25, no. 5, pp. 339–345, 2011.
- [24] I. Grassi, C. Nanni, G. Cicoria et al., “Usefulness of ⁶⁴Cu-ATSM in head and neck cancer: a preliminary prospective study,” *Clinical Nuclear Medicine*, vol. 39, no. 1, pp. e59–e63, 2014.
- [25] C. J. Kelly and M. Brady, “A model to simulate tumour oxygenation and dynamic [18F]-Fmiso PET data,” *Physics in Medicine and Biology*, vol. 51, no. 22, article 9, pp. 5859–5873, 2006.
- [26] K. Wang, E. Yorke, S. A. Nehmeh, J. L. Humm, and C. C. Ling, “Modeling acute and chronic hypoxia using serial images of 18F-FMISO PET,” *Medical Physics*, vol. 36, no. 10, pp. 4400–4408, 2009.
- [27] R. M. Bartlett, B. J. Beattie, M. Naryanan et al., “Image-guided PO₂ probe measurements correlated with parametric images derived from 18F-fluoromisonidazole small-animal PET data in rats,” *Journal of Nuclear Medicine*, vol. 53, no. 10, pp. 1608–1615, 2012.
- [28] S. Gu, G. Chakraborty, K. Champley et al., “Applying a patient-specific bio-mathematical model of glioma growth to develop virtual [18F]-FMISO-PET images,” *Mathematical Medicine and Biology*, vol. 29, no. 1, pp. 31–48, 2012.
- [29] K. C. McCall, J. L. Humm, R. Bartlett, M. Reese, and S. Carlin, “Copper-64-diacetyl-bis(N(4)-methylthiosemicarbazone) pharmacokinetics in FaDu xenograft tumors and correlation with microscopic markers of hypoxia,” *International Journal of*

- Radiation Oncology Biology Physics*, vol. 84, no. 3, pp. e393–e399, 2012.
- [30] D. Monnich, E. G. Troost, J. H. Kaanders et al., “Correlation between tumor oxygenation and 18F-fluoromisonidazole PET data simulated based on microvessel images,” *Acta Oncologica*, vol. 52, pp. 1308–1313, 2013.
- [31] D. Mönlich, E. G. C. Troost, J. H. A. M. Kaanders, W. J. G. Oyen, M. Alber, and D. Thorwarth, “Modelling and simulation of [¹⁸F]fluoromisonidazole dynamics based on histology-derived microvessel maps,” *Physics in Medicine and Biology*, vol. 56, no. 7, pp. 2045–2057, 2011.
- [32] D. Liu, A. Chalkidou, D. B. Landau, P. K. Marsden, and J. D. Fenwick, “(18)F-FLT uptake kinetics in head and neck squamous cell carcinoma: a PET imaging study,” *Medical Physics*, vol. 41, no. 4, Article ID 041911, 2014.
- [33] I. Toma-Dașu, A. Dașu, and A. Brahme, “Quantifying tumour hypoxia by PET imaging—a theoretical analysis,” *Advances in Experimental Medicine and Biology*, vol. 645, pp. 267–272, 2009.
- [34] B. Titz and R. Jeraj, “An imaging-based tumour growth and treatment response model: Investigating the effect of tumour oxygenation on radiation therapy response,” *Physics in Medicine and Biology*, vol. 53, no. 17, pp. 4471–4488, 2008.
- [35] B. Titz, K. R. Kozak, and R. Jeraj, “Computational modelling of anti-angiogenic therapies based on multiparametric molecular imaging data,” *Physics in Medicine and Biology*, vol. 57, no. 19, pp. 6079–6101, 2012.
- [36] D. Thorwarth and M. Alber, “Individualised radiotherapy on the basis of functional imaging with FMISO PET,” *Zeitschrift für Medizinische Physik*, vol. 18, no. 1, pp. 43–50, 2008.
- [37] H. Cho, E. Ackurstaff, S. Carlin et al., “Noninvasive multimodality imaging of the tumor microenvironment: registered dynamic magnetic resonance imaging and positron emission tomography studies of a preclinical tumor model of tumor hypoxia,” *Neoplasia*, vol. 11, no. 3, pp. 247–259, 2009.
- [38] W. Choi, S. W. Lee, S. H. Park et al., “Planning study for available dose of hypoxic tumor volume using fluorine-18-labeled fluoromisonidazole positron emission tomography for treatment of the head and neck cancer,” *Radiotherapy & Oncology*, vol. 97, no. 2, pp. 176–182, 2010.
- [39] I. Toma-Dașu, J. Uhrdin, L. Antonovic et al., “Dose prescription and treatment planning based on FMISO-PET hypoxia,” *Acta Oncologica*, vol. 51, no. 2, pp. 222–230, 2012.
- [40] E. J. Hall and A. J. Giaccia, *Radiobiology for the Radiologist*, Lippincott Williams & Wilkins, 7th edition, 2012.
- [41] P. Kolstad, “Inter-capillary distance, oxygen tension and local recurrence in cervix cancer,” *Scandinavian Journal of Clinical and Laboratory Investigation*, vol. 106, pp. 145–157, 1968.
- [42] A. Carreau, B. E. Hafny-Rahbi, A. Matejuk, C. Grillon, and C. Kieda, “Why is the partial oxygen pressure of human tissues a crucial parameter? Small molecules and hypoxia,” *Journal of Cellular and Molecular Medicine*, vol. 15, no. 6, pp. 1239–1253, 2011.
- [43] A. R. Padhani, K. A. Krohn, J. S. Lewis, and M. Alber, “Imaging oxygenation of human tumours,” *European Radiology*, vol. 17, no. 4, pp. 861–872, 2007.
- [44] R. P. Mason, D. Zhao, J. Pacheco-Torres et al., “Multimodality imaging of hypoxia in preclinical settings,” *The Quarterly Journal of Nuclear Medicine and Molecular Imaging*, vol. 54, no. 3, pp. 259–280, 2010.
- [45] R. R. Hallac, H. Zhou, R. Pidikiti et al., “Correlations of noninvasive BOLD and TOLD MRI with pO₂ and relevance to tumor radiation response,” *Magnetic Resonance in Medicine*, vol. 71, no. 5, pp. 1863–1873, 2014.
- [46] D. Belkić and K. Belkić, “Molecular imaging in the framework of personalized cancer medicine,” *Israel Medical Association Journal*, vol. 15, no. 11, pp. 665–772, 2013.
- [47] A. Nunn, K. Linder, and H. W. Strauss, “Nitroimidazoles and imaging hypoxia,” *European Journal of Nuclear Medicine*, vol. 22, no. 3, pp. 265–280, 1995.
- [48] J. S. Rasey, Z. Grunbaum, S. Magee et al., “Characterization of radiolabeled fluoromisonidazole as a probe for hypoxic cells,” *Radiation Research*, vol. 111, no. 2, pp. 292–304, 1987.
- [49] J. G. Rajendran, D. L. Schwartz, J. O’Sullivan et al., “Tumor hypoxia imaging with [F-18] fluoromisonidazole positron emission tomography in head and neck cancer,” *Clinical Cancer Research*, vol. 12, no. 18, pp. 5435–5441, 2006.
- [50] B. Gagel, M. Piroth, M. Pinkawa et al., “pO polarography, contrast enhanced color duplex sonography (CDS), [¹⁸F] fluoromisonidazole and [¹⁸F] fluorodeoxyglucose positron emission tomography: validated methods for the evaluation of therapy-relevant tumor oxygenation or only bricks in the puzzle of tumor hypoxia?” *BMC Cancer*, vol. 7, article 113, 2007.
- [51] S. Okamoto, T. Shiga, K. Yasuda et al., “High reproducibility of tumor hypoxia evaluated by ¹⁸F-fluoromisonidazole PET for head and neck cancer,” *Journal of Nuclear Medicine*, vol. 54, no. 2, pp. 201–207, 2013.
- [52] D. Sorger, M. Patt, P. Kumar et al., “[¹⁸F]Fluoroazomycin-arabinofuranoside (¹⁸FAZA) and [¹⁸F]Fluoromisonidazole (18FMISO): a comparative study of their selective uptake in hypoxic cells and PET imaging in experimental rat tumors,” *Nuclear Medicine and Biology*, vol. 30, no. 3, pp. 317–326, 2003.
- [53] L. J. Dubois, N. G. Lieuwes, M. H. M. Janssen et al., “Preclinical evaluation and validation of [18F]HX4, a promising hypoxia marker for imaging,” *Proceedings of the National Academy of Sciences of the United States of America*, vol. 108, no. 35, pp. 14620–14625, 2011.
- [54] J. S. Lewis, D. W. McCarthy, T. J. McCarthy, Y. Fujibayashi, and M. J. Welch, “Evaluation of ⁶⁴Cu-ATSM in vitro and in vivo in a hypoxic tumor model,” *Journal of Nuclear Medicine*, vol. 40, no. 1, pp. 177–183, 1999.
- [55] L. G. Strauss, L. Pan, C. Cheng, U. Haberkorn, and A. Dimitrakopoulou-Strauss, “Shortened acquisition protocols for the quantitative assessment of the 2-tissue-compartment model using dynamic PET/CT 18F-FDG studies,” *Journal of Nuclear Medicine*, vol. 52, no. 3, pp. 379–385, 2011.
- [56] N. A. Mullani, R. S. Herbst, R. G. O’Neil, K. L. Gould, B. J. Barron, and J. L. Abbruzzese, “Tumor blood flow measured by PET dynamic imaging of first-pass 18F-FDG uptake: a comparison with 15O-labeled water-measured blood flow,” *Journal of Nuclear Medicine*, vol. 49, no. 4, pp. 517–523, 2008.
- [57] J. Rødal, E. Rusten, Å. Søvik, H. K. Skogmo, and E. Malinen, “Functional imaging to monitor vascular and metabolic response in canine head and neck tumors during fractionated radiotherapy,” *Acta Oncologica*, vol. 52, no. 7, pp. 1293–1299, 2013.
- [58] D. Mönlich, E. G. C. Troost, J. H. A. M. Kaanders, W. J. G. Oyen, M. Alber, and D. Thorwarth, “Modelling and simulation of the influence of acute and chronic hypoxia on [18F]fluoromisonidazole PET imaging,” *Physics in Medicine and Biology*, vol. 57, no. 6, pp. 1675–1684, 2012.
- [59] P. Workman, “Pharmacokinetics of hypoxic cell radiosensitizers: a review,” *Cancer Clinical Trials*, vol. 3, no. 3, pp. 237–251, 1980.

- [60] J. J. Casciari, M. M. Graham, and J. S. Rasey, "A modeling approach for quantifying tumor hypoxia with [F- 18]fluoromisonidazole PET time-activity data," *Medical Physics*, vol. 22, no. 7, pp. 1127–1139, 1995.
- [61] M. Bruehlmeier, U. Roelcke, P. A. Schubiger, and S. M. Ametamey, "Assessment of hypoxia and perfusion in human brain tumors using PET with 18F-fluoromisonidazole and 15O-H₂O," *Journal of Nuclear Medicine*, vol. 45, no. 11, pp. 1851–1859, 2004.
- [62] D. Zips, K. Zöphel, N. Abolmaali et al., "Exploratory prospective trial of hypoxia-specific PET imaging during radiochemotherapy in patients with locally advanced head-and-neck cancer," *Radiotherapy & Oncology*, vol. 105, no. 1, pp. 21–28, 2012.
- [63] D. D'Ambrosio, F. Zagni, A. E. Spinelli, and M. Marengo, "Attenuation correction for small animal PET images: a comparison of two methods," *Computational and Mathematical Methods in Medicine*, vol. 2013, Article ID 103476, 12 pages, 2013.
- [64] M. Soret, S. L. Bacharach, and I. Buvat, "Partial-volume effect in PET tumor imaging," *Journal of Nuclear Medicine*, vol. 48, no. 6, pp. 932–945, 2007.
- [65] X. Geets, V. Gregoire, and J. A. Lee, "Implementation of hypoxia PET imaging in radiation therapy planning," *The Quarterly Journal of Nuclear Medicine and Molecular*, vol. 57, pp. 271–282, 2013.

Research Article

Delay Differential Model for Tumour-Immune Response with Chemoimmunotherapy and Optimal Control

F. A. Rihan,^{1,2} D. H. Abdelrahman,¹ F. Al-Maskari,³ F. Ibrahim,^{4,5} and M. A. Abdeen²

¹ Department of Mathematical Sciences, College of Science, UAE University, P.O. Box 15551, Al-Ain, UAE

² Department of Mathematics, Faculty of Science, Helwan University, Cairo 11795, Egypt

³ Zayed bin Sultan Al Nahyan Center for Health Sciences, College of Medicine and Health Sciences, UAE University, P.O. Box 17666, Al-Ain, UAE

⁴ Institut für Angewandte Mathematik, LS III, TU Dortmund, Vogelpothsweg 87, 44227 Dortmund, Germany

⁵ Department of Mathematics, Faculty of Science, South Valley University, Qena 83523, Egypt

Correspondence should be addressed to F. A. Rihan; frihan@uaeu.ac.ae

Received 13 May 2014; Revised 1 July 2014; Accepted 3 July 2014; Published 14 August 2014

Academic Editor: Loredana G. Marcu

Copyright © 2014 F. A. Rihan et al. This is an open access article distributed under the Creative Commons Attribution License, which permits unrestricted use, distribution, and reproduction in any medium, provided the original work is properly cited.

We present a delay differential model with optimal control that describes the interactions of the tumour cells and immune response cells with external therapy. The intracellular delay is incorporated into the model to justify the time required to stimulate the effector cells. The optimal control variables are incorporated to identify the best treatment strategy with minimum side effects by blocking the production of new tumour cells and keeping the number of normal cells above 75% of its carrying capacity. Existence of the optimal control pair and optimality system are established. Pontryagin's maximum principle is applicable to characterize the optimal controls. The model displays a tumour-free steady state and up to three coexisting steady states. The numerical results show that the optimal treatment strategies reduce the tumour cells load and increase the effector cells after a few days of therapy. The performance of combination therapy protocol of immunochemotherapy is better than the standard protocol of chemotherapy alone.

1. Introduction

Cancer is considered one of the most complicated diseases to be treated clinically and one of the main causes of death. Accordingly, a great research effort is being devoted to understand the interaction between the tumour cells and the immune system. The treatment of cancer is then one of the most challenging problems of modern medicine. The cancer treatment should kill cancer cells in the entire body and in the meantime keep the healthy cells above the minimum level. Chemotherapy is one of the most prominent cancer treatment modalities. However, it is not always a comprehensive solution for tumor regression. Other treatment options, including surgery, immunotherapy, and radiation, are often able to force the cancer into remission, but better and suitable treatments are needed to fulfil the requirements [1–3].

Recently, chemotherapy is used in combination with immunotherapy to protect the patient from opportunistic infection, as well as fighting the cancer itself [4, 5]. This

is due to the fact that the chemotherapy treatment kills both cancerous and healthy cells and therefore it depletes the patients immune system, making the patient prone to dangerous infections. For this and other reasons, it is desirable to strengthen the immune system after an immune-depleting course of chemotherapy. Additionally, however, the ability to recruit the body's own defenses to fight the cancer can be a powerful treatment strategy. Therefore, maintaining a strong immune system, by combining immunotherapy during chemotherapy, may be essential to successfully fight the cancer. However, the query now is how to most effectively combine cancer immunotherapy and chemotherapy?

Mathematical models, using ordinary, partial, and delay differential equations, play an important role in understanding the dynamics and tracking tumour and immune populations over time (see, e.g., [6–14]). Kuznetsov et al. [3] model the interactions of cytotoxic T lymphocyte (CTL) response and the growth of an immunogenic tumour. In the contributions of [15–17], the authors take into account

the penetration of the tumour cells by the effector cells, which simultaneously causes the inactivation of effector cells. Recently, in [18], the authors adopted a predator-prey formulation of the tumour immunity problem as a battle between immune cells and tumour cells (predators and prey, resp.). Many research papers have also been done on formulations of the mathematical models describing the interaction between tumour cells and immune cells alone, between tumour cells and normal cells alone, and between tumour cells and chemotherapy treatment alone [19, 20]. We should mention here that the application of the optimal control theory requires the boundedness of the solutions of the model populations; see also [21, 22].

The objective of this paper is to adopt a delay differential model and analyze and provide computationally an optimal way to combine chemotherapy and immunotherapy treatment strategies that identify the best treatment strategy that can minimize the tumor load while maximizing the strength of the immune system. We formulate and analyze a delay differential model describing immune response and tumour cells under the influence of chemotherapy alone and the combinations of chemotherapy and immunotherapy. The outline of the paper is as follows. In Section 2, we describe the model. In Section 3, we study the qualitative behaviour of the model without external therapy. In Section 4, we describe the optimal control problem governed by DDEs with only chemotherapy control variable. Existence of the solution and optimality conditions are discussed in Sections 5 and 6. In Section 7, we extend the control problem to include a combination of chemotherapy and immunotherapy treatments with two-control variable. Numerical simulations and conclusion are given in Sections 8 and 9.

2. Description of the Model

Let us recall Kuznetsov et al.'s model [3] that describes the dynamics of tumour immune system interactions by incorporating a system of five ordinary differential equations (ODEs) model; then we reduce it into two equations but with time delays. The model describes the response of the effector cells (ECs) to the growth of tumour cells (TCs). The penetration of TCs by ECs has been taken into account, which simultaneously causes the inactivation of ECs. It is assumed that interactions between the ECs and TCs are *in vitro* such that $E(t)$, $T(t)$, $C(t)$, $E^*(t)$, and $T^*(t)$ denote the local concentrations of ECs, TCs, EC-TC conjugates, inactivated ECs, and "lethally hit" TCs, respectively. The total population of unattacked TCs is $T_{\text{tot}}(t) = T(t) + C(t)$. The rate of binding of ECs to TCs and the rate of separation of ECs from TCs without damaging them are denoted by k_1 and k_{-1} , respectively. The rate at which EC-TC integrations program for lysis is denoted by k_2 while the rate at which EC-TC interaction inactivate ECs is denoted by k_3 . The model takes the form

$$\begin{aligned} \frac{dE(t)}{dt} &= \sigma + F(C(t), T(t)) - d_1 E(t) - k_1 E(t) T(t) \\ &\quad + (k_{-1} + k_3) C(t), \end{aligned}$$

$$\begin{aligned} \frac{dT(t)}{dt} &= \alpha T(t) (1 - \beta T_{\text{tot}}(t)) - k_1 E(t) T(t) \\ &\quad + (k_{-1} + k_3) C(t), \end{aligned}$$

$$\frac{dC(t)}{dt} = k_1 E(t) T(t) - (k_{-1} + k_2 + k_3) C(t),$$

$$\frac{dE^*(t)}{dt} = k_3 C(t) - d_2 E^*(t),$$

$$\frac{dT^*(t)}{dt} = k_2 C(t) - d_3 T^*(t).$$

(1)

Here, the parameter σ represents the normal rate (not increased by the presence of the tumour) of the flow of adult ECs into the tumour side (region), $\mathcal{F}(C(t), T(t)) = \mathcal{F}(E(t), T(t)) > 0$ (when $T(t) > 0$) describes the accumulation of ECs in the tumour side due to the presence of the tumour. However, d_1 , d_2 , and d_3 are the coefficients of the processes of destruction and migration of E , E^* , and T^* , respectively. The maximal growth of tumour is represented by the coefficient α , and β^{-1} is the environment capacity. If we assume that $dC(t)/dt \approx 0$, therefore $C(t) \approx KE(t)T(t)$ where $K = k_1/(k_{-1} + k_2 + k_3)$, and the model can be reduced to two equations which describe the behavior of ECs and TCs only [2, 3]. That leads to the fact that the rate of stimulated accumulation has some maximum value as TCs get large.

Thus, the reduced model that describes the interactions between the two populations, tumour cells $T(t)$ and activated effector cells $E(t)$ (such as cytotoxic T-cells or natural killer cells), is of the form

$$\begin{aligned} \frac{dE(t)}{dt} &= \sigma + \mathcal{F}(E(t), T(t)) - \mu E(t) T(t) - \delta E(t), \\ \frac{dT(t)}{dt} &= \alpha T(t) (1 - \beta T(t)) - n E(t) T(t), \end{aligned} \quad (2)$$

with the initial conditions $E(0) = E_0$ and $T(0) = T_0$. The interaction between the effector cells and tumour cells can reduce the size of both populations with different rates. This is expressed as $-\mu E(t)T(t)$ and $-n E(t)T(t)$ to illustrate the interaction between the tumour cells and effector cells. As a result of this interaction, the immune effector cells decrease the population of tumour cells at the rate n . Additionally, tumour cells infect some of the effector cells and, therefore, the population of uninfected effector cells decreases at the rate μ .

If one considers $T(t)$ as prey and $E(t)$ as predator, then $\mathcal{F}(E, T)$ may take the form $\mathcal{F}(E, T) = \rho E(t)T(t)/(\eta + T(t))$ which is Michaelis-Menton form. In this term, ρ is the maximum immune response rate and η is the steepness of immune response. The presence of the tumour cells virtually initiates the proliferation of tumour-specific effector cells to reach a saturation level parallel to the increase in the tumour populations. Hence, the recruitment function should be zero in the absence of the tumour cells, whereas it should increase monotonically towards a horizontal asymptote [23]. We also incorporate a discrete time-delay τ into the model, to describe

the time needed by the immune system to develop a suitable response after recognizing the tumour cells. Accordingly, the model with discrete time delay takes the form

$$\begin{aligned} \frac{dE(t)}{dt} &= \sigma + \frac{\rho E(t-\tau)T(t-\tau)}{\eta + T(t-\tau)} - \mu E(t-\tau)T(t-\tau) - \delta E(t), \\ \frac{dT(t)}{dt} &= r_2 T(t)(1 - \beta T(t)) - nE(t)T(t), \\ &t \geq 0, \end{aligned} \quad (3)$$

with the initial functions $E(t) = \psi_1(t)$ and $E(t) = \psi_2(t)$, for all $t \in [-\tau, 0]$. Here σ represents the normal rate (not increased by the presence of the tumour) of the flow of adult effector cells into the tumour side (region). The source of the immune cells is considered to be outside of the system, so it is reasonable to assume a constant influx rate σ . Furthermore, in the absence of any tumour, the cells will die at the rate δ . The presence of tumour cells stimulates the immune response, represented by the positive nonlinear growth term for the immune cells $\rho E(t-\tau)T(t-\tau)/(\eta + T(t-\tau))$ where ρ and η are positive constants and $\tau \geq 0$ is the time delay that presents the time needed by the immune system to develop a suitable response after recognizing the tumour cells. The saturation term (Michaelis-Menton form) with the $E(t)$ compartment and logistic term with the $T(t)$ compartment are consold. The presence of the tumour cells virtually initiates the proliferation of tumour-specific effector cells to reach a saturation level parallel to the increase in the tumour populations. Let us first prove the nonnegativity and boundedness solutions of the underlying DDEs model (3) (see [24]).

2.1. Nonnegativity and Boundedness Solutions of Model (3). To show that the solutions of model (3) are bounded and remain nonnegative in the domain of its application for sufficiently large values of time t , we recall the following lemma.

Lemma 1 (Gronwall's Lemma [25, page 9]). *Let x , ψ , and χ be real continuous functions defined in $[a, b]$, $\chi \geq 0$ for $t \in [a, b]$. One supposes that on $[a, b]$ one has the inequality $x(t) \leq \psi(t) + \int_a^t \chi(s)x(s)ds$. Then $x(t) \leq \psi(t) + \int_a^t \chi(s)\psi(s)e^{\int_s^t \chi(\xi)d\xi} ds$ in $[a, b]$.*

Therefore, we arrive at the following proposition.

Proposition 2. *Let (E, T) be a solution of the DDEs model (3); then $E(t) < M_1$ and $T(t) < M_2$ for all sufficiently large time t , where*

$$\begin{aligned} M_1 &= E(0) + \frac{\sigma}{\delta} \exp(\delta t) \\ &+ \int_0^t \left[\rho e^{\delta(\tau+s)} \left(E(0) + \frac{\sigma}{\delta} e^{\delta s} \right) \right. \\ &\quad \left. \times \exp \left(\int_s^t \rho e^{\delta(\tau+\xi)} d\xi \right) \right] ds, \end{aligned}$$

$$M_2 = \max \left(\frac{1}{\beta}, T(0) \right). \quad (4)$$

Proof. Let (E, T) denote the solution of model (3). From the second equation of system (3), we have $dT/dt \leq r_2 T(t)(1 - \beta T(t))$. Thus, $T(t)$ may be compared with the solution of

$$\frac{dX}{dt} = r_2 X(t)(1 - \beta X(t)), \quad \text{with } X(0) = T(0). \quad (5)$$

This proves that $T(t) < M_2$. From the first equation of system (3), we obtain

$$\begin{aligned} E(t) &= \exp(-\delta t) \\ &\times \left\{ E(0) + \int_0^t \left[\sigma + \frac{\rho E(s-\tau)T(s-\tau)}{\eta + T(s-\tau)} \right. \right. \\ &\quad \left. \left. - \mu E(s-\tau)T(s-\tau) \right] \right. \\ &\quad \left. \times \exp(\delta s) ds \right\}. \end{aligned} \quad (6)$$

To show that $E(t)$ is bounded, we use the generalized Gronwall Lemma. Since $T/(\eta + T) < 1$ and $\exp(-\delta t) \in (0, 1]$, we have

$$E(t) \leq E_0 + \frac{\sigma}{\delta} \exp(\delta t) + \int_0^t \rho E(s-\tau) \exp(\delta s) ds. \quad (7)$$

The generalized Gronwall Lemma gives $E(t) < M_1$ where M_1 is uniformly bounded. It follows that if (E, T) is a solution of (3), then $(E, T) < (M_1, M_2)$ for all t . This shows that the solutions of model (3) are uniformly bounded. This completes the proof. \square

From (1) and the solution $T(t) = T(0) \exp(\int_0^t [r_2(1 - \beta T(s)) - E(s)] ds)$, we arrive at the following result.

Corollary 3. *If $\rho/(\eta + T) \geq \mu$, then the solutions (E, T) for model (3) are nonnegative for any nonnegative initial condition. However, if $\rho/(\eta + T) < \mu$, then there exist nonnegative initial conditions such that $E(t)$ becomes negative in a finite time interval.*

2.2. Model with Chemotherapy. We extend model (3) to consider extra two variables, namely, amount of chemotherapy, $u(t)$, and normal cells, $N(t)$ (see Figure 1). We also assume

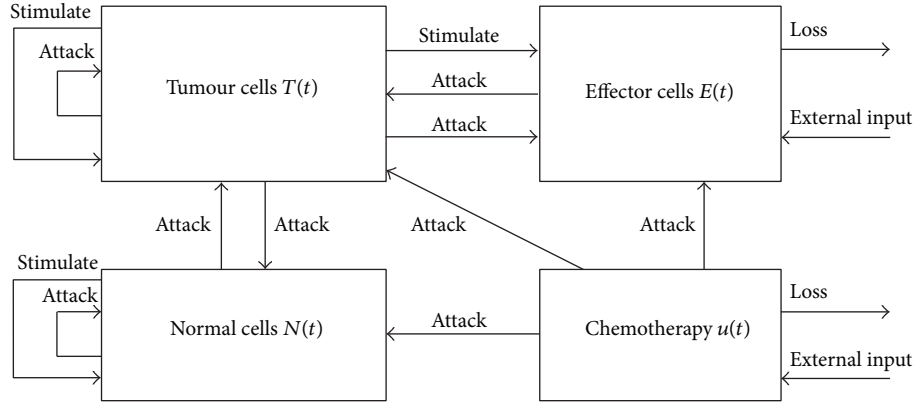


FIGURE 1: The interaction of tumour cells, immune cells, and normal cells in the presence of chemotherapy drug.

a homogeneity of the tumour cells. The modified model is

$$\begin{aligned}
 \frac{dE(t)}{dt} &= \sigma + \frac{\rho E(t-\tau)T(t-\tau)}{\eta + T(t-\tau)} \\
 &\quad - \mu E(t-\tau)T(t-\tau) - \delta E(t) \\
 &\quad - a_1(1 - e^{-u(t)})E(t), \\
 \frac{dT(t)}{dt} &= r_2 T(t)(1 - \beta T(t)) - nE(t)T(t) \\
 &\quad - c_1 N(t)T(t) - a_2(1 - e^{-u})T(t), \\
 \frac{dN(t)}{dt} &= r_3 N(t)(1 - \beta_2 N(t)) - c_2 T(t)N(t) \\
 &\quad - a_3(1 - e^{-u})N(t), \\
 \frac{du(t)}{dt} &= v(t) - d_1 u(t).
 \end{aligned} \tag{8}$$

We assume that the drug kills all types of cells but that the killing rate differs for each type of cells; $F(u) = a_i(1 - e^{-u})$ is the fraction cell kill for a given amount of drug, $u(t)$, at the tumour site. We denote by a_1 , a_2 , and a_3 the three different response coefficients. $v(t)$ represents the amount of dose that is injected into the system, while d_1 is the decay rate of the drug once it is injected. In this case, the quantity we will control directly is not $u(t)$ but $v(t)$. The tumour cells and normal cells are modelled by a logistic growth law, with the parameters r_i representing the growth rate of two types of cells: $i = 2$ identifies the parameter associated with tumour, and $i = 3$ identifies the one associated with the normal tissue; β and β_2 are the reciprocal carrying capacities of tumour cells and host cells, respectively. In addition, there are two terms representing the competition between the tumour and host cells $-c_1 NT$ and $-c_2 NT$.

Let $\mathcal{C} = \mathcal{C}([- \tau, 0], \mathbb{R}^4)$ be the Banach space of continuous functions mapping the interval $[- \tau, 0]$ into \mathbb{R}^4 with the topology of uniform convergence. It is easy to show that there exists a unique solution $(E(t), T(t), N(t), u(t))$ of system (8)

with initial data $(E_0, T_0, N_0, u_0) \in \mathcal{C}$. For biological reasons, we assume that the initial data of system (8) satisfy $E_0 \geq 0$, $T_0 \geq 0$, $N_0 \geq 0$, and $u_0 \geq 0$. For $\tau = 0$, the model is reduced to ODEs model developed by De Pillis and Radunskaya in [26].

Remark 4. We consider that the units of the model cells are normalized, so that $\beta_2 = 1$.

The main objective in developing chemotherapy treatment, in system (8), is to reach either tumour-free steady state or coexisting steady state in which the tumour cells' size is small, while the normal cells' size is closed to its normalized carrying capacity. We next start the analysis with studying the stability of the system when there is no drug (treatment) input; that is, $u(t) = 0$, for all t .

3. Drug-Free Steady States and Their Stability

In the absence of chemotherapy ($u(t) = 0$), model (8) has the following types of steady states:

- (a) tumour-free steady state, where the tumour cells population is zero, while the normal cells survive. This steady state has the form $\mathcal{E}_0 = (\sigma/\delta, 0, 1)$;
- (b) dead (lethal) steady state, where the normal cells population is zero, which has the following forms:
 - (i) $(\sigma/\delta, 0, 0)$ in which the normal and tumour cell populations have died off,
 - (ii) $(f(T^*), T^*, 0)$ where the normal cells alone have died off and the tumour cells have survived, where

$$f(T) = \frac{\sigma(\eta + T)}{\mu T(\eta + T) + \delta(\eta + T) - \rho T}, \tag{9}$$

and T^* is a nonnegative solution for

$$T^* + \left(\frac{n}{r_2 \beta}\right) f(T^*) - \frac{1}{\beta} = 0; \tag{10}$$

TABLE 1: The stability results for the coexisting steady states by using the functions ρ and σ , while fixing the rest of the parameters as mentioned in the text.

Region in Figure 2	ρ	σ	Steady state (E^*, T^*, N^*)	Eigenvalues $\lambda_1, \lambda_2, \lambda_3$	Stability for $\tau \geq 0$
Light blue (1a)	0.1	0.05	(0.0269, 486.9244, 0.9999)	-0.9509, -1.9105, -1	Stable node
Light blue (1b)	1.4	0.1	(1.0299, 0.0238, 0.9999)	-1, -0.0486 - 0.3096i, -0.0486 + 0.3096i	Stable spiral for $\tau < \tau^*$, stable limit cycles at $\tau = \tau^*$
Orange (2)	0.2	0.23	(0.1648, 419.9672, 0.9999)	-0.5942, -1, -1.7876	Stable node
			(0.8656, 79.7712, 0.99)	0.276, -1, -0.7291	Unstable saddle node
Brown (3)	0.6	0.1	(0.0789, 461.688, 0.99)	-0.7137, -1.5050, -1	Stable node
			(0.7236, 148.7078, 0.99)	0.4060, -1, -0.8506	Unstable saddle node
			(1.0298, 0.0623, 0.99)	-1, -0.0486 - 0.2922i, -0.0486 + 0.2922i	Stable spiral for $\tau < \tau^*$, stable limit cycles at $\tau = \tau^*$

(c) coexisting steady state, where both normal and tumour cells coexist with nonzero populations. The steady state is given by $\mathcal{E}_+ = (f(T^*), T^*, g(T^*))$ where $g(T^*) = 1 - (c_2/r_3)T^*$, and T^* is a nonnegative solution of

$$\begin{aligned}
C_3 T^3 + C_2 T^2 + C_1 T + C_0 &= 0, \quad \text{where} \\
C_3 &= -\mu r_2 \beta + \frac{\mu c_1 c_2}{r_3}, \\
C_2 &= -\mu \eta r_2 \beta + \frac{\mu \eta c_1 c_2}{r_3} + \mu r_2 - \mu c_1 - \delta r_2 \beta \\
&\quad + \frac{\delta c_1 c_2}{r_3} + \rho r_2 \beta - \frac{\rho c_1 c_2}{r_3}, \\
C_1 &= \mu \eta r_2 - \mu \eta c_1 - \delta \eta r_2 \beta + \frac{\delta \eta c_1 c_2}{r_3} + \delta r_2 \\
&\quad - \delta c_1 - \rho r_2 + \rho c_1 - \sigma \eta, \\
C_0 &= \delta \eta r_2 - \delta \eta c_1 - \sigma \eta \eta.
\end{aligned} \tag{11}$$

The number of coexisting steady states mainly depends on the parameter values. There could be zero, one, two, or three of these steady states (see Figure 2). We next study the stability of the previously mentioned steady states.

3.1. Stability of Tumour-Free Steady State. In this subsection, we investigate the parameter ranges for which the tumour-free steady state \mathcal{E}_0 is locally asymptotically stable. The Jacobian matrix of the linearized system at the tumour-free steady state is given by

$$J_{\mathcal{E}_0} = \begin{pmatrix} -\delta & \frac{\rho \sigma}{\eta \delta} e^{-\lambda \tau} - \frac{\mu \sigma}{\delta} e^{-\lambda \tau} & 0 \\ 0 & r_2 - \frac{n \sigma}{\delta} - c_1 & 0 \\ 0 & -c_2 & -r_3 \end{pmatrix} \tag{12}$$

with the eigenvalues $\lambda_1 = -\delta < 0$, $\lambda_2 = r_2 - n\sigma/\delta - c_1$, and $\lambda_3 = -r_3 < 0$. Hence, the tumour-free steady state \mathcal{E}_0 is locally stable if $\lambda_2 < 0$ if and only if

$$r_2 < \frac{n\sigma}{\delta} + c_1, \quad \forall \tau \geq 0. \tag{13}$$

This relates r_2 (the growth rate of the tumour cells) to the $n\sigma/\delta$ (the resistance coefficient), which measures how efficiently the immune system competes with the tumour cells. If this tumour-free steady state is unstable, then no amount of chemotherapy will be able to completely eradicate the tumour cells.

3.2. Stability of Lethal Steady States. The same analysis done above shows that the deadly steady state $(\sigma/\delta, 0, 0)$ has the eigenvalues $\lambda_1 = -\delta < 0$, $\lambda_2 = r_2 - n\sigma/\delta$, and $\lambda_3 = r_3 > 0$ and hence it is unstable saddle point, while the other deadly steady state $(f(T^*), T^*, 0)$ can be either stable or unstable depending on the model parameters and the value of the time-delay τ . This can be shown by using Routh Harwitz test and Rouché's theorem as shown in detail in the previous chapters. Since the stability of this steady state is not needed for the developing treatment therapy, we will not introduce more details in this part.

3.3. Stability of Coexisting Steady States. To study the stability of the coexisting steady states, we vary the two parameters ρ (the immune cells growth rate) and σ (the normal flow rate of immune cells), with fixing the other parameters: $\delta = 0.2$, $\eta = 0.3$, $\mu = 0.003611$, $r_2 = 1.03$, $r_3 = 1$, $\beta = 2 \times 10^{-3}$, $n = 1$, $c_1 = 0.00003$, and $c_2 = 3 \times 10^{-9}$. Table 1 summarizes the existence and stability results of the coexisting steady states as present in different regions of Figure 2. It shows that the light blue region (1a) represents the ‘‘escape’’ case where there is a unique stable node steady state with high tumour size, while the light blue region (1b) represents the case where there is a unique steady state with low tumour size. It is stable spiral for $\tau < \tau^*$, while at $\tau = \tau^*$ the

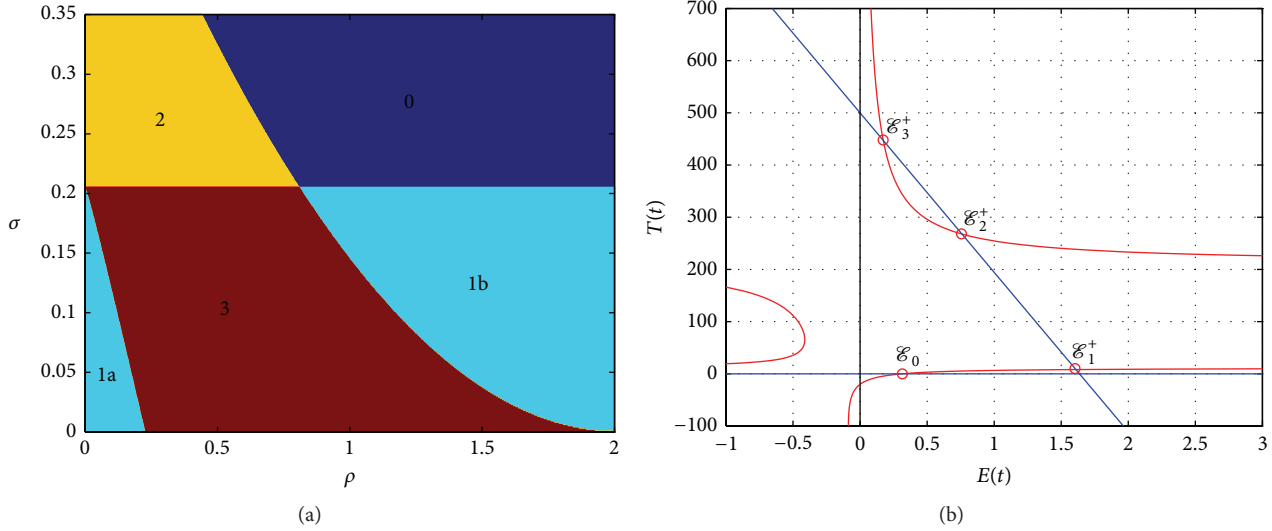


FIGURE 2: (a) shows the regions of existence of coexisting equilibria of model (3) in (ρ, σ) -plane with the parameter values $\delta = 0.2$, $\eta = 0.3$, $\mu = 0.003611$, $r_2 = 1.03$, $r_3 = 1$, $\beta = 2 \times 10^{-3}$, $n = 1$, $c_1 = 0.00003$, and $c_2 = 3 \times 10^{-9}$. The dark blue region (0) represents the case where there is no equilibrium, the light blue regions (1a, 1b) represent the case where there is a unique equilibrium, the orange region (2) represents the case where there are two steady states, and the brown region (3) represents the case where there is three equilibria. (b) shows the nullclines of the model which has up to four steady states: tumour-free steady state “ \mathcal{E}_0^+ ”; tumour dormancy steady state “ \mathcal{E}_1^+ ”; medium concentration tumour steady state “ \mathcal{E}_2^+ ”; and escape tumour steady state “ \mathcal{E}_3^+ ”.

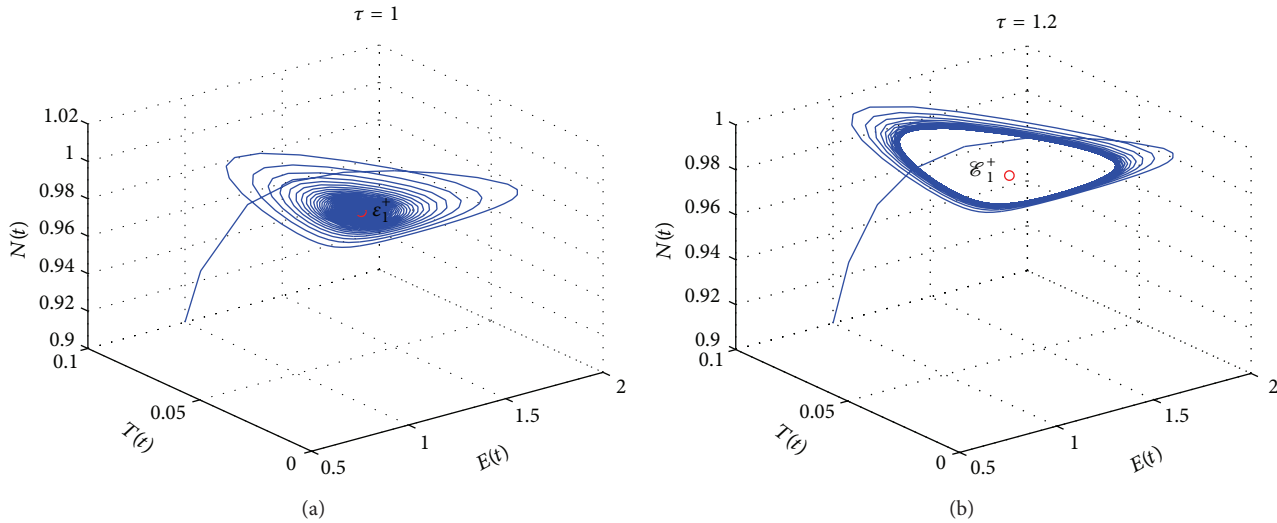


FIGURE 3: The phase space for the cell populations in the case where $\rho = 1.4$ and $\sigma = 0.1$. (a) shows that, for $\tau = 1$, the steady state is asymptotically stable. (b) shows that, for $\tau = 1.2$, a limit cycle is born around the steady state.

limit cycle occurs due to Hopf bifurcation. Furthermore, the orange region (2) represents the case where there are two steady states; one is stable node and the other is unstable saddle node. To this end, the brown region (3) represents the case where there are three steady states: one is stable node, one is unstable node, and the last steady state is spiral stable for $\tau < \tau^*$, while the limit cycle occurs at $\tau = \tau^*$. Of interest are the existence and stability of steady states where a small tumour population size might coexist with a large number of normal cells. Figure 3 presents the phase space for the cell

populations in the case where $\rho = 1.4$ and $\sigma = 0.1$. It shows that, for $\tau = 0.8$, the steady state is asymptotically stable (Figure 3(a)), while, for $\tau = 1.2$, a limit cycle is born around the steady state (Figure 3(b)). We utilize MIDDE code [27] to solve the DDEs model, which is suitable to simulate stiff and nonstiff problems, using monoimplicit RK methods [28]. We next consider the chemotherapy treatment ($u(t) > 0$) in the underlying model and establish the existence of an optimal control for the model and provide necessary conditions for the optimal control.

4. Optimal Control Problem Governed by DDEs

Once a suitable model of interacting cell populations is constructed, we then focus on the design of an efficient treatment protocol, where we employ the tools of optimal control theory.

Consider the optimal control problem with pure state constraints and control bounds, as follows:

$$\max_{x,v} J(x, v) = \Psi(x(t_f)) + \int_0^{t_f} L(t, x(t), v(t)) dt, \quad (14a)$$

subject to the DDEs

$$x'(t) = f(t, x(t), x(t-\tau), v(t)), \quad t \in [0, t_f], \quad (14b)$$

$$x(t) = \phi(t), \quad t \in [-\tau, 0], \quad (14c)$$

with the control constraint

$$a \leq v(t) \leq b, \quad t \in [0, t_f] \quad (14d)$$

and state constraint

$$x(t) \geq c, \quad t \in [0, t_f]. \quad (14e)$$

J is called objective functional and the integrand $L(\cdot)$ is called the Lagrangian of objective functional. Furthermore, a and b are called the lower and upper bounds. The function $v(t)$ is called an admissible control if and only if it fulfills inequality constraints (14d). The set of all admissible controls is called the admissible set and we referred to it by V_{ad} (where ‘‘ad’’ stands for the admissible). The state $x(\cdot)$ enters with a delay τ as $x(t-\tau)$ in the system of the state equations (14b) while it is evaluated at the time t as $x(t)$ in the objective functional (14a). The set of all admissible states X_{ad} , which satisfy the state equations and the state constraint, is called the set of admissible state.

The goal of chemotherapy is to eradicate the tumour cells, while maintaining adequate amounts of healthy tissue. From a mathematical point of view, adequate destruction to tumour cells might mean forcing the system out of the basin of an unhealthy spiral node, out of a limit cycle, and into a basin of attraction of a stable tumour-free equilibrium. Alternatively, if the therapy pushes the system into a limit cycle in which the size of the tumour is small for a long period of time (as long as the life of the patient, for example), this could also be considered a ‘‘cure.’’

Optimality in treatment might be defined in a variety of ways. Some studies have been done in which the total amount of drug administered is minimized, or the number of tumour cells is minimized. The general goal is to keep the patient healthy while killing the tumour. Since our model takes into account the toxicity of the drug to all types of cells, our control problem consists of determining the function $v(t)$ that will maximize the amount of effector cells and minimize the number of tumour cells and the cost of the control with the constraint that we do not kill too many normal cells. If the units of cells are normalized, so that the

carrying capacity of normal cells is 1, we then require that the number of normal cells stays above three-fourths of the carrying capacity. Therefore, our main objective is to optimize the functional

$$\max_{v \in V_{\text{ad}}} J(v) = \int_0^{t_f} \left(E(t) - T(t) - \frac{B_v}{2} [v(t)]^2 \right) dt \quad (15a)$$

which subject to the underlying DDEs

$$\begin{aligned} \frac{dE(t)}{dt} &= \sigma + \frac{\rho E(t-\tau)T(t-\tau)}{\eta + T(t-\tau)} \\ &\quad - \mu E(t-\tau)T(t-\tau) - \delta E(t) \\ &\quad - a_1(1 - e^{-u(t)})E(t), \end{aligned} \quad (15b)$$

$$\frac{dT(t)}{dt} = r_2 T(t)(1 - \beta T(t)) - nE(t)T(t) \quad (15c)$$

$$- c_1 N(t)T(t) - a_2(1 - e^{-u})T(t),$$

$$\frac{dN(t)}{dt} = r_3 N(t)(1 - \beta_2 N(t)) - c_2 T(t)N(t) \quad (15d)$$

$$- a_3(1 - e^{-u})N(t),$$

$$\frac{du(t)}{dt} = v(t) - d_1 u(t) \quad (15e)$$

with control constraint

$$0 \leq v(t) \leq v_{\text{max}} < \infty, \quad t \in [0, t_f] \quad (15f)$$

and state constraint

$$k(N) = N - 0.75 \geq 0, \quad t \in [0, t_f]. \quad (15g)$$

Here, B_v is a weight factor that describes the patient’s acceptance level of chemotherapy. We choose the control parameter as a class of piecewise continuous functions defined for all t such that $0 \leq v(t) \leq v_{\text{max}} < \infty$, where $v(t) = v_{\text{max}}$ represents the maximum chemotherapy, while $v(t) = 0$ represents the case where there is no chemotherapy. Thus, we depict the class of admissible controls as

$$\begin{aligned} V_{\text{ad}} &= \left\{ v \in L^\infty([0, t_f], \mathbb{R}) \mid \right. \\ &\quad \left. 0 \leq v(t) \leq v_{\text{max}} < \infty, \forall t \in [0, t_f] \right\}. \end{aligned} \quad (16)$$

We next prove the existence of the optimal solution of the underlying system (15a)–(15g).

5. Existence of an Optimal Solution

To prove the existence of the optimal solution of (15a)–(15g), we use the results of Fleming and Rishel [29, Theorem 4.1, pages 68–69] and Lukes [30, Theorem 9.2.1, page 182].

Theorem 5. *There exists an optimal solution $(x^*, v^*) \in W^{1,\infty}([0, t_f], \mathbb{R}^4) \times L^\infty([0, t_f], \mathbb{R})$ for the optimal control problem (15a)–(15g) such that*

$$J(v^*) = \max_{v \in V_{\text{ad}}} J(v), \quad (17)$$

where $x^* = [E^*, T^*, N^*, u^*]^T$ if the following conditions are satisfied.

- (1) The set of admissible state is nonempty.
- (2) The admissible set V_{ad} is nonempty, convex, and closed.
- (3) The right-hand side of the state system is bounded by a linear combination of the state and control variables.
- (4) The integrand, $L(E, T, v) = (E(t) - T(t) - (B_v/2)[v(t)]^2)$, of the objective functional is a concave on V_{ad} .
- (5) There exist constants $h_2, h_3 > 0$, and $b > 1$ such that $L(E, T, v) \leq h_2 - h_3(|v|)^b$.

Proof. In order to verify the above conditions, we should first prove the existence of the solution for system of the state equations (15b)–(15e). Since $\rho T(t - \tau)/(\eta + T(t - \tau)) < \rho$, $v_{\max} < \infty$ and, by neglecting the negative terms in the model, we have

$$\begin{aligned} \frac{dE(t)}{dt} &< \sigma + \rho E(t - \tau), & \frac{dT(t)}{dt} &< r_2 T, \\ \frac{dN(t)}{dt} &< r_3 N, & \frac{du(t)}{dt} &< v_{\max}. \end{aligned} \quad (18)$$

System (18) can be rewritten in the form

$$\begin{aligned} \begin{pmatrix} E(t) \\ T(t) \\ N(t) \\ u(t) \end{pmatrix}' &< \begin{pmatrix} 0 & 0 & 0 & 0 \\ 0 & r_2 & 0 & 0 \\ 0 & 0 & r_3 & 0 \\ 0 & 0 & 0 & 0 \end{pmatrix} \begin{pmatrix} E(t) \\ T(t) \\ N(t) \\ u(t) \end{pmatrix} \\ &+ \begin{pmatrix} \rho & 0 & 0 & 0 \\ 0 & 0 & 0 & 0 \\ 0 & 0 & 0 & 0 \\ 0 & 0 & 0 & 0 \end{pmatrix} \begin{pmatrix} E(t - \tau) \\ T(t - \tau) \\ N(t - \tau) \\ u(t - \tau) \end{pmatrix} + \begin{pmatrix} \sigma \\ 0 \\ 0 \\ v_{\max} \end{pmatrix}, \end{aligned} \quad (19)$$

where $' = d/dt$. This system is linear in finite time with bounded coefficients. Then the solutions of this linear system are uniformly bounded. Therefore, the solution of the nonlinear system (15b)–(15e) is bounded and exists [30]. Hence, condition one is satisfied.

Clearly, the second condition is satisfied by the definition of V_{ad} . System (15b)–(15e) is bilinear in the control variable v and can be rewritten as

$$\vec{F}(t, \vec{X}(t), \vec{X}(t - \tau), v) = \vec{\alpha}(t, \vec{X}) + \vec{\beta}(t, \vec{X}(t - \tau)) + \sigma + v, \quad (20)$$

where $\vec{X}(t) = (E, T, N, u)$, $\vec{X}(t - \tau) = (E(t - \tau), T(t - \tau), N(t - \tau), u(t - \tau))$, and $\vec{\alpha}$ and $\vec{\beta}$ are the vector valued functions of $\vec{X}(t)$ and $\vec{X}(t - \tau)$, respectively. Using the fact that the solutions are bounded, we have

$$\begin{aligned} &|\vec{F}(t, \vec{X}(t), \vec{X}(t - \tau), v)| \\ &\leq |F_1 X(t)| + |F_2 X(t - \tau)| + |F_3| + |F_4| \\ &\leq h_1 |\vec{X}| + |\sigma| + |v|, \end{aligned} \quad (21)$$

where h_1 depends on the coefficients of the system, and

$$\begin{aligned} F_1 &= \begin{pmatrix} 0 & 0 & 0 & 0 \\ 0 & r_2 & 0 & 0 \\ 0 & 0 & r_3 & 0 \\ 0 & 0 & 0 & 0 \end{pmatrix}, & F_2 &= \begin{pmatrix} \rho & 0 & 0 & 0 \\ 0 & 0 & 0 & 0 \\ 0 & 0 & 0 & 0 \\ 0 & 0 & 0 & 0 \end{pmatrix}, \\ F_3 &= \begin{pmatrix} \sigma \\ 0 \\ 0 \\ 0 \end{pmatrix}, & F_4 &= \begin{pmatrix} 0 \\ 0 \\ 0 \\ v \end{pmatrix}. \end{aligned} \quad (22)$$

We also note that the integrand of $J(v)$ is concave in V_{ad} . Finally,

$$\begin{aligned} E(t) - T(t) - \frac{B_v}{2}[v(t)]^2 &< E - \frac{B_v}{2}[v(t)]^2 \\ &\leq h_2 - h_3|v(t)|^2, \end{aligned} \quad (23)$$

where h_2 depends on the upper bounds of $E(t)$ and $T(t)$, and $h_3 = B_v/2$. This completes the proof. \square

We also conclude that there exists an optimal control variable v^* .

6. Optimality Conditions

In this section, we establish the necessary conditions for the optimal solution of the optimization problem (15a)–(15g); we use Pontryagin's minimum (maximum) principle derived by Göllmann et al. [31] for the retarded optimal control problem with mixed control-state constraints. To this end, we define the augmented Hamiltonian function involving the inequality constraints by

$$\begin{aligned} \mathcal{H}(t, E, T, E_\tau, T_\tau, u, v, \lambda) \\ = E(t) - T(t) - \frac{B_v}{2}[v(t)]^2 + \lambda_1(T) \frac{dE(t)}{dt} \\ + \lambda_2(t) \frac{dT(t)}{dt} + \lambda_3(t) \frac{dN(t)}{dt} + \lambda_4 \frac{du(t)}{dt} \\ + \gamma(t) k(N), \end{aligned} \quad (24)$$

where

$$\gamma(t) = \begin{cases} 1 & \text{if } N(t) \leq 0.75, \\ 0 & \text{otherwise} \end{cases} \quad (25)$$

and λ_i ($i = 1, 2, 3, 4$) are the adjoint variables that satisfy

$$\begin{aligned} \lambda_1'(t) &= -\frac{\partial \mathcal{H}}{\partial E}(t) - \chi_{[0, t_f - \tau]}(t) \frac{\partial \mathcal{H}}{\partial E_\tau}(t + \tau), & \lambda_1(t_f) &= 0, \\ \lambda_2'(t) &= -\frac{\partial \mathcal{H}}{\partial T}(t) - \chi_{[0, t_f - \tau]}(t) \frac{\partial \mathcal{H}}{\partial T_\tau}(t + \tau), & \lambda_2(t_f) &= 0, \end{aligned}$$

$$\begin{aligned}\lambda'_3(t) &= -\frac{\partial \mathcal{H}}{\partial N}(t), & \lambda_3(t_f) &= 0, \\ \lambda'_4(t) &= -\frac{\partial \mathcal{H}}{\partial u}(t), & \lambda_4(t_f) &= 0.\end{aligned}\tag{26}$$

Here $\chi_{[0, t_f - \tau]}$ denotes the indicator function of the interval $[0, t_f - \tau]$ and defined by

$$\chi_{[0, t_f - \tau]} = \begin{cases} 1 & \text{if } t \in [0, t_f - \tau], \\ 0 & \text{otherwise.} \end{cases}\tag{27}$$

To minimize the Hamiltonian functional, the Pontryagin's minimum principle [31] is used. Thus, we arrive at the the following theorem.

Theorem 6. Let $(x^*, v^*) \in W^{1, \infty}([0, t_f], \mathbb{R}^4) \times L^\infty([0, t_f], \mathbb{R})$ be the optimal solutions of (15a)–(15g), where $x^* = [E^*, T^*, N^*, u^*]^T$. Then, there exists an adjoint state $\lambda(t) \in W^{1, \infty}([0, t_f], \mathbb{R}^4)$, defined by (26), such that the triple (x^*, v^*, λ) satisfies the state equation

$$\begin{aligned}\frac{dE^*(t)}{dt} &= \sigma + \frac{\rho E^*(t-\tau) T^*(t-\tau)}{\eta + T^*(t-\tau)} - \mu E^*(t-\tau) T^*(t-\tau) \\ &\quad - \delta E^*(t) - a_1 (1 - e^{-u^*}) E^*(t), \\ \frac{dT^*(t)}{dt} &= r_2 T^*(t) (1 - \beta T^*(t)) - \mu E^*(t) T^*(t) \\ &\quad - c_1 N^*(t) T^*(t) - a_2 (1 - e^{-u^*(t)}) T^*(t), \\ \frac{dN^*(t)}{dt} &= r_3 N^*(t) (1 - \beta_2 N^*(t)) - c_2 T^*(t) N^*(t) \\ &\quad - a_3 (1 - e^{-u^*(t)}) N^*(t), \\ \frac{du^*(t)}{dt} &= v^*(t) - d_1 u^*(t),\end{aligned}\tag{28}$$

with the initial conditions

$$\begin{aligned}E^*(t) &= \phi_1(t), & T^*(t) &= \phi_2(t), \\ N^*(t) &= \phi_3(t), & u(t) &= \phi_4(t), \\ & & t &\in [-\tau, 0],\end{aligned}\tag{29}$$

the adjoint state equations

$$\begin{aligned}\lambda'_1(t) &= -1 + \lambda_1(t) \left[\delta + a_1 (1 - e^{-u^*}) \right] \\ &\quad + \lambda_2(t) n T^* + \lambda_1(t + \tau) \chi_{[0, t_f - \tau]} \left[\mu T^* - \frac{\rho T^*}{\eta + T^*} \right], \\ \lambda'_2(t) &= 1 + \lambda_2 \left[-r_2 + 2r_2 \beta T^* + n E^* + c_1 N^* \right. \\ &\quad \left. + a_2 (1 - e^{-u^*}) \right] + \lambda_3 c_2 N^* \\ &\quad + \chi_{[0, t_f - \tau]} \lambda_1(t + \tau) \left[\frac{\rho E^* T^*}{(\eta + T^*)^2} - \frac{\rho E^*}{\eta + T^*} + \mu E^* \right], \\ \lambda'_3(t) &= \lambda_2 c_1 T^* - \lambda_3 \left(r_3 - 2r_3 \beta_2 N^* \right. \\ &\quad \left. - c_2 T^* - a_3 (1 - e^{-u^*}) \right) - \gamma, \\ \lambda'_4(t) &= -\lambda_1(t) a_1 e^{-u^*} E^* + \lambda_2(t) a_2 e^{-u^*} T^* \\ &\quad + \lambda_3(t) a_3 e^{-u^*} N^* + \lambda_4(t) d_1,\end{aligned}\tag{30}$$

with transversality conditions

$$\lambda_i(t_f) = 0, \quad i = 1, 2, 3, 4,\tag{31}$$

and the optimal control

$$v^* = \min \left(v_{\max}, \frac{\lambda_4}{B_v} \right).\tag{32}$$

Proof. The optimal control v^* can be solved from the optimality condition $(\partial \mathcal{H} / \partial v)(t) = 0$; that is, $-B_v v + \lambda_4 = 0$. By using the handedness of the control set V_{ad} , it is easy to obtain v^* in the form of (32). \square

7. Immunotherapy

Model (8) is extended to include external source of immunotherapy treatment of the effector cells such as ACI. We then add the term $w(t)s_1$ to represent the input rate of externally administered antitumour effector cells, where $w(t)$ is the control parameter. Our goal is to maximize an objective functional J subject to the new model with a combination of

chemotherapy and ACI and constraints on the control and the state:

$$\begin{aligned} \max_{v, w \in W_{\text{ad}}} J(v, w) = & \int_0^{t_f} \left(E(t) - T(t) \right. \\ & \left. - \left[\frac{B_v}{2} [v(t)]^2 + \frac{B_w}{2} [w(t)]^2 \right] \right) dt, \end{aligned} \quad (33a)$$

subject to DDEs

$$\begin{aligned} \frac{dE(t)}{dt} = & \sigma + \frac{\rho E(t-\tau) T(t-\tau)}{\eta + T(t-\tau)} - \mu E(t-\tau) T(t-\tau) \\ & - \delta E(t) - a_1 (1 - e^{-u(t)}) E(t) + w(t) s_1, \end{aligned} \quad (33b)$$

$$\begin{aligned} \frac{dT(t)}{dt} = & r_2 T(t) (1 - \beta T(t)) - n E(t) T(t) - c_1 N(t) T(t) \\ & - a_2 (1 - e^{-u(t)}) T(t), \end{aligned} \quad (33c)$$

$$\begin{aligned} \frac{dN(t)}{dt} = & r_3 N(t) (1 - \beta_2 N(t)) - c_2 T(t) N(t) \\ & - a_3 (1 - e^{-u(t)}) N(t), \end{aligned} \quad (33d)$$

$$\frac{du(t)}{dt} = v(t) - d_1 u(t), \quad (33e)$$

the control constraints

$$\begin{aligned} 0 \leq v(t) \leq v_{\max} < \infty, \quad 0 \leq w(t) \leq w_{\max} < \infty, \\ t \in [0, t_f], \end{aligned} \quad (33f)$$

and the state constraint

$$k(N) = N - 0.75 \geq 0, \quad t \in [0, t_f], \quad (33g)$$

where B_w is a weight factor that describes a patient's acceptance level of immunotherapy and the set of all admissible controls W_{ad} is defined by

$$\begin{aligned} W_{\text{ad}} = & \{ (v, w) : (v, w) \text{ piecewise continuous, such that} \\ & 0 \leq v(t) \leq v_{\max} < \infty, \quad 0 \leq w(t) \leq w_{\max} < \infty, \\ & \forall t \in [0, t_f] \}. \end{aligned} \quad (34)$$

Similarly, the optimal solution of the optimization problem (33a)–(33g) satisfies the state equations

$$\begin{aligned} \frac{dE^*(t)}{dt} = & \sigma + \frac{\rho E^*(t-\tau) T^*(t-\tau)}{\eta + T^*(t-\tau)} - \mu E^*(t-\tau) T^*(t-\tau) \\ & - \delta E^*(t) - a_1 (1 - e^{-u^*}) E^*(t) + w^*(t) s_1, \\ \frac{dT^*(t)}{dt} = & r_2 T^*(t) (1 - \beta T^*(t)) - \mu E^*(t) T^*(t) \\ & - c_1 N^*(t) T^*(t) - a_2 (1 - e^{-u^*(t)}) T^*(t), \\ \frac{dN^*(t)}{dt} = & r_3 N^*(t) (1 - \beta_2 N^*(t)) - c_2 T^*(t) N^*(t) \\ & - a_3 (1 - e^{-u^*(t)}) N^*(t), \\ \frac{du^*(t)}{dt} = & v^*(t) - d_1 u^*(t), \\ E^*(t) = & \phi_1(t), \quad T^*(t) = \phi_2(t), \\ N^*(t) = & \phi_3(t), \quad u(t) = \phi_4(t), \\ & t \in [-\tau, 0]. \end{aligned} \quad (35)$$

The adjoint state equations are

$$\begin{aligned} \lambda_1'(t) = & -1 + \lambda_1(t) \left[\delta + a_1 (1 - e^{-u^*(t)}) \right] \\ & + \lambda_2(t) n T^*(t) + \lambda_1(t + \tau) \chi_{[0, t_f - \tau]} \\ & \times \left[\mu T^*(t) - \frac{\rho T^*(t)}{\eta + T^*(t)} \right], \\ \lambda_2'(t) = & 1 + \lambda_2 \left[-r_2 + 2r_2 \beta T^*(t) + n E^*(t) \right. \\ & \left. + c_1 N^*(t) + a_2 (1 - e^{-u^*}) \right] \\ & + \lambda_3 c_2 N^*(t) + \chi_{[0, t_f - \tau]} \lambda_1(t + \tau) \\ & \times \left[\frac{\rho E^*(t) T^*(t)}{(\eta + T^*(t))^2} - \frac{\rho E^*(t)}{\eta + T^*(t)} + \mu E^*(t) \right], \\ \lambda_3'(t) = & \lambda_2 c_1 T^*(t) - \lambda_3(t) \\ & \times \left(r_3 - 2r_3 \beta_2 N^*(t) - c_2 T^*(t) - a_3 (1 - e^{-u^*(t)}) \right) \\ & - \gamma, \\ \lambda_4'(t) = & -\lambda_1(t) a_1 e^{-u^*(t)} E^*(t) + \lambda_2(t) a_2 e^{-u^*(t)} T^*(t) \\ & + \lambda_3(t) a_3 e^{-u^*(t)} N^*(t) + \lambda_4(t) d_1, \end{aligned} \quad (36)$$

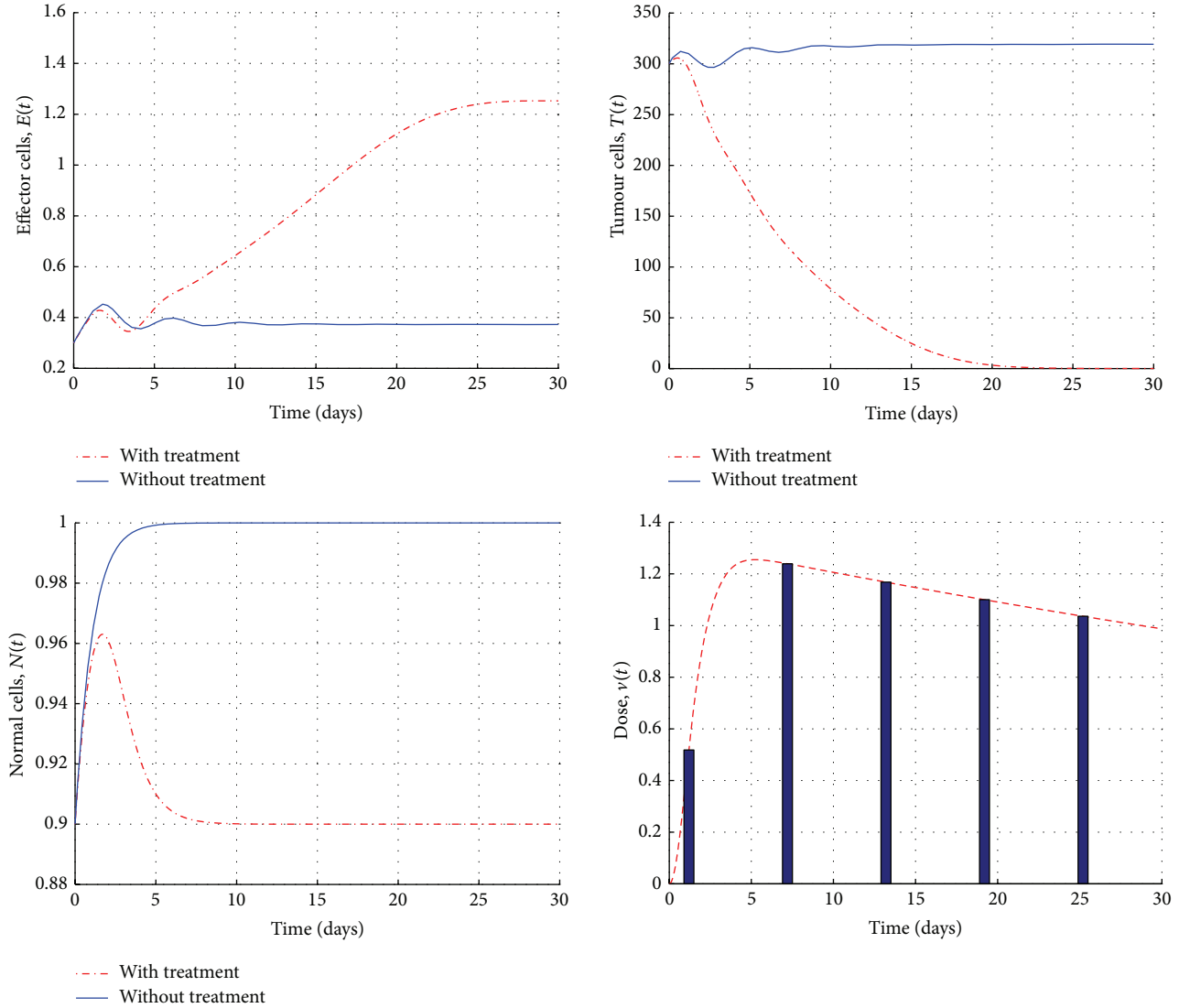


FIGURE 4: Simulations of system (28)–(32), in the stable region, before and after the treatments with control with the initial conditions $E_0 = 0.3$, $T_0 = 300$, and $N_0 = 0.9$ and the parameter values are given in the text.

with the transversality conditions $\lambda_i(t_f) = 0$, $i = \{1, 2, 3, 4\}$, and the minimum condition

$$v^* = \min \left(v_{\max}, \frac{\lambda_4}{B_v} \right), \quad w^* = \min \left(w_{\max}, \frac{\lambda_1 s_1}{B_w} \right). \quad (37)$$

When $s_1 = 0$ (without immunotherapy), system (35)–(37) reduces to system (28)–(32).

Remark 7. In the case of immunotherapy alone ($u(t) = 0$), the objective functional becomes

$$J(w) = \int_0^{t_f} \left(E(t) - T(t) - \frac{B_w}{2} [w(t)]^2 \right) dt. \quad (38)$$

8. Numerical Simulations of the Optimal Control System

Numerical simulations leading to the approximation of the optimal controls (35)–(37) are carried out using the forward Euler method for the state system and backward difference approximation for the adjoint system. We assume the step-size h , such that $\tau = mh$ and $t_f - t_0 = nh$, where $(m, n) \in \mathbb{N}^2$. We define the state, adjoint, and control variables at the mesh points. An initial guess is given for the controls v and w , which are then updated continuously until the objective functional satisfies the conditions. However, there are several major problems to be overcome when solving delay differential equations. These include stability, stiffness, and discontinuities in the right-hand side of the equation. Stability and stiffness can be handled by the correct choice

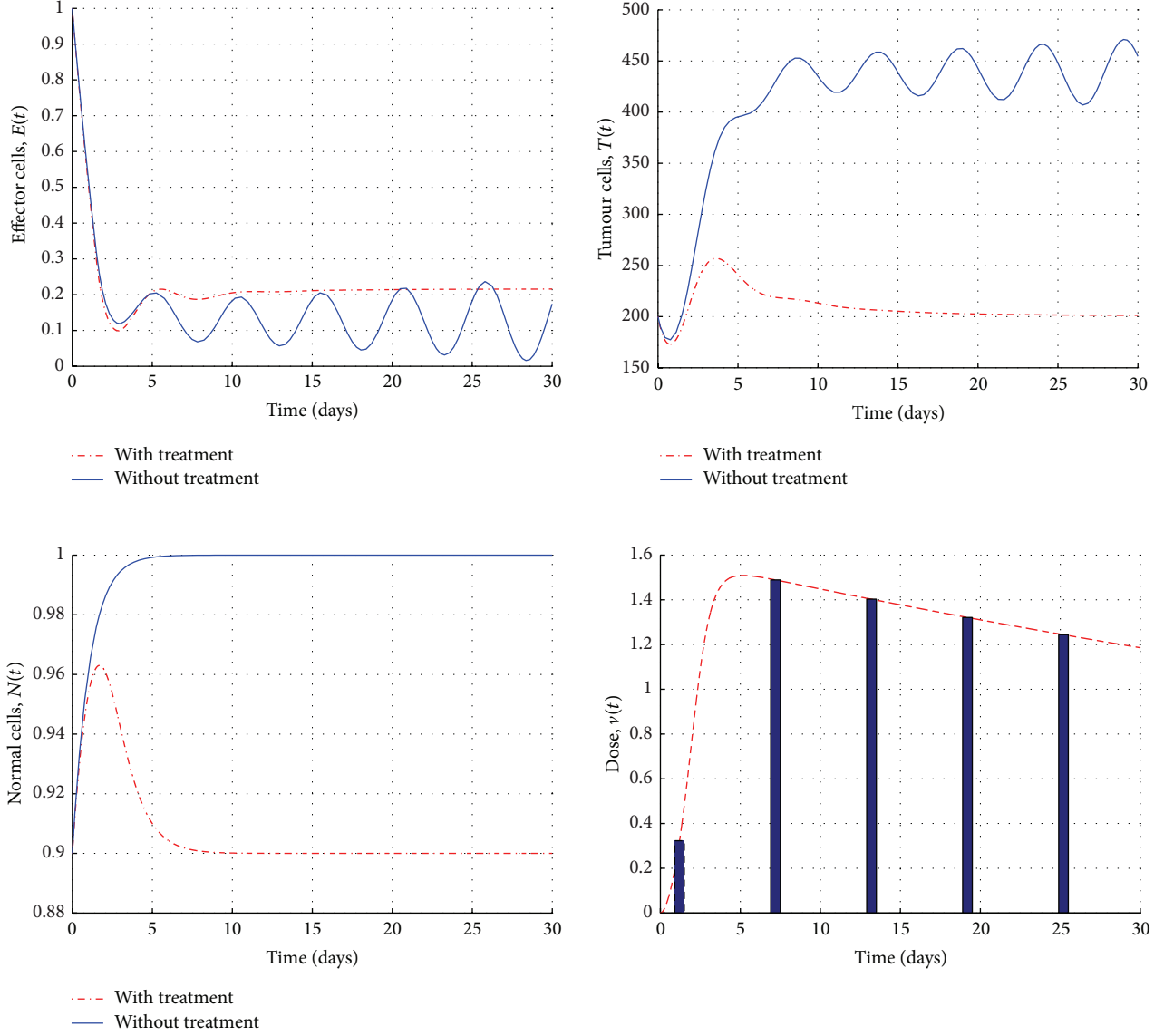


FIGURE 5: Simulations of the system (28)–(32), in an unstable region, before and after the chemotherapy treatment with the control and initial conditions $E_0 = 1$, $T_0 = 200$, and $N_0 = 0.9$ and the parameter values are given in the text.

of implicit solvers [27]. The delay terms can create a whole suite of discontinuities; see [32, 33].

We choose a different set of parameter values (in stable and unstable regions). In the current simulations, we vary the three parameters σ , ρ , and τ , and fix the other parameters:

$$\begin{aligned}
 \delta &= 0.2, & \eta &= 0.3, & \mu &= 0.003611, & s_1 &= 0.3, \\
 r_2 &= 1.03, & r_3 &= 1, & \beta &= 2 \times 10^{-3}, & \beta_2 &= 1, \\
 n &= 1, & c_1 &= 0.00003, & c_2 &= 0.00000003, & a_1 &= 0.2, \\
 a_2 &= 0.4, & a_3 &= 0.1, & d_1 &= 0.01, & B &= 100.
 \end{aligned} \tag{39}$$

We solve the optimality system to determine the optimal control situation (i.e., the drug strategy) and predict the evolution of the tumour cells, effector cells, and normal cells of each control strategy in 30 days.

Figure 4 shows the numerical simulations of the state system before and after chemotherapy treatment using optimality system (28)–(32) when $\sigma = 0.5$, $\rho = 0.01$, and $\tau = 1.2$ (in the stable region). We note that, in the presence of chemotherapy with optimal control, the effector cells population grows up significantly, while the tumour cells population decreases and is totally eradicated after 20 days. In the meantime, the normal cells population remains over 75%. Yet, Figure 5 shows the impact of chemotherapy treatments (with optimal control) when we choose the parameter values in an unstable region ($\sigma = 0.2$, $\rho = 0.2$, and $\tau = 1.5$).

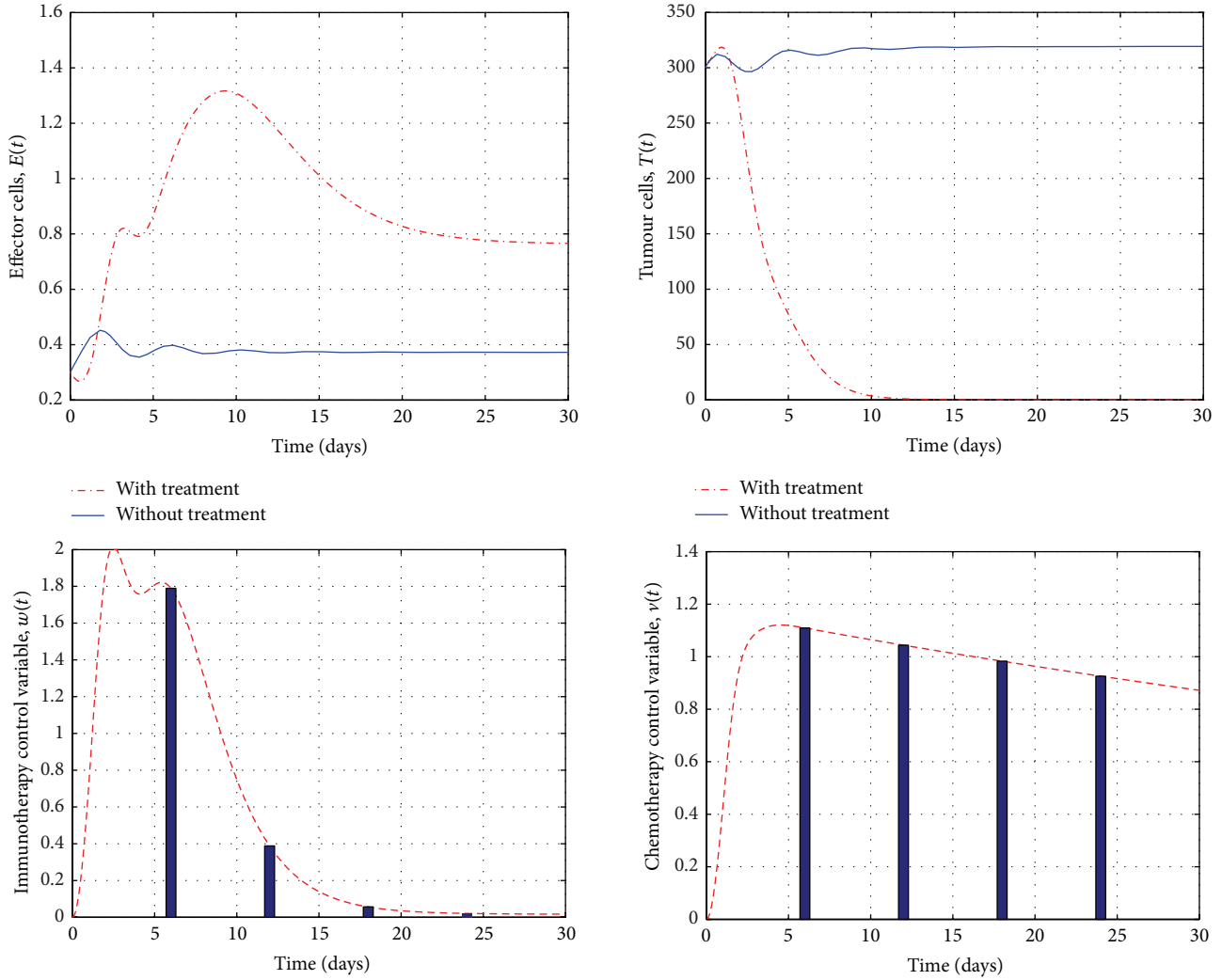


FIGURE 6: Simulations of system (35)–(37), in the stable region, before and after the immunochemotherapy treatments with controls. It shows that the tumour cells population can be eradicated in day 12.

The tumour and effector cells populations are oscillating over time in the absence of chemotherapy, while the presence of treatment helps the immune system to keep the growth of the tumour cells under its control.

Figure 6 presents the evolution of system (35)–(37) in the case of combination of chemotherapy and ACI. The parameters values are chosen in the stable region. We notice that the tumour cells population can be eradicated after day 12 which is faster compared to the results of Figure 4 when we used the chemotherapy alone. In other words, the numerical results show that using the combination immunochemotherapy is more effective than using chemotherapy treatment alone.

However, Figure 7 shows evolution of the system with only immunotherapy (i.e., without chemotherapy). We may notice from the figure that this case reflects the best therapeutic strategies for treatment of tumour, where the recovery becomes faster with high dosage of immunotherapy where $w(t)$ can reach the value of 3.5 level compared with the combination it was in level 2.

9. Concluding Remarks

In this paper, we provided a delay differential model with control variables that describe the interactions of immune cells, tumour cells, normal cells, and immunochemotherapy treatment with control variables. A pontryagin-type maximum principle is derived, for retarded optimal control problems with delays in the state variable when the control system is subject to a mixed controlstate constraint, in order to minimize the cost of treatment, reduce the tumour cells load, and keep the number of normal cells above 75% of its carrying capacity. We presented an efficient numerical technique, based on forward difference approximation to the state system and backward difference scheme to the adjoint system, to solve the optimal control problem and identify the best treatment strategy when we adopt the chemotherapy treatment alone or a combination of chemoimmunotherapy, with minimum side effects. The numerical results show and confirm that the optimal treatment strategies reduce the

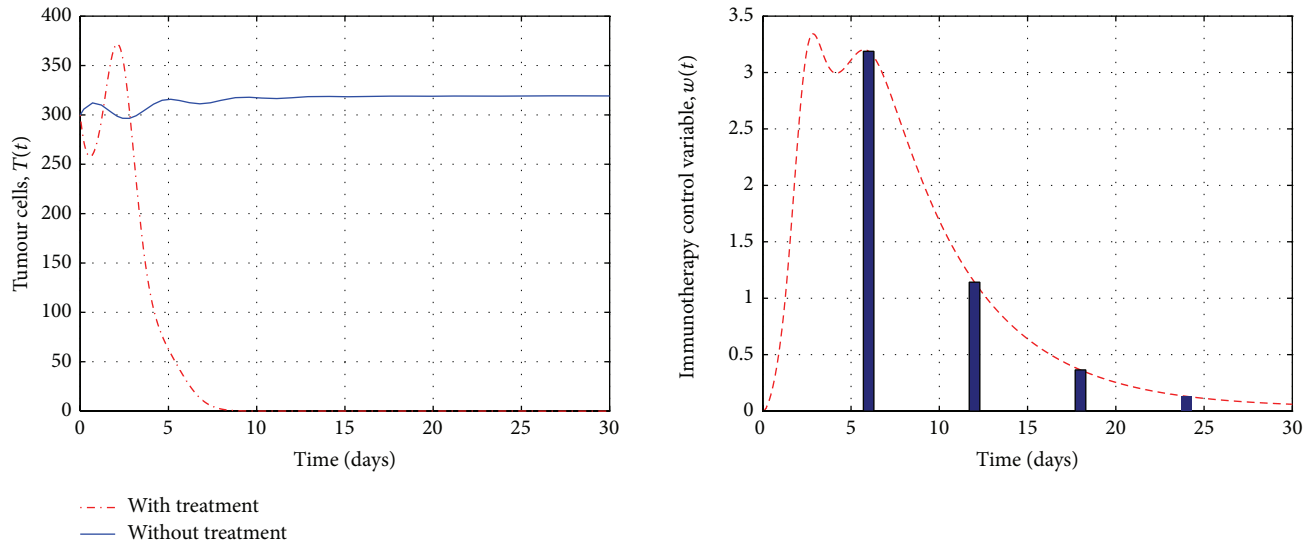


FIGURE 7: Simulations of the tumour cells population of system (35)–(37), before and after immunotherapy with control. It shows that the tumour cells can be eradicated at day 7 with high immunotherapy dosage where the control value $w(t)$ reaches the value of 3.5.

tumour cells load and increase the effector cells after few days of therapy. The performance of combination therapy protocol was better than the standard protocol of chemotherapy alone. The numerical simulations show the rationality of the model presented, which in some degree meets the natural facts.

This work can be extended to more sophisticated problems with delays in both state and control variables, when the control system is subject to a mixed controlstate constraints.

Conflict of Interests

The authors declare that they have no conflict of interests regarding the publication of this paper.

Acknowledgments

This work was supported by UAE University. The authors would like to thank the referees and Professor Loredana G. Marcu for their valuable and contractive comments that improved this paper.

References

- [1] B. Joshi, X. Wang, S. Banerjee, H. Tian, A. Matzavinos, and M. A. J. Chaplain, "On immunotherapies and cancer vaccination protocols: a mathematical modelling approach," *Journal of Theoretical Biology*, vol. 259, no. 4, pp. 820–827, 2009.
- [2] D. Kirschner and J. C. Panetta, "Modeling immunotherapy of the tumor—immune interaction," *Journal of Mathematical Biology*, vol. 37, no. 3, pp. 235–252, 1998.
- [3] V. A. Kuznetsov, I. A. Makalkin, M. A. Taylor, and A. S. Perelson, "Nonlinear dynamics of immunogenic tumors: parameter estimation and global bifurcation analysis," *Bulletin of Mathematical Biology*, vol. 56, no. 2, pp. 295–321, 1994.
- [4] L. G. de Pillis, W. Gu, and A. E. Radunskaya, "Mixed immunotherapy and chemotherapy of tumors: modeling, applications and biological interpretations," *Journal of Theoretical Biology*, vol. 238, no. 4, pp. 841–862, 2006.
- [5] L. G. de Pillis, K. R. Fister, W. Gu et al., "Optimal control of mixed immunotherapy and chemotherapy of tumors," *Journal of Biological Systems*, vol. 16, no. 1, pp. 51–80, 2008.
- [6] R. P. Araujo and D. L. S. McElwain, "A history of the study of solid tumour growth: the contribution of mathematical modelling," *Bulletin of Mathematical Biology*, vol. 66, no. 5, pp. 1039–1091, 2004.
- [7] N. Bellomo, N. K. Li, and P. K. Maini, "On the foundations of cancer modelling: selected topics, speculations, and perspectives," *Mathematical Models and Methods in Applied Sciences*, vol. 18, no. 4, pp. 593–646, 2008.
- [8] H. M. Byrne, T. Alarcon, M. R. Owen, S. D. Webb, and P. K. Maini, "Modelling aspects of cancer dynamics: a review," *Philosophical Transactions of the Royal Society of London A*, vol. 364, no. 1843, pp. 1563–1578, 2006.
- [9] M. A. J. Chaplain, "Modelling aspects of cancer growth: insight from mathematical and numerical analysis and computational simulation," in *Multiscale Problems in the Life Sciences*, vol. 1940 of *Lecture Notes in Mathematics*, pp. 147–200, Springer, Berlin, Germany, 2008.
- [10] M. L. Martins, S. C. Ferreira Jr., and M. J. Vilela, "Multiscale models for the growth of avascular tumors," *Physics of Life Reviews*, vol. 4, no. 2, pp. 128–156, 2007.
- [11] J. D. Nagy, "The ecology and evolutionary biology of cancer: a review of mathematical models of necrosis and tumor cell diversity," *Mathematical Biosciences and Engineering*, vol. 2, no. 2, pp. 381–418, 2005.
- [12] T. Roose, S. J. Chapman, and P. K. Maini, "Mathematical models of avascular tumor growth," *SIAM Review*, vol. 49, no. 2, pp. 179–208, 2007.
- [13] R. Yafia, "Dynamics analysis and limit cycle in a delayed model for tumor growth with quiescence," *Nonlinear Analysis: Modelling and Control*, vol. 11, no. 1, pp. 95–110, 2006.

- [14] R. Yafia, "A study of differential equation modeling malignant tumor cells in competition with immune system," *International Journal of Biomathematics*, vol. 4, no. 2, pp. 185–206, 2011.
- [15] R. Eftimie, J. L. Bramson, and D. J. D. Earn, "Interactions between the immune system and cancer: a brief review of non-spatial mathematical models," *Bulletin of Mathematical Biology*, vol. 73, no. 1, pp. 2–32, 2011.
- [16] F. A. Rihan and D. H. A. Rahman, "Delay differential model for tumor-immune dynamics with HIV infection of CD4⁺ T-cells," *International Journal of Computer Mathematics*, vol. 90, no. 3, pp. 594–614, 2013.
- [17] F. A. Rihan, M. Safan, M. A. Abdeen, and D. H. Abdel Rahman, "Qualitative and computational analysis of a mathematical model for tumor-immune interactions," *Journal of Applied Mathematics*, vol. 2012, Article ID 475720, 19 pages, 2012.
- [18] F. A. Rihan, D. H. Abdel Rahman, S. Lakshmanan, and A. Alkhajeh, "A time delay model of tumour-immune system interactions: global dynamics, parameter estimation, sensitivity analysis," *Applied Mathematics and Computation*, vol. 232, pp. 606–623, 2014.
- [19] L. G. de Pillis and A. Radunskaya, "The dynamics of an optimally controlled tumor model: a case study," *Mathematical and Computer Modelling*, vol. 37, no. 11, pp. 1221–1244, 2003.
- [20] G. W. Swan, "Optimal control applications in the chemotherapy of multiple myeloma," *IMA Journal of Mathematics Applied in Medicine and Biology*, vol. 2, no. 3, pp. 139–160, 1985.
- [21] F. Castiglione and B. Piccoli, "Cancer immunotherapy, mathematical modeling and optimal control," *Journal of Theoretical Biology*, vol. 247, no. 4, pp. 723–732, 2007.
- [22] D. Kirschner and A. Tsygvintsev, "On the global dynamics of a model for tumor immunotherapy," *Mathematical Biosciences and Engineering*, vol. 6, no. 3, pp. 573–583, 2009.
- [23] M. Villasana and A. Radunskaya, "A delay differential equation model for tumor growth," *Journal of Mathematical Biology*, vol. 47, no. 3, pp. 270–294, 2003.
- [24] M. Bodnar, "The nonnegativity of solutions of delay differential equations," *Applied Mathematics Letters. An International Journal of Rapid Publication*, vol. 13, no. 6, pp. 91–95, 2000.
- [25] A. Halanay, *Differential Equations: Stability, Oscillations, Time Lags*, Academic Press, New York, NY, USA, 1966.
- [26] L. G. De Pillis and A. Radunskaya, "A mathematical tumor model with immune resistance and drug therapy: an optimal control approach," *Journal of Theoretical Medicine*, vol. 3, no. 2, pp. 79–100, 2001.
- [27] F. A. Rihan, E. H. Doha, M. I. Hassan, and N. Kamel, "Numerical treatments for Volterra delay integro-differential equations," *Computational Methods in Applied Mathematics*, vol. 9, no. 3, pp. 292–308, 2009.
- [28] C. T. H. Baker, G. Bocharov, A. Filiz et al., "Numerical modelling by delay and volterra functional differential equations," in *Proceeding of the Topics in Computer Mathematics and its Applications*, pp. 113–137, LEA, Athens, Greece, 1999.
- [29] W. H. Fleming and R. W. Rishel, *Deterministic and Stochastic Optimal Control*, Springer, New York, NY, USA, 1975.
- [30] D. L. Lukes, *Differential Equations: Classical to Controlled*, Academic Press, New York, NY, USA, 1982.
- [31] L. Göllmann, D. Kern, and H. Maurer, "Optimal control problems with delays in state and control variables subject to mixed control-state constraints," *Optimal Control Applications & Methods*, vol. 30, no. 4, pp. 341–365, 2009.
- [32] F. A. Rihan, *Numerical treatment of delay differential equation [Ph.D. thesis]*, University of Manchester, Manchester, UK, 2000.
- [33] F. A. Rihan and B. F. Rihan, "Numerical modelling of biological systems with memory using delay differential equations," *Applied Mathematics & Information Sciences*, vol. 9, no. 3, pp. 1–14, 2015.